UC Berkeley
UC Berkeley Electronic Theses and Dissertations

Title

Design, Synthesis, and Characterization of Functional Materials for Battery Electrolyte and Marine Antifouling Applications

Permalink

https://escholarship.org/uc/item/494317t9

Author

Buss, Hilda Gail

Publication Date

2017

Peer reviewed|Thesis/dissertation

Design, Synthesis, and Characterization of Functional Materials for Battery Electrolyte and Marine Antifouling Applications

By

Hilda Buss

A dissertation submitted in partial satisfaction of the

requirements for the degree of

Doctor of Philosophy

in

Chemical Engineering

in the

Graduate Division

of the

University of California, Berkeley

Committee in charge:

Professor Bryan D. McCloskey, Chair
Professor Nitash Balsara
Professor Phillip B. Messersmith

Spring 2017

Design, Synthesis, and Characterization of Functional Materials for Battery Electrolyte and Marine Antifouling Applications

by
Hilda Buss

Abstract

Design, Synthesis, and Characterization of Functional Materials for Battery Electrolyte and Marine Antifouling Applications

by

Hilda Buss

Doctor of Philosophy in Chemical Engineering

University of California, Berkeley

Professor Bryan D. McCloskey, Chair

In this thesis, challenges associated with the creation of anti-fouling surfaces and polymer-based electrolytes are addressed using a versatile polymer chemistry that affords control over material functionality through the manipulation of the polymer's side chain composition. The polymers used in this thesis generally have a backbone comprised in-part or wholly of poly(ethylene oxide) (PEO) with pendant allyl side groups, to which various moieties can be attached using a straightforward thio-ene click. I describe the attachment of different side groups to design polymers with desirable properties, then characterize these polymers' performance when used as anti-fouling surface coatings and electrolytic solutions.

The development of high lithium cation transference number electrolytes, those in which the ionic conductivity is carried predominantly by the lithium ion instead of its counteranion, could limit concentration polarization that plagues current battery electrolytes. The typical approach for achieving high transference number electrolytes is to immobilize the anion on a polymer to limit anion motion. We designed a lithium neutralized PEO backbone with pendent sulfonate groups to use as a dry single ion conductor. Interestingly, these sulfonate functionalized materials self-assembled into very well ordered, small (2.5nm) lamellae, which result from aggregation and phase segregation of the attached ions from the polymer backbone. Unfortunately, given that the ions are not solvated (i.e., dissociated) by the polymer backbone, no conductivity was observed in these materials, including at high (120°C) temperatures. The lack of ion dissociation suggests that a solvent with higher Lewis basicity or acidity than the PEO backbone is needed to disrupt the contact ion pairs and allow conductivity.

Polyelectrolyte solutions were therefore prepared from the polyanion described above and a strong Lewis basic solvent, dimethyl sulfoxide. These solutions exhibited an excellent combination of high ionic conductivity and Li$^+$ transference number (*e.g.*, 1.2 mS/cm and 0.99, respectively, at 25°C). In addition, this system is tunable (polyanion molecular weight and charge concentration can be manipulated), and provided a platform to explore the tradeoff between conductivity and transference number in liquid electrolytes with an unprecedented combination of both. Taking advantage of this tunability, I explored the effect of temperature, polymer molecular weight, solvent choice, and small molecule salt addition on the solution transport properties. Li$^+$ transference number was found to be temperature independent, as

expected for solutions that are fully dissociated at all temperatures measured. Scaling theories for molecular weight dependence of diffusion coefficients described the polymer behavior well but did not capture the behavior of the lithium cation, which was generally found to be independent of polymer molecular weight. Solutions made in a variety of solvents all displayed high cation transference number and high conductivity, but there was no simple relationship between solvent and electrolyte properties. Finally, when mixed into the polyelectrolyte solution, small molecule salts, such as LiTFSI, increase the solution conductivity, but at a substantial cost to Li^+ transference number.

In another application, I designed polymer materials that prevent marine fouling, the attachment of organisms to human-made structures in marine environments. Amphiphilic polymers have been shown to be effective as antifouling materials against a variety of organisms and organic compounds. We therefore designed a polymer platform to present sequence-specific peptoids at the surface of thin film coatings. These amphiphilic coatings were used to study the effect of hydrophobic and hydrophilic residue sequence on antifouling performance. The polymer platform had a polystyrene (PS) anchoring block, and a PEO presentation block to which peptoids were attached. We showed that fluorinated moieties are very surface active and direct the surface composition of the polymer thin film. The position and number of fluorinated groups in the polypeptoid was shown to affect both the surface composition and antifouling properties of the film. Specifically, the position of the fluorinated units in the peptoid chain changes the surface chemistry and the antifouling behavior, while the number of fluorinated residues affects the fouling release properties.

In addition to the peptoid sequence, the specific composition of the polymer platform is an important consideration for film stability and surface presentation. The anchoring block molecular weight plays an important role in film stability, but also affects the overall film hydrophobicity, which adversely affects antifouling performance. It was found that the coatings using an entirely hydrophobic scaffold, polystyrene-*b*-poly(dimethyl siloxane), performed well against only one of the marine organisms studied (*Ulva linza*), but that hydrophilic coatings comprised of polystyrene-*b*-poly(ethylene oxide) performed well against all marine organisms studied, including *U. linza* and *Navicula*. Finally, it was shown that perfluorooctane thiol attached directly to the polymer chain can direct surface presentation of the entire polymer system, thereby allowing improved anti-fouling film formation.

To my cat,
Winnie

TABLE OF CONTENTS

List of Figures

List of Tables

Acknowledgements

Like any good adventure, my time at UC Berkely was filled with surprises, challenges, and, most importantly, wonderful people. Without these people, this thesis would not exist and graduate school would have been a lot less interesting.

I would first like to thank my advisers, Bryan McCloskey and Rachel Segalman for the many things they taught me and the support they provided. Bryan has an impressive level of engagement in his lab and an unstoppable curiosity that is contagious. The community that I had the privilege to be a part of in Rachel's lab taught me what kind of scientist that I wanted to be, and the training in both materials design and professional skills that I received from Rachel has served me well throughout my time in Berkeley.

Nothing in lab would have been possible without the training, help, and companionship from my labmates: Thanks to Victor, who taught me everything I needed to know in grad school, and to Wendy, who had infinite patience for my naivete, guiding me through my first few years of research. Hannah, Adrianne, Bryan, and Megan, who sat in group meeting, asking the toughest questions in the nicest way, teaching me to think critically and what it means to be a good labmate. Nathan, who helped make material when I just couldn't keep up. Barbara and Boris, who kept lab fun. Jessica, Sara, and Colin, who welcomed me when I was lab-less, with open arms. Sophia, who went above and beyond what I expected from an undergrad, always putting out excellent work. And to Kyle, who was the best science buddy I ever could have asked for, always being down to take apart broken equipment, brainstorm all the crazy ideas, wrestle with figures, or just help me locate my sanity.

Of course, all of that would have been moot without all of the people who keep this place up and running. Thanks for Carlet Altamirano and Joseph Nolan, for making sure I don't need to worry about the logistics. Thanks to Ron Scholtz for assistance in cleaning out the mess that was Kerr Lab and keeping us safe.

Finally, special thanks go to my housemates, Carly, Lin, Nico, and Jacob for making Berkeley a place I call home.

1 Introduction

1.1 A short history of polymer chemistry

The first use of chemistry to control the properties of a polymeric material can be traced back to 1600 B.C. in ancient Mesoamerica. A natural latex material was extracted from *Castilla elastica*, a tree indigenous to the area. When the tree extract is dried, the material is brittle, and fractures easily. However, the ancient Mesoamerican people added juice from the *Ipomoea alba* plant, and were able to produce a rubbery material that could be formed into balls or figurines, then cured into a solid material. The appeal of this material was the unique set of physical properties that were accessible, specifically elasticity and the ability to form a shape, and then have it remain that shape.

It was not until much later that the underlying chemistry was understood. The *C. elastic* extract was an emulsion of an aqueous phase and an organic, polyisoprene containing phase. Mixing in juice from *I. alba* served both to purify small molecules out of the polymer, but also to crosslink the chains. A very large amount of progress has been made in the intervening 3600 years in the understanding and synthesis of polymeric materials. This progress now allows us to design and synthesize materials with specific, and otherwise inaccessible, properties.[1]

1.2 Why polymers?

Polymers have a unique range of achievable mechanical and chemical characteristics. This range of characteristics stems from their large molecular structures, as well as the range of structures achievable, and the ease of introducing different chemical interactions. While the bottom limit of polymer size is somewhat dependent on the property of interest, certain polymers can achieve >1 million g/mol molecular weights for a single chain, and crosslinked polymer networks are approximated as having infinite molecular weight. Polymers can be arranged as long chains, crosslinked networks, branched systems, densely grafted bottle brushes, or even cyclic molecules, with each arrangement resulting in its own unique set of mechanical properties. Poly(ethylene) with different backbone configurations serve as a common example of the large range of accessible properties for a single polymer, as hard plastic milk jugs (high density poly(ethylene)) and soft, stretchable plastic bags (low density poly(ethylene)) are both comprised of poly(ethylene).

An astounding variety of chemical functionalities can also be incorporated into polymers, allowing their use in a large number of applications. Examples range from super hydrophobic fluorinated materials to hydrophilic materials that contain ionicially charged moieties. In fact, it is possible to combine these chemistries in different architectures within a single polymeric material by covalently tethering two chemistries together in blocks, mixing them randomly, grafting a polymer to another, or even combining them in a sequence specific way. This range of chemistries gives rise to super strong materials like Kevlar, super soft and silky materials that give hair conditioners their characteristic texture, materials with a memory (e.g., shrink hose), or biologically active materials that bind in specific ways and take on specific structures.

Finally, polymers are easily solution or thermally processable, either into thin films, coatings, or bulk materials, making them easy to use for a variety of applications.

1.3 Challenges facing targeted polymer design

In many ways, the expansive tunability of polymer materials is both a blessing and a curse. As described in the previous section, there are numerous variables that can be used to manipulate the properties of any given material. There is no way to combinatorialy address the entire accessible phase space for a certain material goal in a single PhD thesis. For this reason, it is important to understand the design rules for polymers, and to determine structure-property relationships when they are lacking. It is nevertheless this same tunablility that allows polymers to be used as state-of-the-art materials for a variety of applications. With this in mind, we set out to use polymer design principles to tackle the following challenges:

1.3.1 *Design a battery electrolyte with superior transport properties*

Current batteries employ small molecule salts dissolved in organic solvents as an electrolyte. While these electrolytes provide sufficient performance to allow the expansive commercialization of Li-ion batteries, poor ion transport in current lithium ion based electrolytes, particularly through highly tortuous, thick electrodes, is a limiting factor for fast charging. More specifically, the transport properties of interest are:

1. High ionic conductivity
2. High cation transference number (the fraction of total current carried initially by the cation)

The design of electrolytes with these properties would enable fast (>2C), efficient battery charging and decrease operating over potentials. It would also allow the use of thicker porous electrodes in high-energy cell designs that would lead to decrease of weight by 30-50%.

1.3.2 *Design a coating for seafaring ships with superior antifouling properties*

Marine biofouling presents a unique challenge for antifouling materials due to the large variety of marine organisms that can foul a surface, ranging from organic material and biofilms to seaweed and barnacles. Fouling is a problem that affects all seafaring vessels, and can increase fuel consumption by up to 30%. The design of ship hull coatings which can prevent this fouling while not contaminating the ocean is critically important. In addition to their antifouling properties, the coating stability and compatibility with under layers (such as anticorrosion layers) are also important to the design of a successful antifouling coating.

1.4 Approach to polymer design

In order to limit the scope of the project, I used the same base polymer chemistry for both projects. The chemistry of choice was poly(allyl glycidyl ether) (PAGE) for its favorable backbone chemistry, compatibility with other polymer chemistries, and the ability to easily functionalize the polymer through the pendent allyl group.

This materials is a poly(ethylene oxide) (PEO) backbone with pendent allyl groups. PEO is a well studied polymer with a number of favorable traits. It is a hydrophilic material with a high dielectric constant (for a polymer), allowing it to highly interact with water and salts. Its use as a battery electrolyte has been explored due to its ability to conduct lithium cations. It was also found to have some resistance to marine fouling. The crystalline nature of PEO is not always desirable, particularly in battery applications, but the presence of the pendent allyl group breaks up the PEO crystallinity, and PAGE itself is a viscous liquid at room temperature with a T_g of about -80°C.

PAGE is grown through the anionic ring opening polymerization of allyl glycidyl ether, an epoxide ring with a pendent allyl group. This synthetic route allows for good control over the molecular weight of the polymers grown, as well as low polydispersity of the resulting material. It can also be copolymerized with other epoxides, such as ethylene oxide, to maintain the same backbone but decrease the concentration of pendent allyl groups. This also allows for the facile formation of block copolymers incorporating PAGE.

Finally, the allyl group can be easily, and with high conversion, functionalized using thiol-ene click chemistry. Thiol-ene is the chemistry of choice for this functionalization because it is compatible with a large number of solvents and reaction conditions. It is a radical initiated chemistry, compatible with both thermal and ultraviolet radical initiators. It is possible to incorporate both small and polymeric materials, as well as charged, hydrophilic, or hydrophobic residues. The reaction can be easily tracked through NMR. As the reader will see, this chemistry has been exploited as a method to introduce a variety of chemical functionalites into the PAGE-based polymers studied here.

1.5 **Aims**

The aims of this thesis were threefold:

1. To design and synthesize polymer systems to address the two challenges listed above
2. To characterize the materials and determine whether or not the material was appropriate for the intended application
3. To understand the underlying physics that most affected properties of interest and optimize the system for better performance

Chapter 2 leads the reader through the design and synthesis of a material for battery electrolytes. The particular system synthesized, a lithium sulfonate-modified PAGE polymer, was found to order into lamellae whose layers were comprised of the PAGE backbone and sulfonate aggregates, respectively. Unfortunately, this indicated that the lithium sulfonate existed as an associated ion pair and no conductivity was observed in these materials. To induce dissociation, I dissolved these materials in a Lewis basic organic solvent and found that this strategy provided electrolytes with an unprecedented combination of conductivity and Li^+ transference number. The characterization of these so-called polyelectrolyte solutions is the focus of chapters 3 and 4.

The fifth chapter leads the reader through the design and testing of antifouling coatings that are comprised of peptoid-modified PAGE-based polymers. When optimized, these materials were found to provide excellent anti-fouling properties against two common biofoulants, and provided more insight into the design criterion for antifouling materials. The sixth and final chapter delves deeper into the structure property relationships introduced in chapter 5.

2 Understanding the molecular structure of dry polyether polyelectrolytes

2.1 Abstract

Development of dry single ion conducting polymer electrolytes which do not contain flammable organic solvents for Li metal batteries would enable safer Li metal cycling and improved specific and volumetric battery energy densities. The use of swollen polymer or liquid electrolytes tends to provide higher ionic conductivities, but also increases the flammability of the system. Therefore, understanding how to engineer improved ion transport through dry single ion conductors (SIC) is of importance for battery safety. A poly(ethylene oxide) based polymer was designed and synthesized to be a dry SIC. The benefit of this system is that the polymer backbone is able to coordinate lithium cations and that ion concentration and ion chemistry is easily tunable, thereby allowing systematic exploration and understanding of the complex polymer phase behavior. In this chapter I present insights into the relationship between polymer structure, crystallization, and phase behavior. Interestingly, these sulfonate functionalized materials self-assemble into very well ordered, small (2.5nm) lamellae, which result from aggregation and phase segregation of the attached ions from the polymer backbone. Unfortunately, given that the ions are not solvated (i.e., dissociated) by the polymer backbone, no conductivity is observed. In the end, I will emphasize the importance of employing solvents with sufficient Lewis basicity to disrupt ion crystals to achieve high ion conductivity in these single ion-conducting electrolytes.

2.2 Introduction to dry single ion conductors

Battery electric vehicles (BEVs) present a huge opportunity in the development of clean energy infrastructure. Widespread adoption of BEVs would limit petroleum reliance and the environmental impact of internal combustion engines, while opening new markets to US manufacturing. However, the underlying battery technology is plagued by a number of problems including low energy density, range anxiety, safety concerns, and high cost. Large efforts are being made by industry and government agencies to address these issues. A variety of new battery chemistries, including lithium-air, lithium-sulfur, and magnesium-ion, have emerged as possible alternatives to increase the energy density of batteries over current state-of-the-art Li-ion batteries. However, these high-energy technologies have not been successfully commercialized in BEVs given the numerous technical challenges that limit their competitiveness compared to Li-ion batteries. An important limitation for BEVs is the long time necessary to charge the battery; even with Tesla superchargers, it takes 40 minutes to charge today's lithium ion batteries from 10 to 80% state-of-charge. While the price of the lithium-ion battery used in the Nissan Leaf dropped from about $18,000 in 2010 to $6,500 in 2014, it is still a significant fraction of the cost of the car[2]. It is clear that if we want consumers to embrace BEVs as a mainstream transportation option, we have to improve the performance of the batteries that power them.

Dry polymer electrolytes have the possibility of eliminating flammable solvents in batteries, greatly improving the safety of batteries. Binary lithium salts (such as lithium (trifluoromethane sulfonimide), LiTFSI) dissolved in poly(ethylene oxide) (PEO) are well known as useful solid polymer electrolytes for Li batteries[3–5]. PEO is able to coordinate lithium ions, thereby solvating the binary salt and allowing modest ion conductivity in a non-volatile electrolyte. However, the lithium transference number for these and other binary salt electrolytes is low, typically between 0.1-0.4, meaning that most of the ionic current is initially carried by the electrochemically inactive counteranion. In contrast, dry single ion conductors

(SICs) are polymers wherein the negative counter ions are covalently tethered to the polymer backbone, rendering them immobile[6–9]. The Li^+ transference number of such systems is one, because the immobile anion concentration is fixed throughout the polymer electrolyte matrix, eliminating concentration polarization. To take advantage of both the solvating efficacy of PEO and the desirable aspects of single ion conductors, I use the sulfonate functionalized PEO used in the previous chapters with variable ion content, as shown in Figure 2-1.
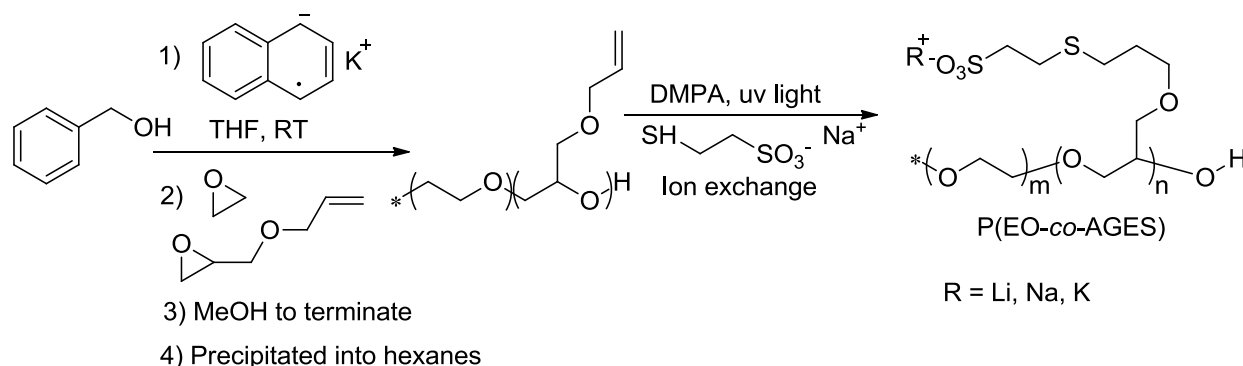
Figure 2-1 Synthesis of poly(ethylene oxide-co-allyl glycidyl ether/sulfonate) (P(EO-co-AGES)) used in this study. The polymer is studied with a variety of counterions, Li^+, Na^+ and K^+. The percent ion content is reported for each polymer and is quantified as n/(n+m).

Here, salt concentration is changed by changing the ratio of EO units (m) to AGE/sulfonate units (n). The mole percent AGE/sulfonate in the polymer is reported using the following equation

$$mol\% \ sulfonate = \frac{n}{m+n} \qquad (2\text{-}1)$$

Using this nomenclature, 100% is PAGE/sulfonate homopolymer and 0% is PEO homopolymer (with no attached ions). Additionally, because the sulfonate is introduced via thiolene-click chemistry, it is possible to incorporate a variety of different anions into the system. This work will focus on bound sulfonate anions. Additionally, the polymer can be ion exchanged from the sodium cation for a variety of different ions, which has interestingly been found to have a large effect on the polymer structure.

2.3 Experimental

2.3.1 Synthesis of PAGES

The poly(ethylene oxide-co-allyl gylcidyl ether/sulfonate) copolymer was synthesized as shown in Figure 2-1. The parent poly(ethylene oxide-co-allyl glycidyl ether) (P(EO-co-AGE)) polymer was synthesized by anionic ring-opening copolymerization of allyl glycidyl ether and ethylene oxide from benzyl alcohol with a potassium naphthalenide solution to generate the potassium alkoxide as described previously[10]. Successful synthesis of the precursor PAGE polymers was confirmed by ^{1}H nuclear magnetic resonance (NMR) spectroscopy in deuterated chloroform ($CDCl_3$). Gel permeation chromatography was carried out on an Agilent system with a 1260 Infinity isocratic pump, degasser, and thermostated column chamber held at 30 °C containing Agilent PLgel 10 μm MIXED-B and 5 μm MIXED-C columns. The thiol-ene click reaction was done in a tetrahydrofuran water mixture with a 2,2-dimethoxy-2-phenylacetophenone (DMPA) radical initiator[11]. Purification and ion exchange to lithium, sodium, or potassium were

performed via dialysis (3.5kDa MWCO, Spectrum) in water. Successful synthesis of the precursor PAGES polymers was confirmed by ^{1}H (NMR) spectroscopy in deuterated water (D$_2$O). Successful ion exchange and removal of excess salts was confirmed using inductively coupled plasma-optical emission spectroscopy (Varian). Samples were freeze dried before being brought into an argon glovebox.

2.3.2 *Thermal Analysis*

Differential scanning calorimetry (DSC) was performed on a Perkin Elmer DSC 8500 between 2-200°C/min (cpm). Pans with 1-5mg of dry polymer were hermetically sealed in the glovebox before analysis in the DSC. Traces reported here are the second heating scan. Thermal gravimetric analysis (TGA) was performed on a PerkinElmer Pyris 1 TGA at 10°C/min.

2.3.3 *Wide-Angle X-ray Scattering (WAXS)*

All X-ray scattering experiments were performed with guidance from Jacob Thelen, and more details about x-ray scattering experiments and theory can be found in Dr. Thelen's articles[12,13] and thesis[14] (chapter 2). Samples for X-ray scattering were prepared in an Argon glovebox (<1ppm O$_2$ and H$_2$O) by pressing freeze dried polymers into 1/8 inch diameter holes in 1/32 inch thick Aflas rubber sheets. The polymer-filled spacer was then covered on both sides by 1 mil Kapton film windows and sealed in a custom-built hermetically sealed aluminum sample holder. The sealed samples were removed from the argon glovebox and vacuum annealed at 90°C for 24 hours before being cooled and measured. Experiments were performed at the Advanced Light Source (ALS) at LBNL, Beamlime 7.3.3[15].The sample-detector distance was determined using a silver behenate calibration standard. Temperature was controlled by a sample stage holder, and held between 25°C and 120°C. The scattering data were analyzed using the Nika macro in Igor Pro developed by Jan Ilavsky[16]. WAXS patterns are circular averages of the 2D scattering pattern, unless otherwise specified.

2.4 **Results and Discussion**

2.4.1 *Thermal Analysis*

DSC shows that the a pure PAGES homopolymer, where equation 2-1 is 100% for the structure shown in Figure 2-1, has no accessible phase transitions (Figure 2-2). These are both second heating traces from close to -100°C to 150°C. The fast cooling trace (shown in blue) has larger artifacts at the beginning and end of the scan, but can increase the size of glass transitions, making them easier to observe. The lack of any glass transitions or melting peaks in either trace makes it clear that there are no accessible transitions between -100°C to 150°C. The lack of a Tg is surprising. The Tg of pure PAGE is -80°C, and the transition temperature is expected to increase as ions are added to the backbone[17]. As we will see, despite the lack of a melting temperature, these polymers are highly crystalline, and this crystallinity suppresses any glassy to rubbery transitions that the backbones may undergo, as has been observed by others[18].
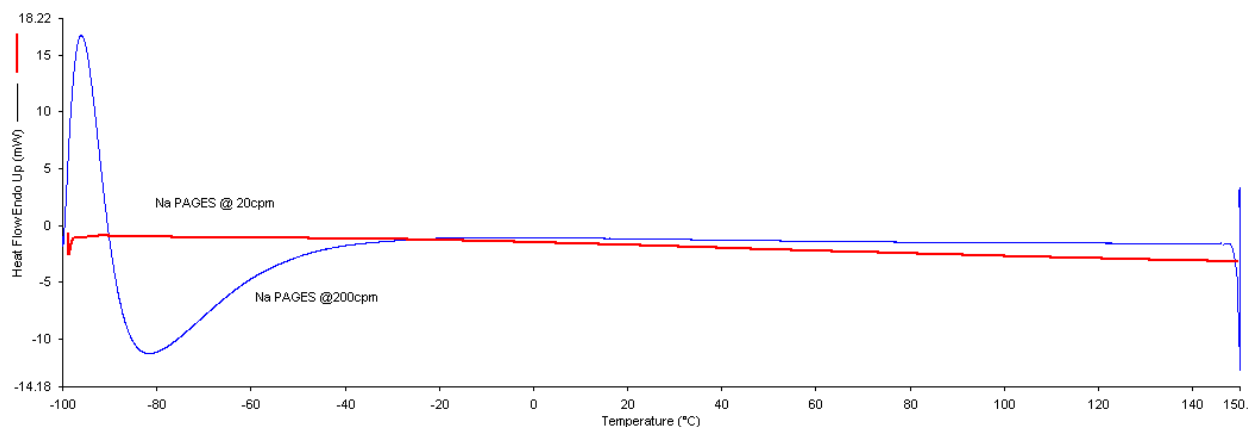
Figure 2-2 Sample DSC of Na PAGES at both fast (blue) and slow (red) heating rates. No accessible phase transitions are observed. The second heating scan is shown in each case.

TGA shows that the PEO backbone of these polymers is relatively stable, not degrading until 300°C (Figure 2-3). The pendent allyl groups present on in the PAGE homopolymers decreases the stability of the overall polymer, with degradation being observed starting at ~225°C. The PAGES degrades at the same temperature as its PAGE parent polymer, but the magnitude of the degradation is larger. Additionally, the ion content of the PAGES polymer makes it very hygroscopic. The initial drop in mass at the start of the scan is due to initial water loss. For this reason, all X-ray scattering and conductivity samples were dried and prepared inside of an argon glovebox.
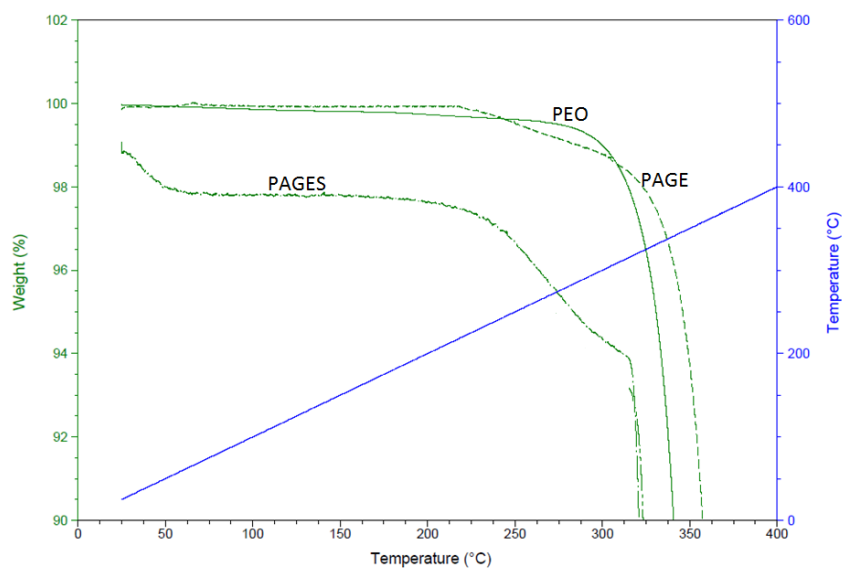
Figure 2-3 TGA of PEO, PAGE, and PAGES at 10 ^{o}C/min.

2.4.2   *Wide angle X-ray scattering (WAXS)*

While the PAGES polymers showed no accessible melting temperatures, it was clear from visual inspection and mechanical properties that they were highly crystalline materials. WAXS was used to further characterize the structure of the PAGES polymers. A typical PAGES WAXS pattern and

schematics for the proposed structure are shown in Figure 2-4. It is very clear from the peaks at integer spacing of q* that these materials take on a layered structure (Figure 2-4A). The position of the q* peak determines the size of the lamellar domains, which is found to be 2.5nm. It is unusual to see such a small domain size in microphase separated polymers, but such structures have been observed before for polyelectrolytes with long sidechains[18,19]. For example, on such system is a protonated poly(ethylene imine) backbone with alkyl carboxylate counter ions. The alkyl chains on the counter ions will crystallize within the hydrophobic domains, and the backbones and the carboxylates will group in a separate domain. In agreement with these studies, I suggest that the PEO backbones align in sheets, with the sulfonate groups assembling between these sheets of PEO backbones, as drawn in Figure 2-4B. In support of this proposed structure, I have calculated that the sulfonate side chain, if full extended (including bond angles), would be 1.3nm long. In the proposed structure, each sulfonate chain is head to head, meaning that the domains should be 2.6nm wide, which is in reasonable agreement with the observed domain size. It is also interesting to note that there are many higher order peaks visible in the WAXS patterns shown, suggesting that these structures are unusually well ordered.
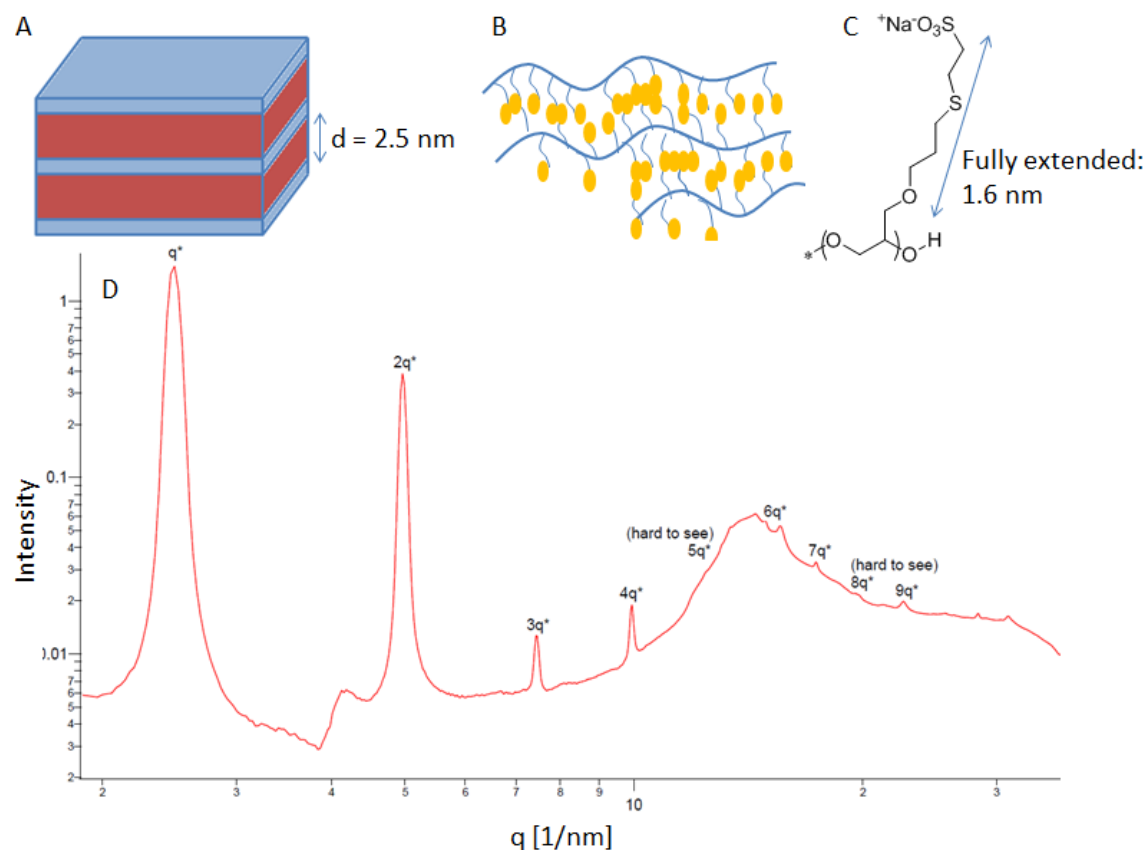
Figure 2-4 Sample WAXS pattern of sodium PAGES and the corresponding structures. A) A schematic of a lamellar structure. The blue phase contains PEO backbones while the red phase contains the sidechains. From the position of the q* peak, the domain spacing is calculated to be 2.5nm. B) The polymer backbones (blue) are likely aligned with aggregated or crystalized side chains (yellow ovals). C) Structure of PAGES and the calculated length of the side chain assuming it were fully extended. D) WAXS spectrum of sodium PAGES with a characteristic lamellar pattern (q* ~ 2.5 nm^{-1}) and an amorphous halo (15 nm^{-1}). The bump at 4 nm^{-1} is due to poor subtraction of the Kapton peak.

In agreement with the ones of the works mentioned above[18], the driving force for the ordering of PAGES is hydrophobicity, not crystallization, despite the presence of crystals. It is apparent that the freeze dried, unannealed sodium 100% PAGES sample in Figure 2-5 has a broad amorphous peak at 15nm^{-1}. This suggests that after freeze drying, there is little to no crystallinity, despite the presence of the lamellar peaks. This indicates that unlike the studies cited above, crystallization is not the dominant factor in structuring the material. Instead, the ionic groups prefer to microphase separate away from the PEO backbone into the lamellar structure. Once templated in this manner, the sulfonate groups crystalize on smaller length scales within the lamellae. The amount of order within these crystals is very sensitive to processing conditions, but the crystallization happens faster during annealing. I would like to again emphasize that these crystals do not have an accessible melting temperature, which also suggests that it is the side chains crystalizing as opposed to the PEO-based backbone. When PEO crystalizes, the backbones stack, but PEO crystals melt at 60°C, and no thermal transition is observed at 60 °C for PAGES, suggesting that the PEO-backbone is not crystallizing. It is also interesting to note that the crystal structure is different from both the structure of PEO as well as the structure of the sodium sulfonate thiol used for the click reaction. This suggests that the sulfonate groups are effectively templated within the lamellae, thereby crystalizing into a new, very stable, structure.
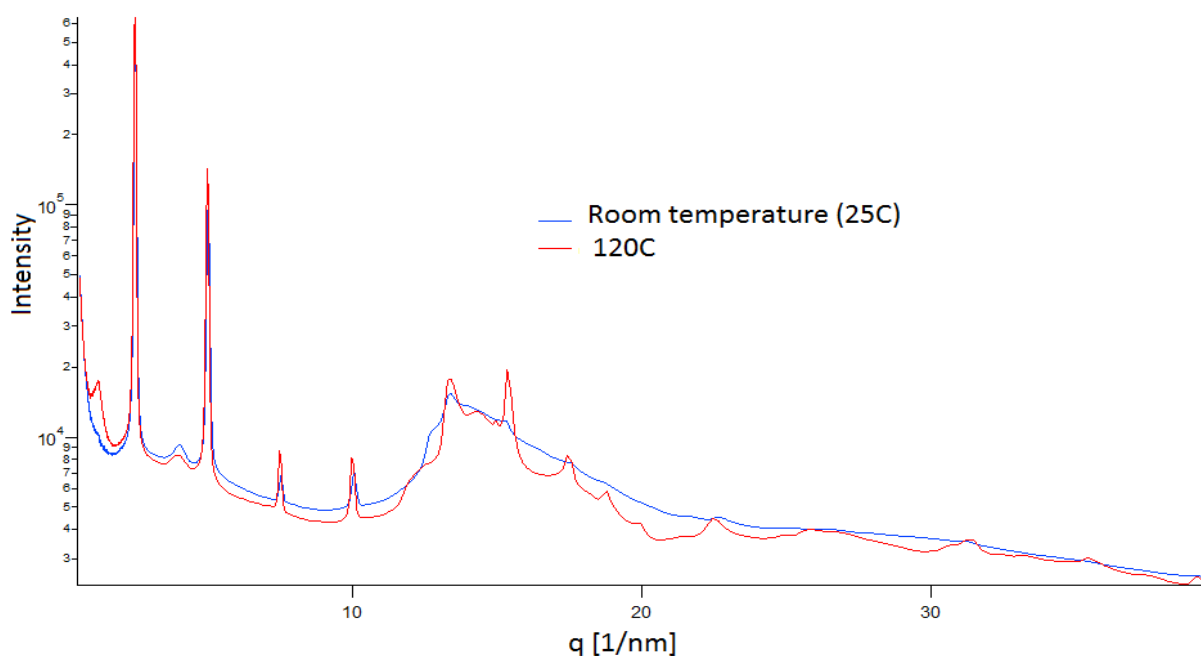
Figure 2-5 WAXS pattern of sodium PAGES after freeze drying (blue) and after annealing at 120C for 45 minutes (red).

By heat pressing the PAGES polymer into the spacer used, it is possible to align the lamellae and the crystals within the sample. This gives anisotropic scattering, and by taking line cuts at different angles of the 2D scattering pattern, it is possible to begin elucidating the orientational relationship between the crystals and the lamellae (Figure 2-6). First, the orientation of the lamellae allows for easier observation of higher order peaks. As seen in the assignments in Figure 2-6 and the table or peak position and q/q*, there are many higher order peaks, suggesting, along with the extremely sharp nature of these peaks, that these lamella are exceptionally well ordered. Additionally, because the highest intensity of the lamellar peaks at 80° but the highest intensity for the crystalline peaks is at 0°, most of the crystals are oriented

orthogonal to the lamellar peaks. It is interesting to note that the peak at 0.15nm^{-1} is the only peak that is not oriented. However, further characterization and peak assignments would be required to extract out additional information about the structure of this material.

	Position [1/A]	q/q*
q*	0.2476	1.0000
2q*	0.4956	2.0013
3q*	0.7428	2.9997
4q*	0.9898	3.9972
5q*	1.2404	5.0091
6q*	1.4822	5.9855
7q*	1.7304	6.9878
8q*	1.9751	7.9760
9q*	2.2264	8.9908
10q*	2.4678	9.9657
11q*	2.7665	11.1719
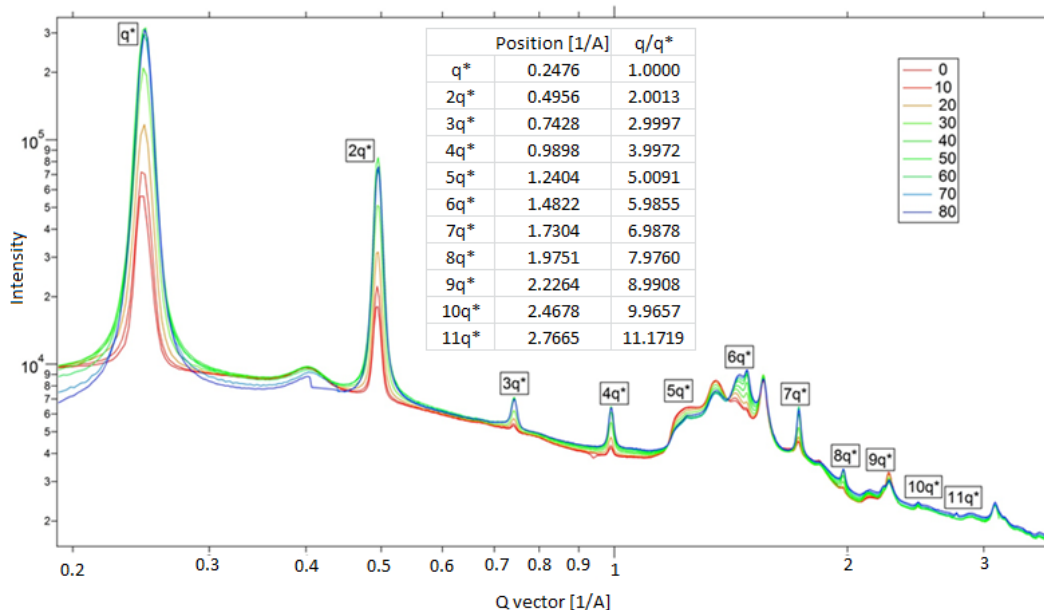
Figure 2-6 WAXS pattern at different angles of a heat pressed sodium PAGES. Each differently colored line is a line cut at a different angle of the two dimensional scattering pattern. The lamellar peaks are labeled, and the position of that peak is listed in the table, as well as q/q* to show the integer spacing. The broad peak at 0.4 Å^{-1} is Kapton.
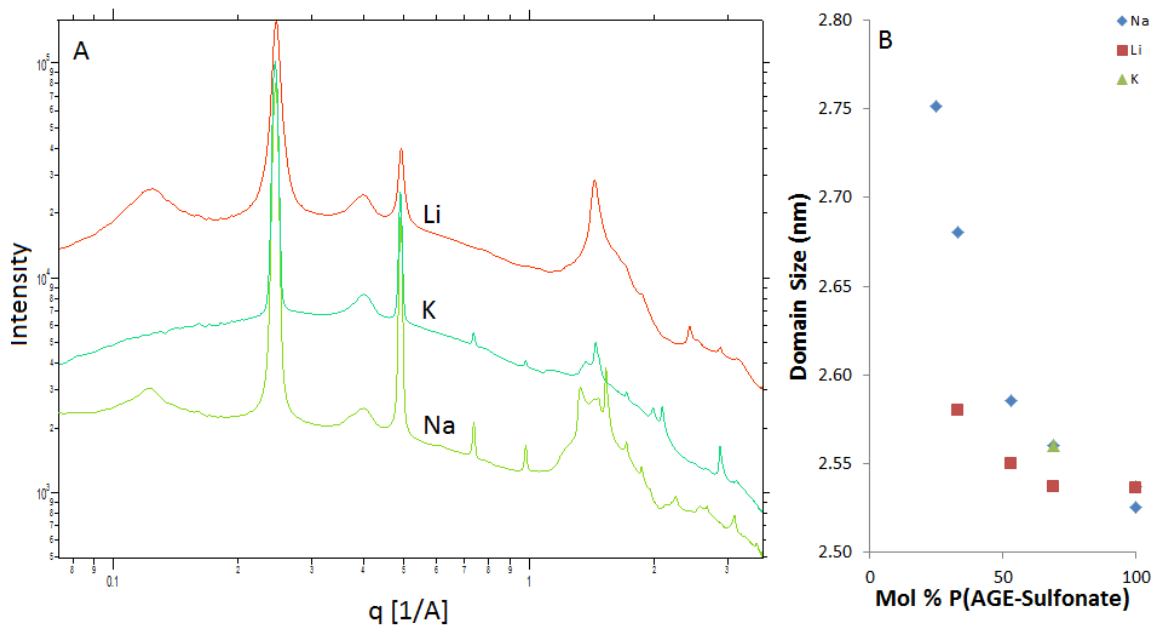
Figure 2-7 WAXS pattern of PAGES polymer with different counter ions and mol% sulfonate. A) WAXS patterns of PAGES with different counterions. B) Domain size is affected by both the counterion as well as the mol% sulfonate.

Figure 2-7 shows that while the samples order into a lamellar structure regardless of the counterion (lithium, sodium, or potassium), both the lamellar domain size and the crystal structure within these domains changes with counterion. The smallest ion, lithium, has the smallest domain size, while the larger ions, sodium and potassium, have larger domain sizes. There are insufficient potassium samples to conclude whether the potassium samples tend to be larger than the sodium form.

Interestingly, Figure 2-7B demonstrates that domain size increases with decreasing ion content. The interaction between the sulfonate ions acts to pin the PEO chains together, presumably through a physical ionic crosslink. As the sulfonate content decreases, the number of possible ionic crosslinks between chains decreases, and the chains have more freedom to separate. Well below 25 mol% sulfonate, the PEO backbone crystalizes and no lamellar structure is seen (not shown, at 2.5 and 1 mol% sulfonate).

2.4.3   *Conductivity and Solubility of PAGES*

Due to the high crystallinity of PAGES, they have no ionic conductivity, both at room temperature and at 120°C (as measured using AC impedance spectroscopy). This is not surprising, as conductivity in polymer electrolytes depends on charge carrier concentration and polymer chain segmental motion[5,20]. The ions in this system are in crystal aggregates, which means that there is no ion dissociation, and there is no accessible melting temperature for these ion containing crystals, regardless of ion content. Additionally, these crystal aggregates serve to pin the polymer chains in physical crosslinks, and limit segmental motion, the second important factor in ionic conductivity. However, even if plasticizers are used to increase segmental motion, if the ions containing crystals are not dissociated there, can be no ionic conductivity. This was experimentally observed in PAGES/PEO blends, which did exhibit glass transitions temperature between -50°C and -25°C, depending on PAGES concentration, but still displayed no measurable ionic conductivity at 120°C.

The solubility and swellability of PAGES in various solvents was explored. However, the low Lewis basicity of the sulfonate anion means that these materials were poorly solvated by most organic solvents (Table 2-1). While swelling was shown to be an effective way to increase segmental motion, ion dissociation proved to be the largest challenge in both this system. However, the goal of this work was to design a highly conductive and high cation transference number system. This is still achievable if the ions are fully dissociated in a high donor number solvent, as will be explored in the following chapters.

Table 2-1 Solubility of lithium PAGES in various solvents.

Solvent	Soluble?	Donor number
Dimethyl sulfoxide (DMSO)	Yes	29.8
Dimethylacetamide (DMAC)	Yes	27.8
N-methylpyrrolidon (NMP)	Yes	27.3
Dimethylformamide (DMF)	Yes	26.6
Tetrahydrofuran (THF)	No	20
Dimethoxyethane (DME)/ polyethyleneoxide (PEO)	No	20
Dimethyl carbonate (DMC)	No	15.1
Acetonitrile (ACN)	No	14.1

2.5 **Conclusions**

In this chapter, I explored the use of sulfonate functionalized PEO as dry single ion conducting polymer electrolyte. These materials self-assemble into well-ordered and small lamellar structure, with the PEO backbones aligned in a plane, and the side chains clustered in between these planes of PEO backbones. This structure is seen for a variety of ion content, from 25-100mol% sulfonate, as well as a variety of counter ions (lithium, sodium, and potassium). While these structures are unusually small for well-ordered, phase-separated polymers, the sulfonate ions crystalize within these lamellae, with no accessible melting temperature. The high crystallinity of these materials gives them no ionic conductivity, and precludes their use as battery electrolytes. These materials also have low solubility in poor Lewis basic solvents, including PEO itself, which explains the lack of ion dissociation in the polymer backbone itself. I conclude that to achieve ion dissociation and ionic conductivity, these polymers *must* be dissolved in strong Lewis basic solvents. We will explore this possibility in the following chapter.

3 Demonstration of Nonaqueous Polyelectrolyte Solutions as Liquid Electrolytes with High Lithium Ion Transference Number and Conductivity

3.1 Abstract

Liquid electrolytes using small molecule lithium salts are currently employed in commercial lithium-ion batteries. While these systems display high ionic conductivity, most of the initial current is carried by the electrochemically inactive anion due to the large solvated radius of Li^+. This behavior results in concentration polarization of the salt during cycling, particularly in porous electrodes, which limits battery energy density and disallows fast charging. Liquid electrolytes with high Li^+ transference number (where Li^+ carries most or all of the ionic current) and high ionic conductivities have the potential to improve battery performance by limiting these concentration gradients. In this chapter, we propose lithium neutralized polyanions in solution as an intriguing strategy to attain both high lithium transference number (> 0.9) and high ionic conductivity (> 1 mS/cm) at room temperature. We study a Li^+-neutralized poly(ethylene oxide)-based sulfonated polyanion from the previous chapter, dissolved in an otherwise salt-free high Lewis basic solvent, dimethyl sulfoxide, that allows solubility of the highly-charged polyelectrolyte to *ca.* 1.0 M Li^+ concentrations. ^7Li and ^1H pulsed field gradient nuclear magnetic resonance (PFG-NMR) measurements are used to attain the self diffusion coefficients of the Li^+ and anion, D_+ and D_-, respectively, and hence the Li^+ transference number, t_+. Conductivity calculated from the PFG-NMR results showed good agreement with conductivity measured directly using a conductivity meter. Interestingly, higher concentration solutions yielded Li^+ diffusion coefficients greater than that expected from Stokes-Einstein theory for a species in a viscous solution. Although the polyelectrolyte solutions studied here exhibit maxima in conductivity around 0.5 M Li^+ (1.5 mS/cm), t_+ continuously increases with concentration, achieving 0.99 at 1.0 M Li^+ in solutions containing the highest molecular weight polyanion studied. Many of the results presented in this chapter have also been published in *ACS Energy Letters*[21].

3.2 Introduction

The development of high lithium cation transference number electrolytes, those in which the ionic conductivity is carried predominantly by the lithium ion, could limit concentration polarization that plagues current battery electrolytes[22,23] and enhance battery performance. In binary salt electrolytes, most of the ionic conductivity is initially carried by the anion, with cation transference numbers ranging from 0.1–0.4, regardless of whether the solvent is a liquid[24,25] or polymer[26]. These low transference numbers cause concentration gradients in the electrolytic solution both in the separator and in the porous electrodes[27], limiting effective use of the electrode active materials, as well as introducing concentration overpotentials[28], both of which reduce battery energy density.

While the benefits of high Li^+ transference number (t_+) has been modeled[22,29] and is often cited[8,9,30,31] as motivation in new electrolyte design, limitations in high t_+ electrolytes has made systematic experimental studies of their influence on battery performance difficult. The typical approach for achieving high t_+ electrolytes is to immobilize the anion on a polymer[8,30,32] to limit anion motion, although Li^+ conductive ceramics[33] are also being explored in this context. However, these dry electrolytes suffer from either low ionic conductivity or high interfacial impedance (particularly when porous electrodes are used)[34]. For

example, the highest bulk ionic conductivity reported for dry (non-gelled) single ion conducting polymers is approximately 10^{-5} S cm^{-1} at 60°C[30], nearly three orders of magnitude lower than a standard liquid electrolyte at room temperature[35].

Swelling with organic solvents to increase the conductivity of these single ion conductors, both in polymer gels[36,37], and composite gels[38,39] has proven to be effective. Yet, this concept has not been fully extended to electrolytes in which single ion conducting polymers (Li$^+$-neutralized polyanions) are fully dissolved in nonaqueous solvents to create liquid polyelectrolyte solutions. The transport properties of such solutions, specifically the relative mobilities of the polymer and its Li$^+$ counterion, are poorly understood, even though this strategy presents an opportunity to design electrolytes that may allow an unprecedented combination of liquid-like conductivities and t_+ approaching unity.

In this study, we synthesize a model anionic polymer, poly(allyl glycidyl ether-lithium sulfonate) (PAGELS), via the synthetic route shown in Figure 3-1. PAGELS was selected as our model polymer because the polymerization affords precise control of polymer molecular weight (with low polydispersity) and charge density along the polymer backbone. The PAGELS polymer is then dissolved in an otherwise salt-free strong Lewis basic solvent, dimethyl sulfoxide (DMSO), that allows solubility of the highly charged polyelectrolyte to ca. 1.0 M Li$^+$ concentrations. We demonstrate that these polyelectrolyte solutions exhibit an excellent combination of high ionic conductivity and transference number (e.g., 1.2 mS/cm and 0.98 at 25°C). With future advances in the polymer chemistry, this strategy provides a clear path to the development of highly stable Li battery electrolytes with liquid-like conductivities and transference numbers above 0.99. In addition, the strategy introduced here provides a method to tune both transference number and conductivity, thereby providing an experimental approach to better understand the relationship between these transport properties and battery performance.
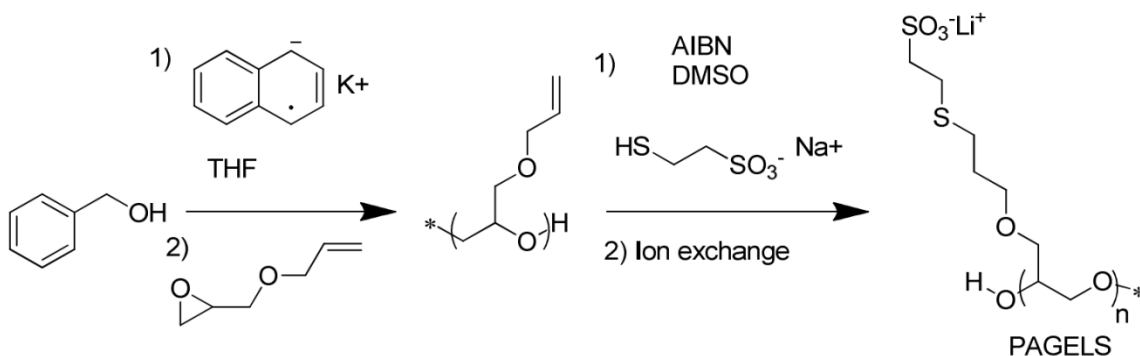
Figure 3-1 Synthesis of the lithium neutralized polyanion used in this study. The poly(allyl glycidyl ether) parent polymer was synthesized anionically. Other than the addition of THF from titration of the benzyl alcohol from a potassium naphalenide solution in THF, the reaction was done neat. The pendent allyl groups are functionalized with sulfonates using thiol-ene click chemistry to create the PAGELS polymer.

3.3   **Experimental**

3.3.1   *Synthesis*

Poly(allyl glycidyl ether/lithium sulfonate) (PAGELS) was synthesized as shown in Figure 3-1. The parent poly(allyl glycidyl ether) (PAGE) polymer was synthesized by neat anionic ring-opening

polymerization of allyl glycidyl ether from benzyl alcohol with a potassium naphthalenide solution to generate the potassium alkoxide as described previously[10]. Successful synthesis of the precursor PAGE polymers was confirmed by ^{1}H nuclear magnetic resonance (NMR) spectroscopy in deuterated chloroform (CDCl$_3$). Gel permeation chromatography was carried out on an Agilent system with a 1260 Infinity isocratic pump, degasser, and thermostated column chamber held at 30 $^\circ$C containing Agilent PLgel 10 µm MIXED-B and 5 µm MIXED-C columns. Molecular weights and dispersities were recorded relative to polystyrene standards. The dispersity indices of these polymers are reported in Table 3-1.

Table 3-1. Properties of the PAGELS used in this study. Most data reported was collected using the shortest (n=43) polymer.

Molecular Weight (M$_n$) [g/mol][1]	Degree of polymerization (n)[1]	Precursor Dispersity [2]
11,000	43	1.1
24,000	93	1.4
66,000	250	1.2
132,000	500	1.2

[1]Measured by ^{1}H NMR spectroscopy by end-group analysis. [2]Measured for the precursor PAGE polymer by size exclusion chromatography relative to polystyrene standards.

Thiol-ene *click* chemistry was used to attach sulfonate anions to the synthesized PAGE. PAGE, 10 wt. eq. of dimethyl sulfoxide (DMSO, Sigma Aldrich), 1.5 mol. eq. of sodium 2-mercaptoethanesulfonate (Na 2-MCES, Sigma Aldrich), and 0.2 mol. eq. of radical initiator azobisisobutyronitrile (AIBN, Sigma Aldrich) were added to a tared round-bottom flask and stirred at room temperature until homogeneous. The round-bottom flask was placed in an oil bath at 65°C, attached to a bubbler to relieve pressure from N$_2$ production, and stirred for 24 h. The solution was then poured into a 2.54 cm diameter dialysis tube (3.5 kDa MWCO, Spectrum Labs), dialyzed two times to ion exchange with a total of 2 wt. eq. of lithium bromide in ultrapure water (Milli-Q), and dialyzed (3.5kDa MWCO, Spectrum) against pure water six times to remove residual reactants and salts. Each dialysis step required a minimum of two hours.

The solution was filtered through a nylon syringe filter (0.4 µm, Fischer Scientific), frozen at –85 $^\circ$C, and lyophilized (Labconco) at 15 mTorr. Successful synthesis of the polymer was confirmed using ^{1}H NMR spectroscopy in D$_2$O indicating complete conversion of allyl substituents. Reported molecular weights in Table 3-1 are number average molecular weights determined via end-group analysis by ^{1}H NMR spectroscopy (Bruker, 500MHz) by comparing end-group benzyl resonances (2H) relative to polyether backbone signals (5H/repeat unit) or allyl signals (3H/repeat unit). A sample NMR is shown in Figure 3-2. It is also important to note that the allyl group in PAGE can isomerize during the polymerization. However, as shown in Figure 3-2A, the isomer is also clickable, and is not expected to change the observed characteristics. The purified solutions were freeze dried to remove water and dried under high vacuum (<5mbar) for several days before being brought into an inert argon glovebox. Successful ion exchange and removal of excess salts was confirmed using inductively coupled plasma-optical emission spectroscopy (Varian). The synthesized Li$^+$-neutralized polyanions are given the acronym PAGELS (PAGE-lithium sulfonate).
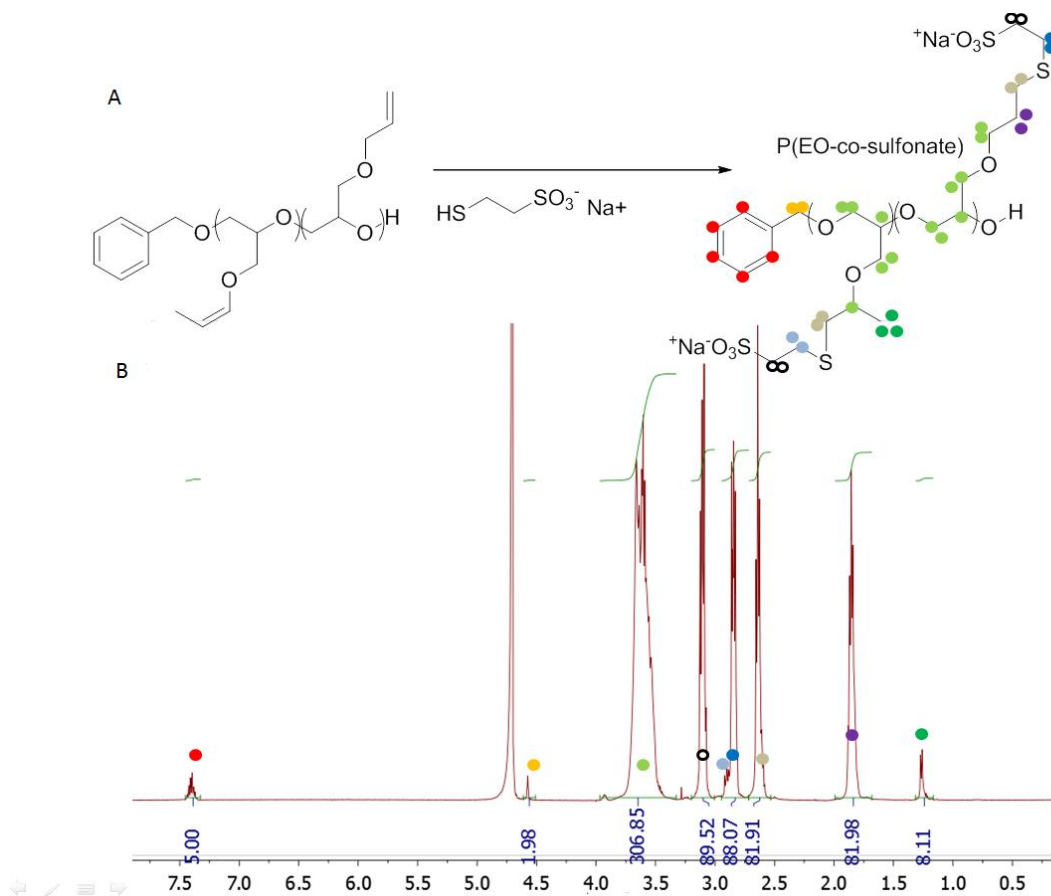
Figure 3-2 NMR of PAGELS in D$_2$O. A) The thioene click reaction on both PAGE and isomerized PAGE. B) ^{1}H NMR spectrum with peaks assigned.

3.3.2 *Solutions*

PAGELS and lithium bis(fluorosulfonyl)imide (LiTFSI) solutions were prepared in an argon atmosphere using anhydrous dimethyl sulfoxide (DMSO, Burdick and Jackson). Water content in these solutions was 20 ppm or less as confirmed by both Karl Fischer Titration (Metrohm) and ^{1}H NMR spectroscopy during the diffusion measurements. Solutions for NMR spectroscopy analysis were prepared in deuterated DMSO-d6 (Sigma Aldrich), and placed in a NMR tube sealed with a high pressure polyethylene cap before being removed from the glovebox for measurement. The molarities of the solutions were recorded with respect to lithium.

Water contamination was an important consideration in this study, as even small water impurities can influence Li$^+$ solvation and dramatically influence conductivity measurements. We present the following control measurements to support our contention that minimal water content (<15 ppm) was present in all PFG-NMR and conductivity measurements. To confirm the accuracy of our Karl Fischer water titration, a small, known amount of water (120 ppm) was added to nominally anhydrous DMSO. Karl Fischer Titration results for this 120 ppm H$_2$O control, as well as samples used for conductivity measurements, are shown in Table 3-2, and confirm the accuracy of the measurement.

Table 3-2. Measured water content in different solutions using Karl Fischer titration.

Sample	ppm [g/g]
Blank	0
120 ppm H_2O in DMSO	115
LiTFSI in DMSO	0
Na Thiol in DMSO	0
Polymer solution in DMSO	6

A representative NMR analysis of the 120 ppm water in DMSO control and an LiTFSI solution used for conductivity is presented in Figure 3-3. The ratio of the integrated area of the small H_2O peak at 3.6-3.8 ppm to the area of the DMSO peak (along with its satellite peaks) confirm the expected water content in each sample.
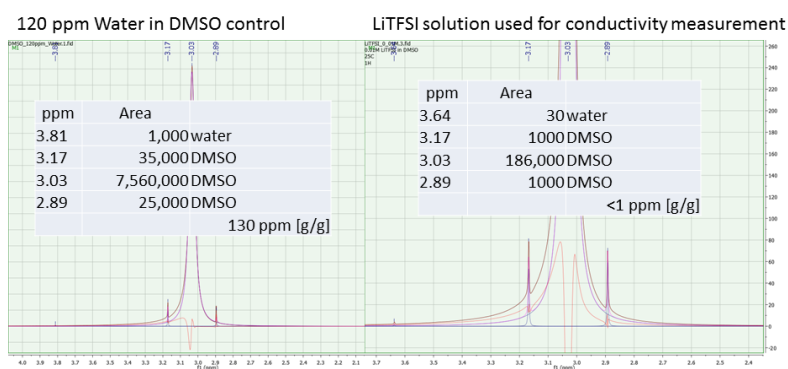
Figure 3-3. ^{1}H NMR of a DMSO sample contaminated with 120 ppm H_2O and a nominally anhydrous LiTFSI in DMSO solution. The water content calculated from the ratio of the water to DMSO peak areas is shown in each table.

Finally, we show in Figure 3-4 a representative analysis of the water content in a PFG-NMR sample. This sample does not have a large DMSO peak (centered at ~3.47 ppm) because it is performed in deuterated DMSO. It is therefore very easy to observe the water peak (sharp peak on the right, 1.33 ppm) when it exists. This is an example of a fairly high water content sample, which is still only 25 ppm water.
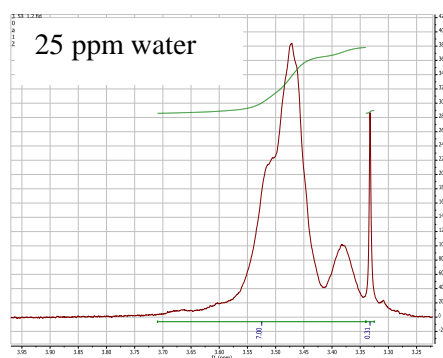
Figure 3-4. NMR spectrum showing 25 ppm water contamination in an electrolyte solution.

3.3.3 *Self-Diffusion Coefficients using Pulsed Field Gradient-Nuclear Magnetic Resonance (PFG-NMR)*

NMR measurements were performed on a Bruker Avance 500 MHz magnet with an Observe broadband high resolution probe with a Z-gradient. The strength of the Z-gradient was calibrated using DMSO-d6[40] and a lithium chloride solution,[41] the results of which are shown in Figure 3-5.
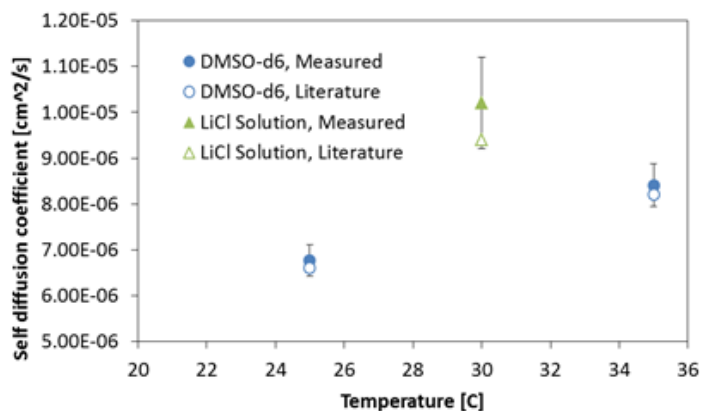
Figure 3-5 Calibration and validation of PFG-NMR measurements using DMSO-d6 and LiCl solutions.

The variable temperature unit maintained the temperature of the samples at 25⁰C to within 0.1 ⁰C during all measurements. Each sample was allowed to equilibrate at 25⁰C for 30 minutes before any measurements were made. The ^{1}H, ^{7}Li, and ^{19}F isotopes were studied to separately characterize the dynamics of the polymer, lithium cation, and perfluorinated anion, respectively. The 90⁰ pulse length was optimized for each sample at each temperature to achieve maximum signal. The T1 relaxation times were measured for each sample using inversion recovery (180-τ-90-acq.) to establish a sufficient delay time between scans. A double stimulated echo pulse sequence with bipolar gradients, eddy current delays, and convection compensation was used to measure diffusion coefficients[42,43]. Diffusion coefficients of the polyelectrolyte solutions were calculated from the relationship between the free diffusion echo signal attenuation, E, and the experimental parameters:

$$E = I/I_0 = \exp\left(-\gamma^2 \delta^2 g^2 D \left(\Delta + \frac{4\delta}{3} + \frac{3\tau}{2}\right)\right) \quad (3\text{-}1)$$

where *I* is the intensity of the resonant peak of interest, I_0 is the intensity at small gradient values, γ is the gyromagnetic ratio of the observed isotope, δ is the length of the bipolar gradient pulse, *g* is the gradient strength, Δ is the time between pulses, and τ is the gradient ringdown delay. For these experiments, Δ was varied between 0.1–0.5 s, τ was set to 0.002 s, and δ was varied from 0.005–0.050 s. The diffusion time Δ and gradient pulse length δ were independently varied to confirm that they do not affect the measured value of D, as shown in Table 3-3.

Table 3-3 Varying delay time in the PFG-NMR experiment does not affect the measured diffusion coefficient. Sample was PAGELS (n=500), 0.075M Li$^+$ in DMSO.

Δ (s)	δ (s)	D, 1H, (cm^2/sec)
0.4	0.008	4.13E-08
0.5	0.008	4.16E-08
0.5	0.011	4.04E-08
0.6	0.013	4.04E-08
0.7	0.015	4.05E-08

Each diffusion coefficient was determined by fitting the attenuated signal of 32 spectra of varying gradient strength (Figure 3-6A). A typical fit and the calculated diffusion coefficients for various protons along the PAGELS backbone and side chain are shown in Figure 3-6B & C. NMR spectroscopy measurements confirm that the calculated self diffusion coefficient of the polyanion is independent of which proton is traced, as is shown in Figure 3-6C. This fact supports that we are tracking true translational motion of the polymer instead of relative segmental dynamics. Importantly, given that the diffusion coefficient of all protons are equivalent regardless of the position of the proton on the polymer, we assume that the sulfonate anion diffusion coefficient, D_, is also equivalent to the diffusion coefficients measured at all other points on the polymer. The remainder of this study reports D_ values as measured from the methylene (H2) protons at 1.73 ppm because of the uniqueness of the protons at this chemical shift.

3.3.4 *Conductivity measurements*

A Metrohm 856 electrode conductivity probe (five electrode configuration), outfitted with a heating and chilling block and Teflon® vials was used to measure the ionic conductivity and temperature of solutions. Measurements were performed inside the glovebox (M-Braun LabMaster with continuous Ar recirculation through both solvent/H$_2$O and O$_2$ traps, with H$_2$O and O$_2$ both <0.1ppm) where the solutions were prepared. The temperature was held at 25°C and was controlled to within 0.1°C. The instrument was calibrated using an aqueous LiCl solution, and validated against literature values of LiTFSI in DMSO[44], as shown in Figure 3-7.

3.3.5 *Viscosity*

Viscosity measurements were made using a Cannon-Ubbelohde Semi-Micro Viscometer (size 50), immersed in a water bath to maintain the temperature at 25°C. Solutions were prepared in the glovebox and removed immediately before measurement to reduce atmospheric exposure. Viscosity measurements were validated against literature values for water and DMSO at several temperatures.
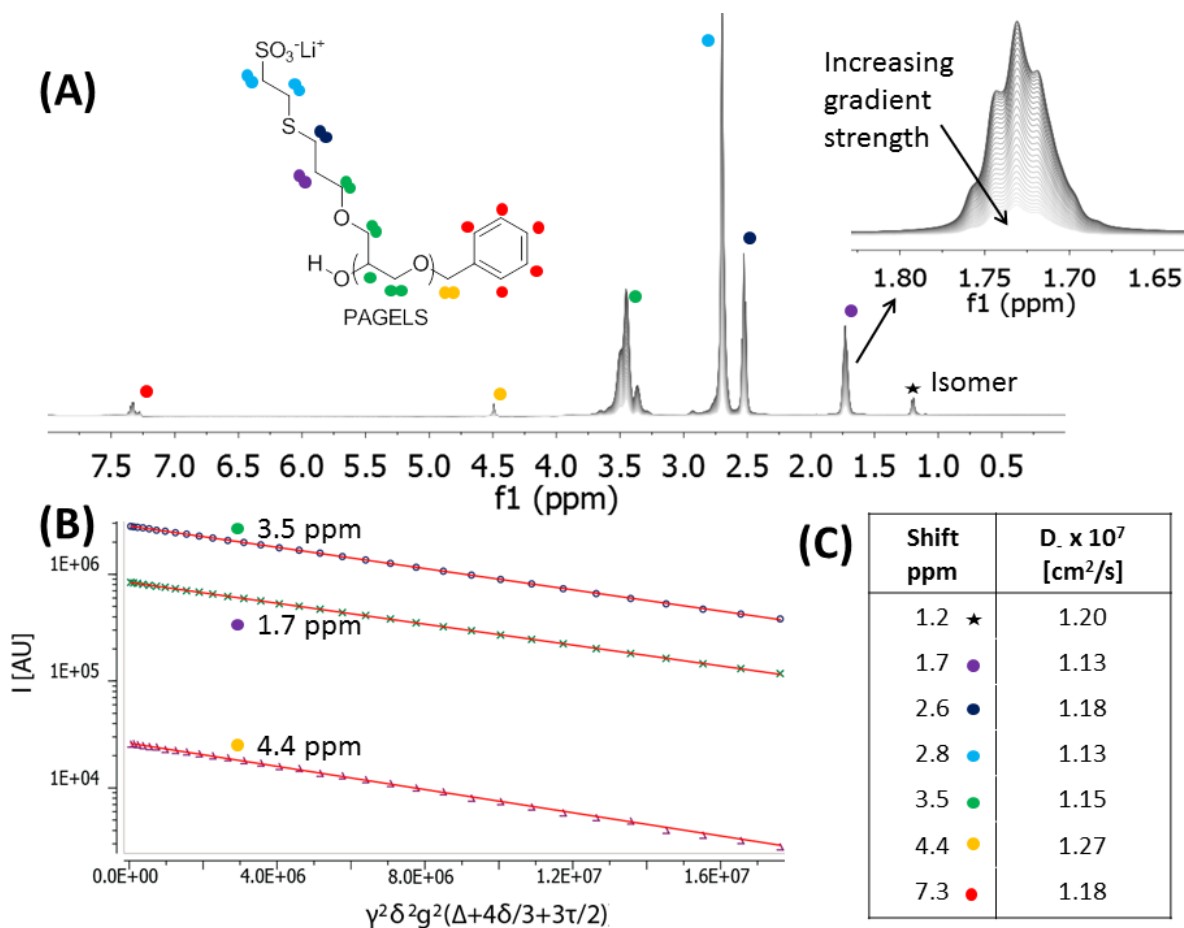
Figure 3-6 Representative PFG-NMR for self diffusion determination. A) PFG-NMR spectra of 0.5M PAGELS (n=43) solution in d6-DMSO. The stacked spectra of different intensities are at different gradient strengths. B) Integrated intensity of three of the peaks from A as a function of the exponent in equation 3-1. The red lines are best fits to equation 3-1 used to extract the self diffusion coefficients reported in C).
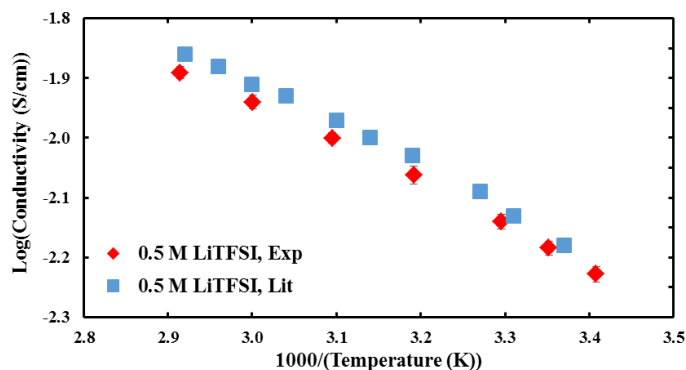
Figure 3-7 Validating conductivity measurements by comparison of literature and experimental data.

3.4   **Results and Discussion**

Figure 3-8 compares the transport properties of two series of solutions at 25 °C: A,C show PAGELS (n=43) dissolved in DMSO, and B, D show a common binary salt used in battery electrolytes, lithium bis(trifluoromethane)sulfonimide (LiTFSI), dissolved in DMSO. DMSO is used in this study because of its high Gutmann donor number (29.8), reflective of being a strong Lewis base, to allow solubility of the PAGELS over a wide concentration range with high dissociation of the lithium sulfonate. PAGELS was unfortunately found to be poorly soluble in carbonates and ethers (solvents more appropriate for Li battery electrolytes) given their low Lewis basicity and/or acidity. While ion dissociation will occur more readily in DMSO than in other solvents due to its high Lewis basicity, we believe that the trends in transference number and conductivity observed in DMSO can be realized in other solvents if polymers can be dissolved in them. Advances in polymer chemistry that allow polymer solubility in poor Lewis base/acid solvents are necessary and are currently being developed in our laboratory. Figure 3-8A shows the self-diffusion coefficients of the anions (D_-) and the lithium cation (D_+) as measured by PFG-NMR. While D_+ only drops by a factor of two by switching from the TFSI anion to the polymer anion, the anion self-diffusion coefficient drops by more than an order of magnitude. This demonstrates that by shifting from a small molecule anion to a large, polymeric anion, selective, and substantial, restriction of anion mobility can be achieved.
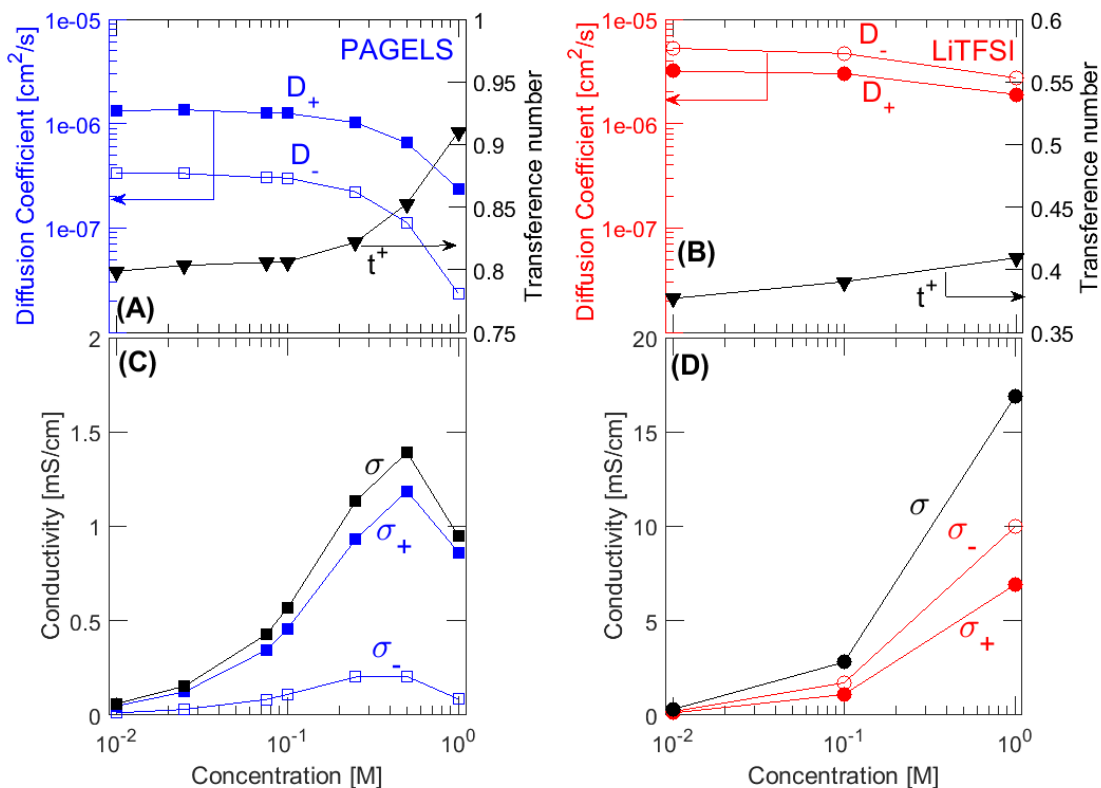
Figure 3-8 Solution properties of PAGELS (n=43) (A, C) and LiTFSI (B, D) at 25 °C in DMSO. A) and B) Self-diffusion coefficients, as measured using PFG-NMR, of the Li^+ (D_+) and anion (D_-) and the Li^+ transference number (t_+). C) and D) Conductivities as calculated from diffusion coefficients acquired using PFG-NMR using the Nernst-Einstein relationship, equation 3-3.

21

As seen in other semidilute polyelectrolyte solutions, there is a regime (0.01–0.5 M Li$^+$) where the PAGELS self-diffusion coefficients are independent of concentration. For this semidilute regime, the increase in solution viscosity with concentration is offset by a decrease in effective chain radius of gyration due to increased electrostatic screening, causing the diffusion coefficient to remain constant.[45,46] At 0.5 M, the self-diffusion coefficients for both ions drop sharply, corresponding with the crossover into a regime where physical polymer obstructions cause self-diffusion to drop with concentration.[45,46]

Figure 3-8B shows the cation transference numbers, t_+, or the fraction of ionic current that was carried by lithium, as calculated by equation 3-2 for a dilute binary 1:1 electrolyte:

$$t_+ = \frac{D_+}{D_+ + D_-} = \frac{\sigma_+}{\sigma_+ + \sigma_-} \quad (3\text{-}2)$$

where σ_+ and σ_- were the ionic conductivities due to the cation and the anion, respectively, in a solution of uniform composition. The polymer solutions exhibited very high t_+, 0.80 or above for all concentrations, and reaching 0.91 at 1.0 M. As seen in other binary salt electrolytes, t_+ of LiTFSI solutions are low at *ca.* 0.4.[47,48]

The self-diffusion coefficients are related to the ionic conductivity through the Nernst-Einstein relation for a dilute, binary 1:1 electrolyte:

$$\sigma = \frac{F^2 C}{RT}(D_- + D_+) = \sigma_- + \sigma_+ \quad (3\text{-}3)$$

where F is Faraday's constant, C is concentration of the salt (which, for a 1:1 electrolyte, is the concentration of Li$^+$), R is the universal gas constant, T is temperature, and σ_i is species i contribution to the overall conductivity[49]. The ionic conductivities of the polymer solutions calculated from PFG-NMR spectroscopy using this relationship are shown in Figure 3-8C. As expected from the high t_+ of these solutions shown in Figure 3-8B, the contribution of the polymer anion to overall ionic conductivity is much lower than that of the lithium cation. It is also important to note that, as is the case of many binary salt polymer electrolytes, the ionic conductivity passes through a maximum with concentration[3,50]. Despite this maximum, the ionic conductivities reached with this system are quite high, reaching over 1 mS/cm at 0.5 M and 25 ℃, which is expected to be sufficiently high for battery applications[51].

Due to non-idealities in experimental systems, such as incomplete ion dissociation[25,52,53] and concentrated solution effects,[49,54] it is important to evaluate the validity of the Nernst-Einstein relationship in this system, which is strictly valid only in the dilute solution regime. To this end, Figure 3-9 compares the conductivity as calculated using the Nernst-Einstein relationship to conductivity measured directly using a conductivity probe. This comparison is important because NMR spectroscopy measures the self-diffusion of all species of a particular nucleus, regardless of charge state or ion pairing. Conductivity measurements using an electric field probe the true ionic mobility of charged species in solution, and no conductivity contribution from ion pairs (condensed ions) would be observed given that ion pairs are uncharged species. The conductivities calculated from the Nernst-Einstein equation using the PFG-NMR diffusion coefficients show good agreement with the measured conductivity, particularly for the polymer solutions. However, at high salt concentrations the two methods begin to deviate by a small amount, with the NMR spectroscopy measurements overestimating the conductivity. This overestimation at high polyanion concentrations in solution is expected because ion condensation increases with increasing concentration.
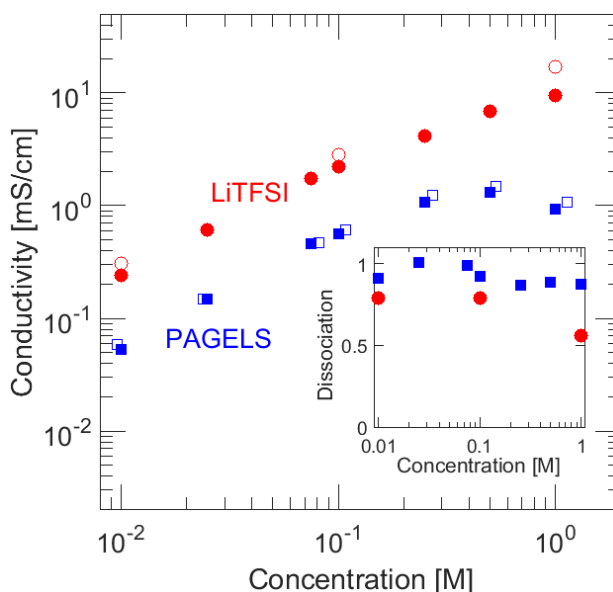
Figure 3-9 Conductivity of solutions in DMSO at 25 °C. Blue squares are PAGELS (n=43) solutions, red circles are LiTFSI. Filled points are data collected from a conductivity meter while empty points are conductivities calculated from NMR measurements. Inset shows the extent of ion dissociation in the same solutions as calculated using equation 3-4.

NMR measurements capture motion of these associated ions during the diffusion measurements, whereas associated ions will not contribute to measured ionic conductivity. It is typical to calculate ion dissociation by assuming the difference between the calculated conductivity from NMR-measured diffusion coefficients and actual conductivity measurements is entirely related to ion condensation. We therefore use the following simple relationship to calculate ion dissociation:

$$\alpha = \frac{\sigma_{probe}}{\sigma_{NMR}} \qquad (3\text{-}4)$$

Where α is the degree of ion dissociation, σ_{probe} is the conductivity as measured using a conductivity meter, and σ_{NMR} is calculated from equation 3-3 using the diffusion coefficients measured using PFG-NMR. The inset in Figure 3-9 shows the degree of dissociation for the LiTFSI and PAGELS solutions. When compared to LiTFSI dissociation observed in a variety of solvents in a previous study[47,55], the degree of dissociation observed in the LiTFSI solutions is consistent with what would be expected in a high Lewis basic, high dielectric constant solvent. LiTFSI's lower degree of dissociation, particularly at 1 M, also implies that the transference numbers calculated from NMR-measured diffusion coefficients are actually slightly larger than would be observed using electrochemical techniques. The degree of dissociation in the PAGELS solutions is higher, implying that DMSO is better solvent for dissociation of sulfonate-based salts compared to imide-based salts.
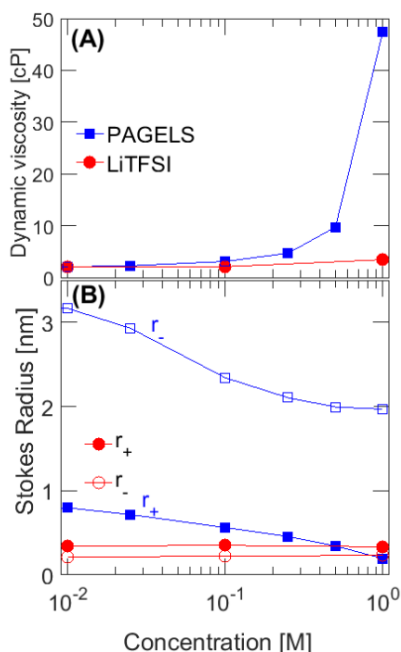
Figure 3-10 Viscosity (A) and cation and anion Stokes radii (B) of PAGELS (n=43) (blue squares) and LiTFSI (red circles) solutions at 25 °C. In B, filled points are data for cations and empty points are data for anions.

It is also seen in Figure 3-9 that, similar to other polymer electrolytes[3,4,56], these polyelectrolyte solutions go through a maximum in conductivity as a function of concentration. The source of this maximum is clear when considering the viscosity of the solution, as is shown in Figure 3-10A. The dynamic viscosity of the solution spikes sharply as the Li^+ concentration approaches 1.0 M, likely a result of the onset of polymer chain entanglement. This increase in viscosity substantially reduces ion mobility, thereby resulting in an overall decrease in conductivity even though the overall concentration of ions is increasing. There was no corresponding increase in the viscosity of LiTFSI solutions at high concentrations and hence no maximum in conductivity was observed over the concentration range explored.

Figure 3-10B plots the Stokes radius of each ion in solution as a function of concentration, as calculated from the Stokes-Einstein equation:

$$r = \frac{k_B T}{6\pi\eta D} \qquad (3\text{-}5)$$

where η is the dynamic viscosity from Figure 3-10A, and k_b is the Boltzmann constant. The Stokes radii of the Li cation in the LiTFSI solutions, and the TFSI anion itself, follow the expected trends and suggest that these ions can be treated as non-interacting spheres. For these LiTFSI solutions, the radii did not change as a function of concentration, and the effective radius of the lithium cation (*ca.* 0.3nm) was larger than that of the TFSI counter ion (*ca.* 0.2nm)[47].

The calculated Stokes radii of charged species in the PAGELS solutions showed intriguing trends. We only briefly comment on these trends and offer potential explanations that would require subsequent

studies for confirmation. As expected and previously observed, the polyanion was much larger than all of the small molecule ions, and decreased in size with increasing concentration before reaching a plateau at 0.5–1.0 M. However, a corresponding decrease in the Li^+ Stokes radius is surprising and suggests that the dynamics of the cation motion are different than that of the cation motion in the LiTFSI solution. While the size and diffusion properties of polyanions have been previously studied[45,46,57–62], there is a distinct lack of understanding of the counterion dynamics. Similarly to Schipper et al.[63], we do not propose that the solvation shell (or the size) of the solvated cation is decreasing as concentration increases. Instead, we note that the derivation of the Stokes-Einstein equation does not consider important localized electrostatic interactions that influence ion mobility. We therefore suggest that both electrostatic and hydrodynamic interactions cause the local viscosity experienced by a diffusing lithium ion to be higher than the bulk viscosity of the solution measured using a viscometer. This difference between local and bulk viscosity is likely due to electrostatic friction[60,61,64]. At low concentrations, the Debye electrostatic screening length, which scales with $C^{-0.5}$, is large, so electrostatic interactions of Li^+ with the large, slow anions cause more friction and therefore results in a large apparent Stokes radius. As concentration increases, the Debye length decreases, lessening the electrostatic interactions and decreasing the apparent Li^+ Stokes radius. In the case of the LiTFSI solutions, no change in the apparent Stokes radius is observed with increasing concentration, implying that electrostatic friction between the ions is substantially smaller compared to the PAGELS solutions. This observation is likely due to the smaller difference in diffusion coefficients of the cations and anions in the LiTFSI solution compared to the PAGELS solution: the smaller, faster anions in the LiTFSI solution result in less electrostatic friction exerted on the Li^+ ions. At high concentrations, an intriguing observation is that the apparent Stokes radius of the Li^+ in a 1M PAGELS solution is calculated to be smaller than the Stokes radius of Li^+ in a 1M LiTFSI solution. The cause of this observation is unknown, but implies that the Li^+ diffuses faster than predicted by the Stokes-Einstein relation.

Figure 3-11 explores the relationship between polymer molecular weight and electrolyte σ and t_+, both calculated from D_+ and D_- measured by PFG-NMR spectroscopy. The changes in conductivity with molecular weight of the polymer were surprisingly small. In addition, all polymers exhibited the same general behavior of increasing conductivity with concentration until reaching a maximum of 1.5 mS/cm at 0.5 M. However, Figure 3-11B shows that the molecular weight has a very large effect on t_+, with the largest PAGELS molecular weight achieving $t_+ = 0.99$ at 1.0 M [Li^+]. Increasing the molecular weight of the polymer at a given concentration beneficially increases t_+ without significantly decreasing the conductivity. These tradeoffs will be explored in more detail in the next chapter.
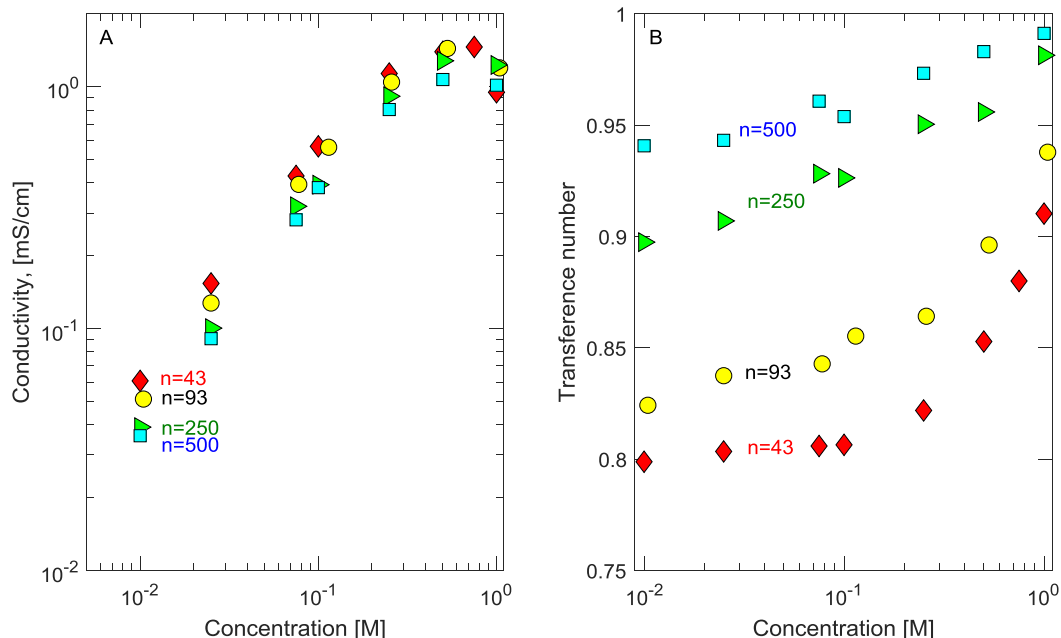
Figure 3-11 PAGELS molecular weight dependence of conductivity calculated from NMR-measured self diffusion coefficients (A) and Li⁺ transference number (B). The red diamonds are PAGELS (n=43), yellow circles are PAGELS (n=93), the green triangles are PAGELS (n=250) and blue squares are PAGELS (n=500).

3.5 **Conclusions**

This work presents a new approach to the ideal marriage of both high ionic conductivity and high transference number in liquid electrolytes for battery applications. By replacing the small molecule anion typically used in battery electrolyte solutions (*e.g.*, TFSI, PF_6) with a polyanion, the self-diffusion coefficient of the anion in solution can be decreased by more than an order of magnitude without a substantial decrease in the self-diffusion of the lithium cation. Using a model system of functional polyether with pendant lithium sulfonate moieties dissolved in a polar aprotic solvent (DMSO), it was shown that high Li^+ transference numbers (0.80–0.99, Figure 3-11B) and high ionic conductivity (of order 1 mS/cm, Figure 3-11A) at room temperature could be achieved. This is among the highest combination of transference number and conductivity in a liquid electrolyte reported in the literature. Additionally, our approach is modular, versatile, and could be utilized using a variety of different polymer backbones, pendant anions, solvents, molecular weights, and formulations, making it an ideal platform for exploring this new paradigm of battery electrolyte. In the next chapter, we will test some of these options, and suggest future directions for improving this electrolyte system.

4 Transport properties of polyelectrolyte solutions with varying temperature and composition

4.1 Abstract

In the last chapter, I introduced the idea of using polyelectrolyte solutions as an electrolyte for lithium batteries. Using polyelectrolyte concentration and molecular weight as variables, the polyelectrolyte solutions were found to exhibit tunable, although always high, Li ion transference numbers (t_+) (0.8-0.99) with conductivities approaching that of common binary salt liquid electrolytes (maximum of 1.5 mS/cm). In this chapter, we use the same Li^+-neutralized polyanion as the previous chapter, poly(allyl glycidyl ether-lithium sulfonate) (PAGELS), to explore the influence of temperature, PAGELS molecular weight, solvent choice, and small molecule salt addition on polyelectrolyte solution transport properties. I will demonstrate that the cation transference number is temperature independent, as is expected for solutions that are fully dissociated at all temperatures measured. Next, I present scaling theories for molecular weight dependence of diffusion coefficients, showing that the theories describe the polymer behavior well but that a simple scaling model developed for Li^+ transport does not capture experimentally observed trends, indicating that more detailed theories should be developed for Li^+. I explore the effect on transport of several different solvents, concluding that while all have high t_+ and high conductivity, there is no simple relationship between solvent properties and electrolyte transport properties. Finally, I test the hypothesis that small molecule salts, such as lithium bis(trifluorosulfonylimide) (LiTFSI), when mixed into the polyelectrolyte solution at small concentrations, can increase conductivity while having minimal effect on the overall t_+. I instead find that only a minor increase in conductivity and moderate decrease in t_+ is observed in this case. Transport properties of polyelectrolyte compositions in which TFSI comprised a moderate to large fraction of the overall anion content were dominated by the TFSI rather than the polyanion, such that these solutions exhibited high conductivity but low t_+.

4.2 Motivation

One of the attractive aspects of employing polyelectrolyte solutions is the ability to potentially optimize the inherent tradeoff between transference number and conductivity in a way that is inaccessible in any other electrolyte system. Small molecule lithium salts dissolved in organic solvents or polymers suffer from low t_+, with minimal ability to increase t_+ above 0.5. Single ion conducting solid polymers or gels have a t_+ fixed at 1, but conductivities which are extremely low and difficult to increase. As shown in the previous chapter, the polyelectrolyte system studied is tunable by simply varying molecular weight and concentration. For example, both conductivity and t_+ increased with increasing polyanion concentration, while increasing the polyanion molecular weight increased t_+ while not dramatically changing conductivity. In this chapter, I explore the influence of different polyelectrolyte solution composition parameters on t_+ and conductivity.

Currently, there is a lack of understanding as to how tradeoffs in t_+ and conductivity affect battery performance. It is clear that a t_+ of 1 is superior to a t_+ of 0.35 (if both electrolytes had similar conductivities), but it is unclear how much better a transference number of, *e.g.*, 0.99 is than a t_+ of 0.97. These questions have not been addressed because no other electrolyte solution has approached the combination of high t_+ and conductivity that these polyelectrolyte solutions possess, while polyelectrolytes also allow each transport property to be independently tuned through simple composition

modifications. Now that we have shown that high t_+ and conductivity are possible, it is important to understand physical polyelectrolyte solution design rules and how they may affect tradeoffs between conductivity and t_+. In this chapter, I will explore the influence of temperature, polyanion molecular weight, solvent choice, and addition of small molecule salt on transport properties with the end goal of gaining a better understanding of how to optimize t_+ and conductivity in these systems.

4.3   Temperature dependence of transference number

4.3.1   *Theoretical background*

The dependence of transference number on temperature is important to understand because in real applications, a battery's operational temperature will likely fluctuate substantially during its operational lifetime. From a physical perspective, the temperature dependence of t_+ can be understood using two different approaches, both starting with well-established theories that describe how the self diffusion coefficients of the cation (D_+) and polymer anion (D_-) scale with temperature. The first approach starts with the Stokes Einstein equation, which is a simple model that predicts how spherical particles would diffuse in a viscous media[65]:

$$D_{AB}(T) = \frac{k_B T}{\mu_B(T) 6 \pi R_A} \quad (4\text{-}1)$$

where T is temperature, R_A is the particle's Stokes radius, and k_B is the Boltzmann constant. $D_{AB}(T)$, the diffusion coefficient of molecule A through solvent B, and $\mu_B(T)$, the viscosity of the solvent B, are both expected to change with temperature while under ideal conditions, the other parameters are not. Rearranging, we can show that

$$\frac{D_{AB}(T_1)}{D_{AB}(T_2)} = \frac{T_1}{T_2} \frac{\mu_B(T_2)}{\mu_B(T_1)} \quad (4\text{-}2)$$

Using this relationship and the definition of transference number (equation 3-2), we can see that the cation transference number is expected to be temperature independent if the polymer's effective Stokes radius is independent of temperature:

$$t_+(T_1) = \frac{D_+(T_1)}{D_+(T_1)+D_-(T_1)} = \frac{D_+(T_2)\left(\frac{T_1}{T_2}\right)\frac{\mu(T_2)}{\mu(T_1)}}{D_+(T_2)\left(\frac{T_1}{T_2}\right)\frac{\mu(T_2)}{\mu(T_1)}+D_-(T_2)\left(\frac{T_1}{T_2}\right)\frac{\mu(T_2)}{\mu(T_1)}} = t_+(T_2) \quad (4\text{-}3)$$

However, as was shown in the previous chapter, Stokes-Einstein theory may be too simplistic to entirely capture all physical phenomena that influence species diffusion in polyelectrolyte solutions. It is therefore useful to evaluate the temperature dependence of these diffusion coefficients through another approach. While the Stokes Einstein equation is derived for a sphere moving through a solution at low Reynolds number, it has also been proposed to instead fit the temperature dependence of diffusion coefficients to the empirical Vogel-Fulcher-Tammann (VTF) equation[52,66,67].

$$D = D_0 \exp\left(-\frac{B}{T-T_0}\right) \quad (4\text{-}4)$$

Here, D is a species self diffusion coefficient, D_0 is the VTF pre-exponential factor, T_0 is the Vogel temperature, and B is inversely related to the fragility of the liquid, where fragility is a liquid property that

describes the deviation from ideal behavior. As I will show, the self diffusion coefficient of each species in the solution is expected have its own pre-exponential factor (*e.g.*, D_{0+} and D_{0-} for the cation and anion, respectively), but because B and T_0 are properties of the solution, these should be the same for all species in a given solution. This gives us the following forms of D_+ and D_-:

$$D_+ = D_{0+} \exp\left(-\frac{B}{T-T_0}\right) \qquad \text{(4-5a)}$$

$$D_- = D_{0-} \exp\left(-\frac{B}{T-T_0}\right) \qquad \text{(4-5b)}$$

It becomes apparent from these equations that the pre-exponential factors, D_{0-} and D_{0+} are the upper bound on the diffusion coefficient of that species, or, the self diffusion coefficient of that species as temperature approaches infinity. Using these equations and the definition of t_+, we again find that t_+ is temperature independent:

$$t_+ = \frac{D_+}{D_+ + D_-} = \frac{D_{0+} \exp\left(-\frac{B}{T-T_0}\right)}{D_{0+} \exp\left(-\frac{B}{T-T_0}\right) + D_{0-} \exp\left(-\frac{B}{T-T_0}\right)} = \frac{D_{0+}}{D_{0+} + D_{0-}} \qquad \text{(4-6)}$$

While these derivations are general to both polymeric and small molecule salts, they break down when there is incomplete salt dissociation. This is because the D_+ and D_- measured by NMR becomes an average of the diffusion coefficient of the dissociated and the associated species, and the degree of dissociation will also be influenced by temperature.

4.3.2 *Experimental verification*

Figure 4-1 shows that experimentally we see no temperature dependence in the polyelectrolyte solutions over a range of concentrations (0.01-1M Li$^+$), molecular weights (43-500 repeat units), and temperatures (25-70°C). Such a trend has been seen in sulfonimides dissolved in PEO, a system which has complete ion dissociation[68]. We showed in the previous chapter that the polymer solutions are well dissociated, so we also expected t_+ of this system to be temperature independent. Given the expected lack of temperature dependence, it is not surprising that these polymer solutions do in fact follow VTF behavior (Figure 4-2). Figure 4-2A shows fits for the n=500 PAGELS solutions at different concentrations, while Figure 4-2B and C shows the extracted fits to equation 4-5. These fits confirm that B is the same for both the cation and the anion, and hence a property of the solution, while the pre-exponential factor is specific to each ion. D_{0+} is approximately 3×10^{-5} cm^2/s while D_{0-} is 10^{-6} cm^2/s and decreases with concentration.

Whereas t_+ for a given polyelectrolyte solution was found to be independent of temperature, small molecule salt solutions, specifically LiTFSI in DMSO, were found to have temperature-dependent t_+ (Figure 4-3). t_+ of the most dilute (0.01M) LiTFSI solution has a slight temperature dependence, with t_+ increasing slightly with temperature. The most concentrated solution (1M) has a much stronger dependence on temperature, but follows the same trend, with the highest t_+ at the highest temperature studied (60°C). This temperature dependence is not unexpected, because, as was shown in the previous chapter, the degree of dissociation in the LiTFSI solutions at 25°C is much lower than for the polymer solutions, around 0.7 for 0.01M and almost 0.5 at 1M. The degree of dissociation is expected to change with temperature, which will influence the measured t_+ depending on the relative diffusion of the ion paired and dissociated species. However, the diffusion coefficients of the dissociated species should scale
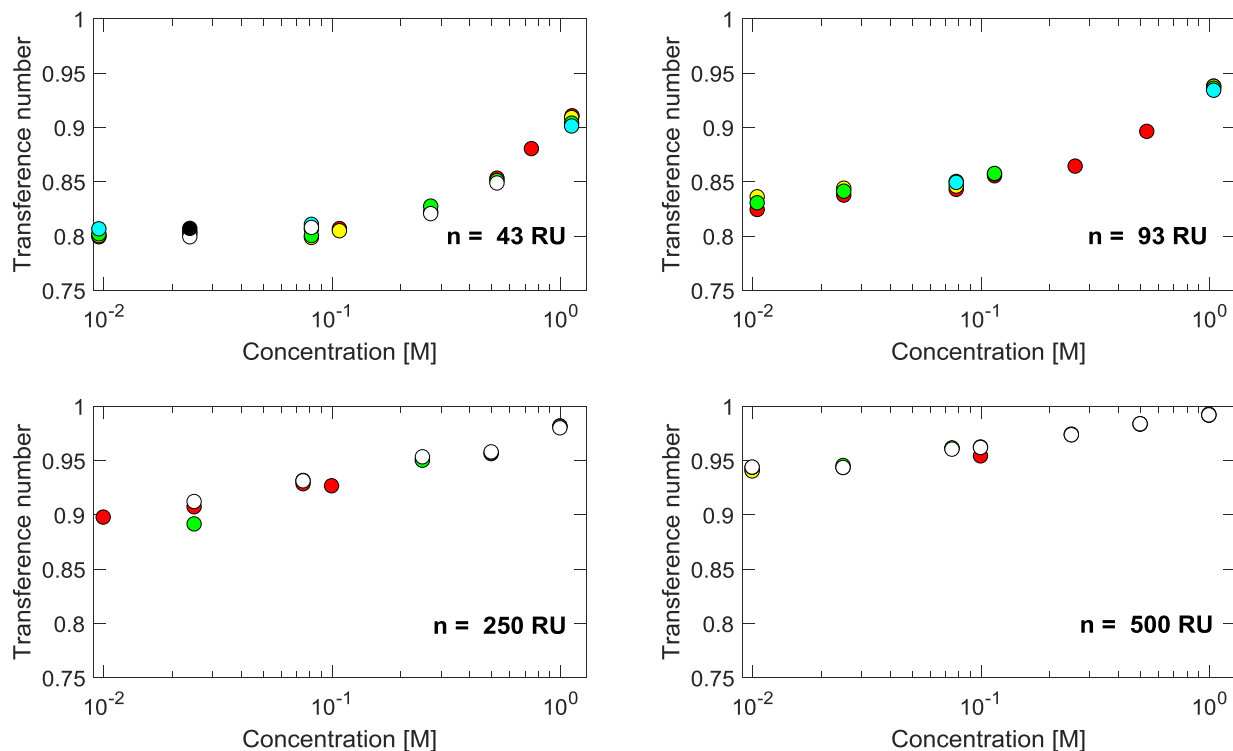
Figure 4-1 Transference number of polyelectrolye solutions at different molecular weights (n=43, 93, 250, 500 in each graph), concentrations (abscissa of each graph), and temperatures (25-70°C as shown in the different color circles). The transference number is independent of temperature for any given polyelectrolyte solution composition between 25 and 70°C.

similarly with temperature (equations 4-5a and 4-5b), and it is therefore expected that t_+ measured electrochemically (which only measures transport of dissociated charged species) would be temperature independent, even for LiTFSI solutions. This hypothesis is not tested here, as it is beyond the scope of this thesis, but would be useful to confirm for general electrolytic solutions.
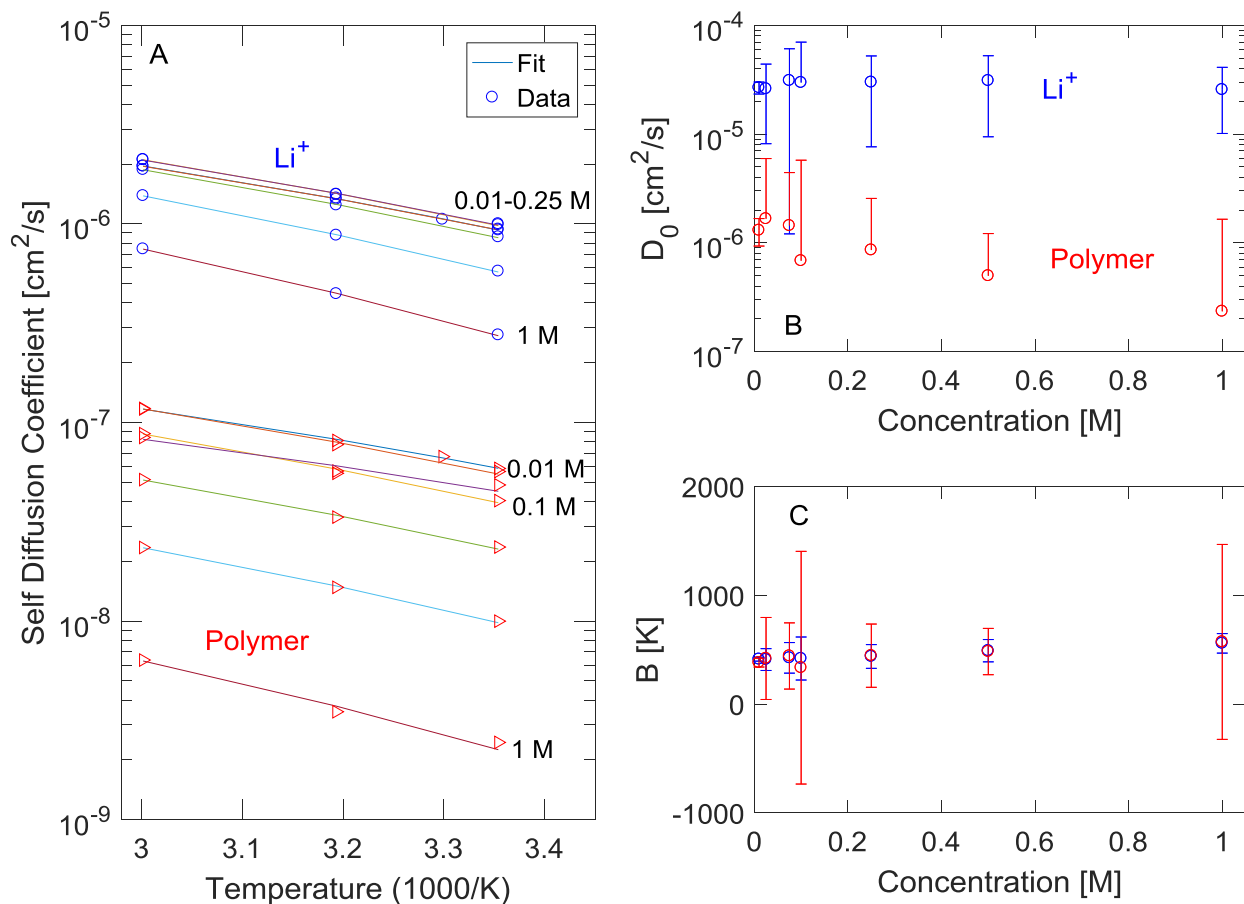
Figure 4-2 Vogel-Fulcher-Tammann (VTF) fits to diffusion coefficients of n=500 PAGELS solutions. A) Diffusion coefficients as a function of inverse temperature. Blue circles are experimental data from PFG-NMR of the lithium cation while red triangles are of the polymer anion. Lines are data fit to equation 4-5 with T_0 fixed at 150 K. Different lines are at different concentrations, 0.01-1M. Fit parameters extracted from the fit to equation 4-5 as a function of concentration are shown in B) Prefactor and C) inverse fragility. In both plots, Li^+ is in blue and polymer anion is red, and error bars are 95% confidence limits of the nonlinear fits. In B the bottom 95% confidence limits on $D_{0\cdot}$ are not shown because the value goes to zero. More temperature points would be needed to improve quality of the fit.
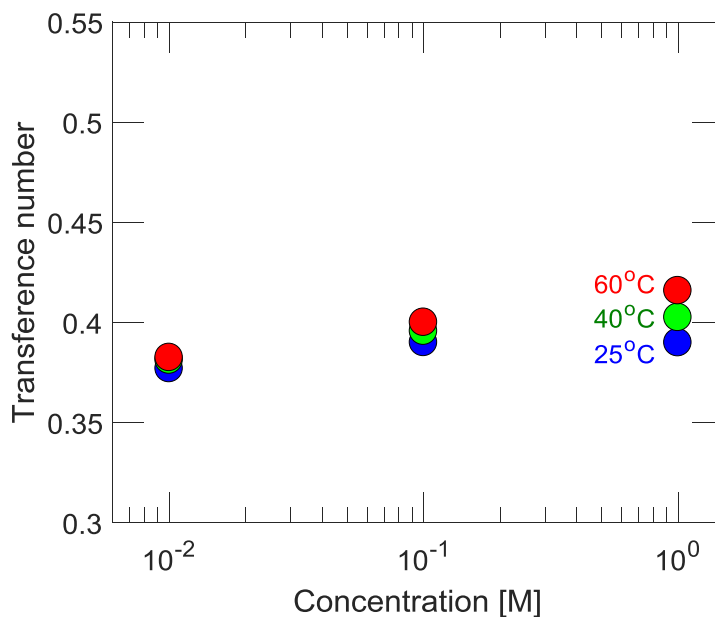
Figure 4-3 Transference number of LiTFSI solutions at 25 (blue circles), 40 (green circles), and 60°C (red circles). At low concentrations the transference number is less sensitive to temperature than at high concentrations. At all concentrations, the lowest transference number is at 25°C and the highest is at 60°C.

4.4   **Molecular weight dependence of transference number**

The molecular weight dependence of transference number can predicted using scaling laws for diffusion developed for polyelectrolyte solutions[46,58,59,63,69–71]. While there are a number of theoretical[58,59,72] and computational[69,73,74] studies that characterize diffusion of charged polymers in solutions, there are substantially fewer experimental studies, most of which are performed in aqueous electrolytes[45,46,75,76]. With two   exceptions[46,63], the focus of these studies is on the behavior of the polymer and not the counterion, The transport properties of both are obviously required to understand the transference number scaling behavior. In this section, I will first focus on the polyanion behavior, both from a theoretical and experimental standpoint, and show that our solutions follow the expected behavior predicted from scaling theory. To my knowledge, this is the first experimental verification of scaling behavior of polyelectrolyte self diffusion coefficients with polyelectrolyte molecular weight in a non-aqueous solution. Next, I will address the behavior of the lithium cation, showing that the experimental scaling does not match the expected trend with polyelectrolyte molecular weight, mostly due to a lack of detailed scaling laws. Finally, I will comment on the consequences of these scaling laws on the overall dependence of t_+ as a function of polyelectrolyte molecular weight.

4.4.1   *Diffusion of PAGELS polyanion dissolved in DMSO*

As was similarly observed by Oostwal *et al.* in aqueous solutions of polystyrene sulfonate, PAGELS-DMSO solutions are in the semidilute unentangled regime in the concentration range of 0.01-0.25 M Li$^+$. This regime is characterized by a reasonably constant polymer self diffusion coefficient throughout the 0.01-0.25 M concentration range (Figure 4-4A). These solutions cross over into the entangled regime above 0.25M, as characterized by the sharp drop in polymer self diffusion coefficient (Figure 4-4A) and

viscosity (previous chapter). We will focus on the untentangled regime for its importance in polymer physics and evaluate the validity of established scaling theory that predicts the relationship between diffusion coefficient and polymer molecular weight[58,69,70]. Unfortunately, I do not have sufficient data in the entangled regime to evaluate the validity of esablished model in that range.
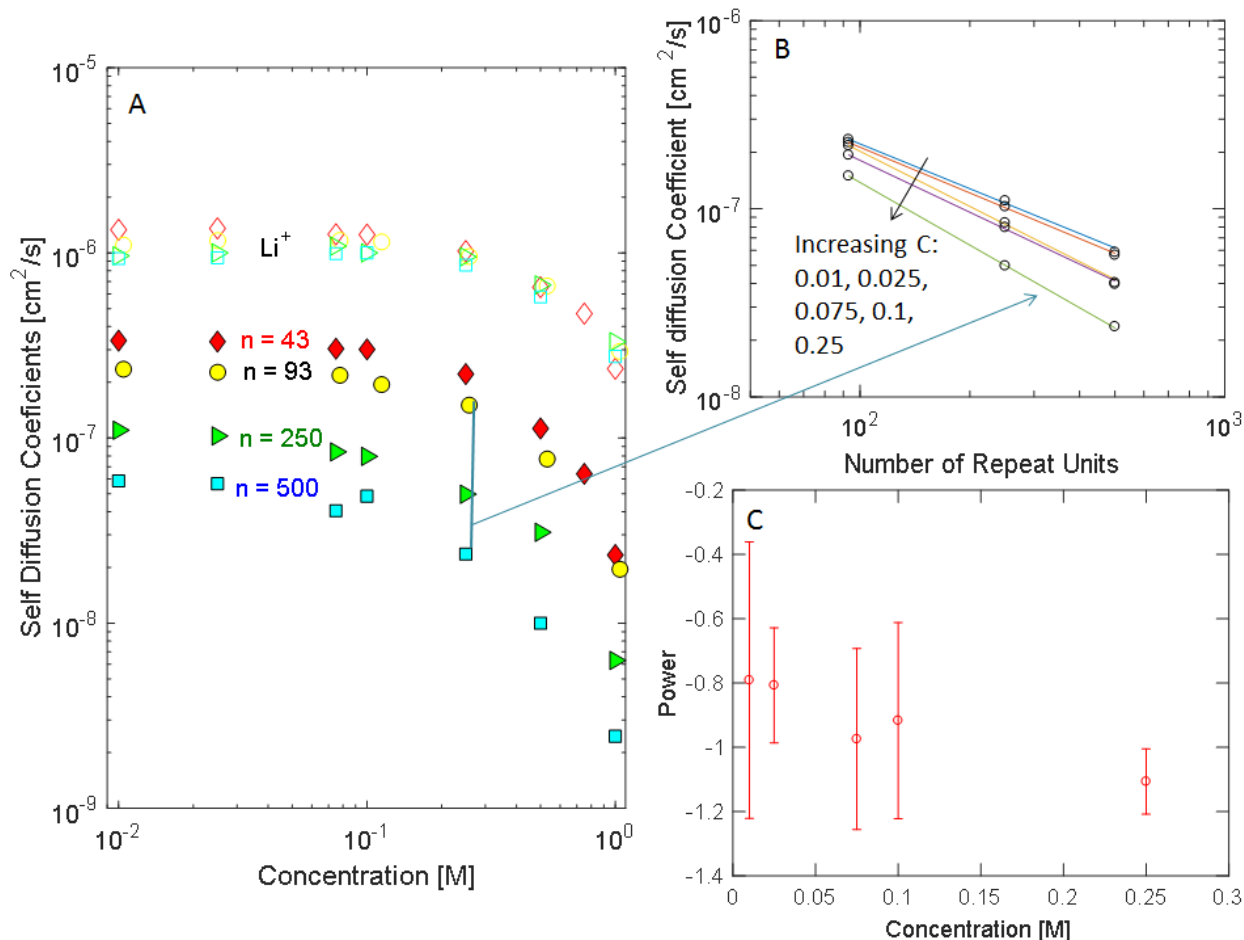
Figure 4-4 Scaling of polymer self diffusion coefficient with polymer molecular weight. A) Self diffusion coefficients as a function of concentration for solutions containing four different molecular weight polymers. PAGELS diffusion coefficients are filled while those for lithium cations are unfilled. B) Self diffusion coefficients of PAGELS polymers as a function of the number of repeat units at different concentrations. Circles are experimental data while the lines are best fits to equation 4-10. C) Shows the value of z from fits shown in B). This is the power of the molecular weight dependence of the self diffusion coefficient. Error bars are 95% confidence limits.

In the semidilute unentangled regime, the polymer follows Rouse-like behavior and can be modeled using the bead and spring model, which provides τ, the polymer relaxation time[77]. Physical arguments that describe Coulomb interactions, electrostatic screening, and random walk statistics are used to predict the chain size, R. Using τ and R, the self diffusion coefficient of the polymer (D) is expected to follow the scaling law:

$$D_{polymer} \approx \frac{R^2}{\tau} \approx \left(\frac{k_B T}{\eta_s}\right)\frac{B}{bN} \propto N^{-1}c^0 \qquad (4\text{-}7)$$

33

Where η_s is the solvent viscosity, b is monomer size, N is degree of polymerization, and B is a parameter that describes the solvent quality[70]. It is very unusual and surprising for the self diffusion coefficient to have no dependence on concentration (c), but this is both predicted and observed previously for charged polymers in aqueous solutions[45], and here in nonaqueous solutions (Figure 4-4A). It is also useful to note that the solvent quality has a large effect on the polymer conformation, both because of interactions with the polymer backbone and ion solvation.

In order for the Rouse model to apply, we must consider the range of polymer chain lengths in which the model is valid. The characteristic time (τ) is calculated for a chain segment that is usually a few times larger than the polymer persistence length. For flexible, uncharged polymers (*e.g.*, polystyrene or polyethylene oxide), the persistence length is on the order of 0.5 nm. However, charges along the backbone increase the polymer persistence length to a value that can be estimated using the following model[78]:

$$L_{Total} = L_P + L_{P,es} = L_P + \frac{\lambda_B}{4\kappa^2 A^2} \qquad (4\text{-}8)$$

where L_{Total} is the total persistence length, while L_P is the persistence length of the bare backbone and $L_{P,es}$ is the electrostatic contribution to persistence length. λ_B is the Bjerrum length (equation 4-9A), A is the contour distance between adjacent charges, and κ^{-1} is the Debye-Hückel shielding length (equation 4-9B).

$$\lambda_B = \frac{e^2}{4\pi\varepsilon_0\varepsilon_r k_B T} \qquad (4\text{-}9A)$$

$$\kappa^{-1} = \sqrt{\frac{\varepsilon_r\varepsilon_0 RT}{2F^2 C_0}} \qquad (4\text{-}9B)$$

where e is the elementary charge, ε_r is the dielectric constant, ε_0 is the permittivity of free space, F is the Faraday constant, and C_0 is the molar concentration of the electrolyte. The Debye screening length and the total persistence length of the polyelectrolyte solutions are shown in Table 4-1.

Table 4-1 Debye screening length and calculated persistence length of PAGELS solutions in dimethyl sulfoxide (DMSO) at 25°C.

Concentration [M]	Debye Screening length [nm]	L_{total} [nm]
0.010	2.3	8.9
0.025	1.5	3.8
0.075	0.9	1.5
0.100	0.7	1.3
0.250	0.5	0.8
0.500	0.3	0.6
1.000	0.2	0.5

The contour lengths of the polymers, as calculated using average C-C (0.154 nm) and C-O (0.143 nm) bond lengths, are 19, 40, 110, 220 nm for the 43, 93, 250, and 500 repeat unit polymers, respectively. Using the results in Table 4-1 and the calculated contour lengths, as well as computational models which study polyelectrolyte scaling laws as a function of polymer molecular weight[69,73], the 43 repeat unit

polymer is likely too short to be represented by the Rouse model, as the calculated persistence lengths at low concentrations are a substantial fraction of its contour length. I therefore exclude the 43 repeat unit polymer from the following analyses and note that its inclusion would result in poor model fits.

In order to determine whether the nonaqueous polyelectrolyte solutions used here support or refute the expected scaling of the diffusion coefficient with polymer molecular weight, we perform a non-linear fit in Matlab using the following equation:

$$D_{polymer} = yN^z \qquad (4\text{-}10)$$

where y and z are fitting parameters. We are particularly interested in z and whether its value matches that provided in equation 4-7. We perform these fits at all concentrations where the solutions are semidilute and unentangled (0.01-0.25 M Li$^+$) for the polymers with 93-500 repeat units. The data and fits using equation 4-10 are shown in Figure 4-4B, while the resulting values for z with 95% confidence limits are shown in Figure 4-4C. We see that good fits are observed for each polymer molecular weight series, and that the value of z for each fit is statistically equivalent to -1, the expected value from equation 4-7, which confirms the validity of Rouse model scaling theory for these nonaqueous polyelectrolyte solutions.

4.4.2   *Diffusion of the lithium counterion in PAGELS dissolved in DMSO*

No analogous scaling law is available for the counterion self diffusion coefficient in a polyelectrolyte solution. The best approximation for such a model is to combine Stokes Einstein theory with scaling theory to predict solution viscosity. The scaling of viscosity with polymer molecular weight can be derived using similar methodology[58] as that used to derive equation 4-7:

$$\eta = \eta_s N(cb^3)^{0.5}B^{1.5} \propto Nc^{0.5} \qquad (4\text{-}11)$$

Combing equation 4-11 with Stokes Einstein, we obtain:

$$D_+ = \frac{k_B T B^{1.5}}{6\pi r \eta_s (cb^3)^{0.5}N} \propto N^{-1}c^{-0.5} \qquad (4\text{-}12)$$

where *r* is the Stokes radius of the cation (discussed in the previous chapter). Figure 4-5A presents Li$^+$ self diffusion coefficients as a function of PAGELS molecular weight and concentration, with best fits to equation 4-10 also provided. Given the diffusion coefficient/molecular weight dependence predicted in equation 4-12, we expect that the fits shown in Figure 4-5A would result in z=-1. However, z is found to be statistically equal to 0 at all PAGELS concentrations (Figure 4-5B). This is perhaps to be expected given the shortcoming of the Stokes Einstein equation as discussed in the previous chapter. It would perhaps be more appropriate to use the Poisson–Boltzmann–Smoluchowski (PBS) model, but this method requires numerical solutions and does not provide simple scaling laws[46,63,79]. Instead, the experimental data show that empirically, there is no dependence of the lithium counter ion self diffusion coefficient on degree of polymerization in the semidilute unentangled regime, and future studies to elucidate the cause of this behavior is certainly warranted.
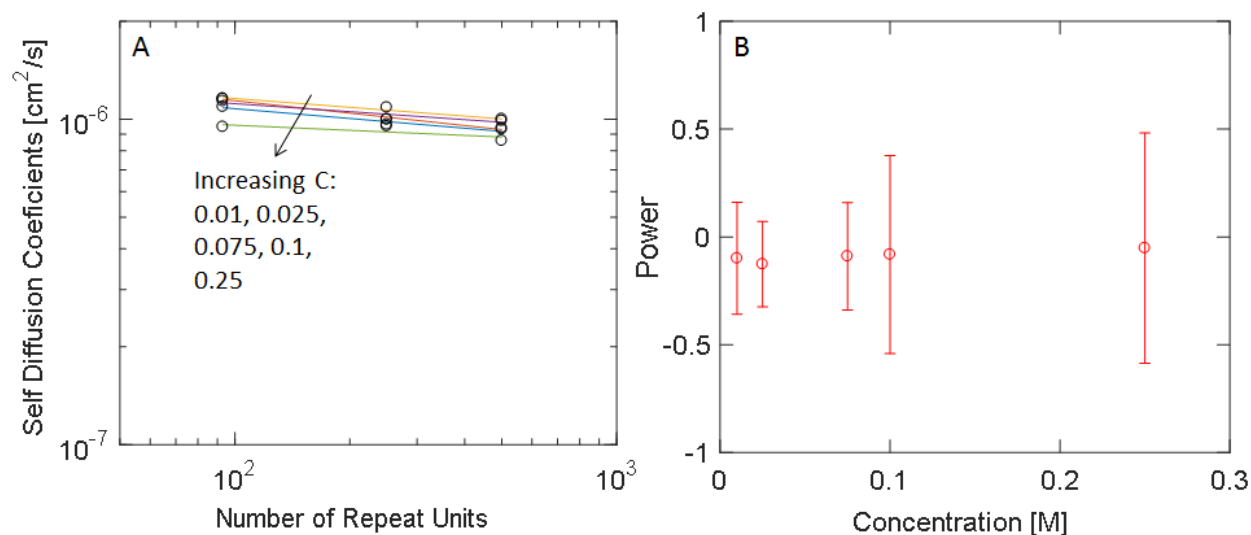
Figure 4-5 Dependence of Li$^+$ self diffusion on the degree of PAGELS polymerization. A) Self diffusion coefficients of Li$^+$ as a function of the number of repeat units at different concentrations. Circles are experimental data while the lines are best fits to equation 4-10. B) Value of z from equation 4-10, or the power of the molecular weight dependence of the self diffusion coefficient. Error bars are 95% confidence limits.

4.4.3   *Overall effect of polyelectrolyte molecular weight on transference number*

Using the scaling arguments made in the previous two sections, it is possible to conclude that the transference number will continue to increase with increasing degree of polymerization, with little to no penalty for the cation self diffusion. This suggests that continuing to move towards higher molecular weight polymers will be beneficial to the transport properties of the resulting electrolytes. Synthetic challenges make it difficult to make higher molecular weight PAGELS, but other systems are expected to follow similar trends. This relationship will hold as long as the solution is in the semidilute unentangled regime. As the molecular weight increases, the crossover concentration to the entangled regime will decrease, and must be taken into account in design of future materials.

4.5   **Effect of solvent choice on transference number**

In the previous chapter, we hypothesized that lithium neutralized polyanions in solution should have high cation transference number, regardless of solvent choice. To test this hypothesis, PAGELS (n=43 and 500) dissolved in three different solvents, dimethyl sulfoxide (DMSO), water, and dimethylformamide (DMF), were studied, with Li$^+$ transference numbers of each solution shown in Table 4-2. As expected given the large size difference between the cation and polyanion regardless of solvent choice, the transference numbers of each solution is very high, particularly for the large molecular weight polymer. It is equally unsurprising that the transference number is slightly different depending on solvent choice, as there are many solvent-specific parameters that influence the relative diffusion of each ion, including solvated ion size (particularly Li$^+$), viscosity, polymer conformation, and electrostatic shielding.

Table 4-2 Cation transference number of PAGELS solutions in three different solvents at 0.1M Li$^+$ and 25°C. Some useful properties of the three solvents.

	DMSO	Water	DMF
t$_+$, n = 43	0.81	0.91	0.70
t$_+$, n = 500	0.95	0.99	0.91
Diffusion coefficient of pure solvent [cm^2/s]^{40,80}	7.3x10^{-6}	2.3x10^{-5}	1.5x10^{-5}
Pure solvent viscosity at 20 °C [cP]	2.00	0.89	0.92
Donor Number	29.80	18.00	26.60
Acceptor Number	19.30	54.80	16.00
Dielectric Constant	46.70	80.10	36.70
Solvent radius [Å]	2.73	1.73	2.81
χ PEO-solvent^a	1.2	5.5	0.7
Debye Screening Length at 0.1M [nm]	0.7	1.0	0.7

^{a} As calculated from regular solution theory[77]

The most important solvent parameters for the transport behavior of PAGELS solutions are listed in the bottom half of Table 4-2: diffusion coefficient of the pure solvent at 25°C (inversely related to the solvent viscosity), donor and acceptor number, dielectric constant, solvent radius, and PEO-solvent interaction parameter. The self diffusion coefficient of the solvent is typically a good descriptor for ionic conductivity because it is an indicator of general mobility in the system. However, the solvent diffusion coefficient is not expected to selectively affect cation mobility compared with the anion, implying that t$_+$ is not expected to be a strong function of the solvent diffusion coefficient.

The donor number, acceptor number, interaction parameter, and dielectric constant all influence the solubility of the polyelectrolyte and the degree of ion dissociation. The donor number describes the solvent's ability to solvate the lithium cation, and to a reasonable first approximation, a solvent with a higher effective donor number than the weak Lewis base sulfonate counterion will dissociate the lithium sulfonate salt. Furthermore, the acceptor number describes a solvent's ability to solvate the sulfonate anion, and therefore sufficiently high acceptor number solvents (such as water) can efficiently dissociate the lithium sulfonate ion pair. Covalent attachment of the sulfonate to the polymer backbone also likely affects the solvating ability of the solvent. Given that the Li$^+$ ion migrates with its solvation shell intact, increasing the solvent molecule radius reduces the Li$^+$ diffusion coefficient, with other conditions staying the same, simply because it increases the effective size of the Li$^+$.

Certain solvent properties can also influence the polyanion shape and size, and understanding these effects is important to explain the polymer self diffusion coefficient. The dielectric constant directly influences the Debye shielding length (e.g., see equations 4-9B), which is a measure of how strongly the charges along the backbone interact, which in turn, has a large effect on polymer conformation. For high dielectric constants (resulting in high Debye screening lengths at a fixed concentration), the polymer is expected to take on a more rod-like conformation due to increased electrostatic repulsion between the

appended anions. Likewise, in low dielectric constant solvents, the polymer will approach a more collapsed, globular conformation because the ions are more effectively screened from one another.

Interactions between the polymer backbone and the solvent also play a role in polymer conformation. To obtain a rough estimate of the PAGELS backbone solubility, I have calculated the interaction parameter between a plain PEO chain and the solvents (χ PEO-solvent) using regular solution theory and have shown these interaction parameters in Table 4-2. It is useful to note that while these calculated interaction parameters are not expected to be exact, they will provide a rough understanding of how well the solvent interacts with the polymer chain. For $\chi=0.5$, the polymer is in a theta solvent, or has equal interactions between the solvent and itself. In this case, the polymer chain conformation takes a random walk. For $\chi<0.5$, the polymer prefers to interact with the solvent rather than itself, and will therefore take on an extended, or swollen, conformation. Finally, for $\chi>0.5$, the polymer prefers to interact with itself instead of the solvent, and will take a collapsed conformation. All three of these solvents have $\chi>0.5$, so the polymer chain would want to collapse onto itself if it were not decorated with ions. Of the three solvents, only water does not solubilize the PAGE parent polymer. It is also interesting to note that water, which has the largest χ (and therefore the least interaction with the polymer backbone), has the highest dielectric constant, and therefore the worst ability to shield electrostatic interactions between ions. In this case, the dielectric constant should drive the polymer towards an extended conformation while the high χ should oppose electrostatics and drive towards a more collapsed state. This is not necessarily true for all solvent choices and backbone chemistries, and it is envisioned that in some cases, solvation and electrostatic interactions can have opposite effects, such that tuning solvent properties could provide leverage to optimize transport properties of polyelectrolyte solutions[74].

Figure 4-6 shows the relationship between self diffusion coefficient of the Li^+ and polymer anions as a function of the self diffusion coefficient of the pure solvent. DMSO has the lowest self diffusion
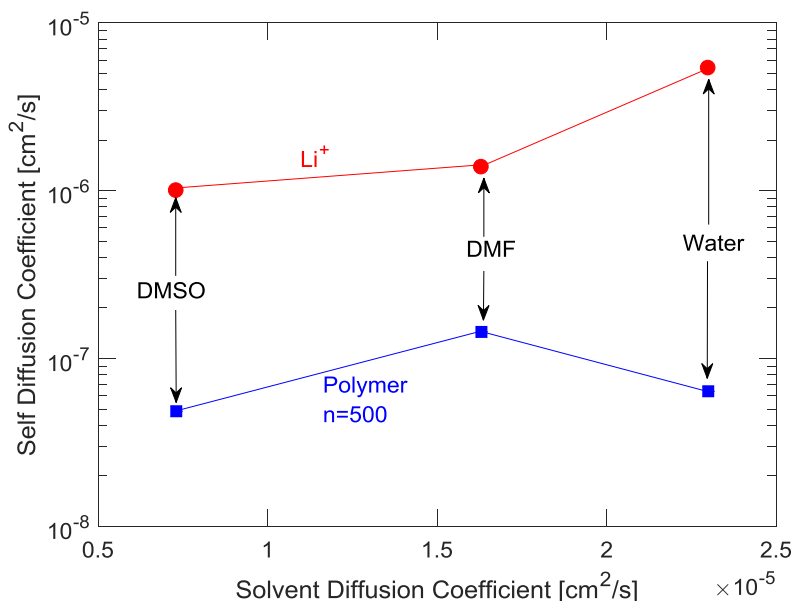
Figure 4-6 Self diffusion coefficient of the lithium (red) and polymer anion (blue) in different solvents (DMSO, DMF, and water). Solutions are at 0.1M Li^+ and 25°C.

coefficient (and highest viscosity) and is expected to therefore have the slowest ion motion. As the solvent diffusion coefficient increases, the self diffusion coefficients of dissolved solutes are also expected to increase. This correlation is generally observed in Figure 4-6, with the exception of the polymer diffusion coefficient in water. This is the first sign that there are conformational changes and specific interactions affecting the PAGELS self diffusion coefficient. To remove the effect of solvent viscosity from the overall diffusion coefficient, we use the relative diffusion coefficient (D_r) [46,63,74], defined as:

$$D_r = \frac{D}{D_0} \qquad (4\text{-}13)$$

where D is the raw self diffusion coefficient of a species in solution and D_0 is the self diffusion coefficient of the pure solvent (third row of Table 4-2).

The relative diffusion coefficients for the PAGELS solutions are shown in Figure 4-7. The relative diffusion coefficient for the lithium (Figure 4-7A) scale inversely with the solvent radius. This is expected, as increasing the solvent radius increases the effective size of the lithium cation, slowing down its relative motion in solution. Both the n=43 and the n=500 PAGELS solution follows the same trend, though the difference in Li$^+$ relative diffusion coefficient is not very large between the two solutions (see previous section). The relative diffusion coefficients of the polymer in solution scale inversely with both dielectric constant and χ, indicating that electrostatic screening is a more important factor than solvent-backbone interactions.
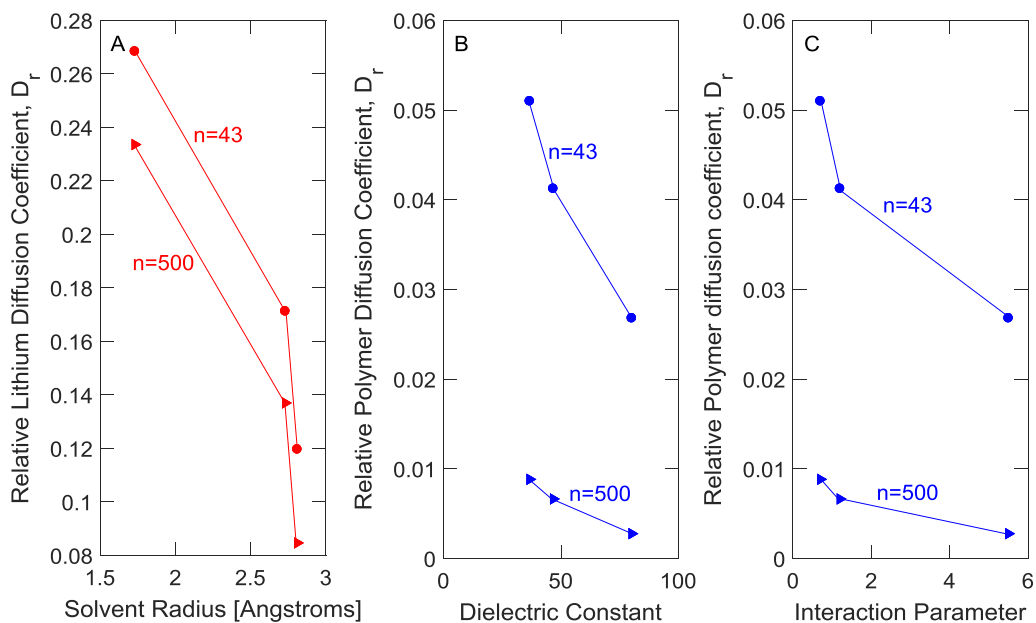
Figure 4-7 Relative diffusion coefficient of charged species in polyelectrolyte solutions in three different solvents. A) Relative lithium diffusion coefficient as a function of the solvent radius. B) Relative polymer diffusion coefficient as a function of the solvent dielectric constant. C) Relative polymer diffusion coefficient as a function of the interaction parameter between the PEO backbone and the solvent. Circles are data for the 43 repeat unit PAGELS solutions while triangles represent 500 repeat unit PAGELS solutions. Solutions are at 0.1M Li$^+$ and 25°C.

Overall, the ideal solvent to optimize conductivity and transference number would have:

- A sufficiently high donor number to dissociate the ions (I note that high donor or acceptor number solvents typically are unstable in Li batteries, such that new ion chemistries that allow lower donor/acceptor number solvents to be used would be ideal)
- A high diffusion coefficient to increase overall conductivity
- A small molecular radius to selectively increase the Li^+ diffusion coefficient
- A small χ with the polymer backbone to swell the polymer backbone and therefore decrease the polymer's diffusion coefficient
- A high dielectric constant to promote an extended polymer conformation due to increased electrostatic interaction between appended ions and thereby decrease the polymer diffusion coefficient.

4.6 Effect of small molecule salt addition to polyelectrolyte solutions on Li^+ transference number

It was observed in the previous section and chapter that the self diffusion coefficient of Li^+ in PAGELS solutions is smaller than that of Li^+ in LiTFSI solutions of equal Li^+ concentration. The analysis of the Stokes radii shows that at high concentrations, where overall solution conductivity is the highest, this difference is due in part to a large increase of the polymer solution viscosity. Although Li^+ diffusion coefficient differences between the two types of solutions are also observed at low concentrations, it is clear that this difference arises from other interactions, likely electrostatic friction, affecting the Li^+ in the polymer solutions rather than just viscous drag, as is only considered when calculating Stokes radii. Previous reports have indicated that the viscosity of polyelectrolyte solutions are substantially lower when even small amounts of binary salts are added to the solution[58,63]. This decrease is a result of increased electrostatic screening (i.e., a decrease in the Debye charge screening length) of the appended anions when a salt is added. Charged polymers in this case will therefore behave more like an uncharged polymer, whose conformation is smaller in solution than a charged polymer with equal contour length. I therefore incorporated LiTFSI into PAGELS solutions in an attempt to reduce solution viscosity at high concentrations, and thereby potentially increase overall solution conductivity. Although I hypothesized that this strategy would improve conductivity, it also would likely reduce the Li^+ transference number due to a reduction in the polyanion conformation size. The objective of this section is to understand transport properties of these solutions and, specifically, the tradeoff between conductivity and Li^+ transference number with varying anion composition.

Table 4-3 Solutions used to study the effect of varying the ratio of LiTFSI and PAGELS (n=500) in DMSO.

Solution #	PAGELS Concentration [M Li^+]	LiTFSI Concentration [M Li^+]	Total Li^+ concentration [M]
1	0.000	1.000	1.000
2	0.025	0.975	1.000
3	0.250	0.750	1.000
4	0.750	0.250	1.000
5	0.975	0.025	1.000

The transport properties of solutions with varying PAGELS and LiTFSI concentrations, whose compositions are provided in Table 4-3, are shown in Figure 4-8. Figure 4-8A presents the self diffusion coefficients of both the Li$^+$ and the polyanion at various LiTFSI/PAGELS ratios, with the Li$^+$ concentration associated with PAGELS plotted on the abscissa. To evaluate the effect of the LiTFSI added to the PAGELS solution, the mixture is compared to the pure PAGELS solutions without added salt, but with similar Li$^+$ concentrations. Surprisingly, when comparing solutions with and without added LiTFSI, negligible differences in Li$^+$ and PAGELS diffusion coefficients are seen even at high LiTFSI contents. n other words, mixtures of PAGELS and LiTFSI result in solutions with diffusion coefficients that resemble pure PAGELS solutions, instead of our desired outcome of a higher Li$^+$ diffusion coefficient that perhaps approached that observed in a pure 1M LiTFSI solution. Using the self diffusion coefficients shown in Figure 4-8A, plus the self diffusion coefficients of the TFSI anion (not shown), the new Li$^+$ transference number is calculated using the following relation:

$$t_+ = \frac{C_{Li^+} D_{Li^+}}{C_{Li^+} D_{Li^+} + C_{TFSI^-} D_{TFSI^-} + C_{polymer^-} D_{polymer^-}} \qquad (4\text{-}14)$$

t$_+$ for PAGELS + LiTFSI mixtures is shown in Figure 4-8B, and for most compositions, resembles t$_+$ observed in a pure LiTFSI solution until very low LiTFSI concentrations. At very small LiTFSI contents (e.g., solution #5 in Table 4-3), a modest decrease in t$_+$ is observed compared to the pure 1M PAGELS solution, yet almost no difference in conductivity is observed between the two solutions, as is shown in Figure 4-8C. Furthermore, the degree of ion dissociation (Figure 4-8C) appears to scales roughly with the relative concentrations of TFSI anions (which only partially dissociate from Li$^+$) and polymer anions (which almost completely dissociate from Li$^+$).

It is incredibly surprising that the diffusion coefficients lack of sensitivity to added LiTFSI (Figure 4-8A), particularly when comparing the solution viscosities of pure PAGELS and PAGELS + LiTFSI mixtures (Figure 4-8D). Even the inclusion of 0.025M LiTFSI dramatically decreases (~5x reduction) the overall solution viscosity, which is in agreement with previous studies[81–83]. In a simple, ideal solution, such a substantial reduction in viscosity would result in an increase in dissolved species diffusion coefficients consistent with that expected from Stokes-Einstein theory (~5x increase). For our solutions, we would certainly have expected at least some conductivity benefit from reducing viscosity, particularly because only minor differences in ion dissociation exist between the two solutions (Figure 4-8C), and a portion of the large polyanion is being replaced by a small, more mobile anion. This leads us to two very important conclusions and numerous remaining questions. The first is that viscosity is obviously not the only important factor in determining either the lithium or the polymer diffusion coefficient. In other words, our results are not well-modeled by Stokes-Einstein theory, as was shown and discussed in the previous chapter. The other important factor was hypothesized to be electrostatic friction on the lithium cations in the previous chapter. Therefore, it is important to evaluate the ability of a small molecule salt to decrease this friction by shielding these electrostatic interactions. Second, LiTFSI does not appear to be more effective at screening this electrostatic friction than the polymer itself. We arrive at this conclusion because despite the decrease in bulk viscosity, the lithium cation appears to still be slowed by this frictional effect. Understanding how these electrostatic interactions appear to counterbalance viscous interactions will help identify whether the addition of small molecule salts is a useful design strategy to increase polyelectrolyte solution conductivity while maintaining a high Li$^+$ transference number.
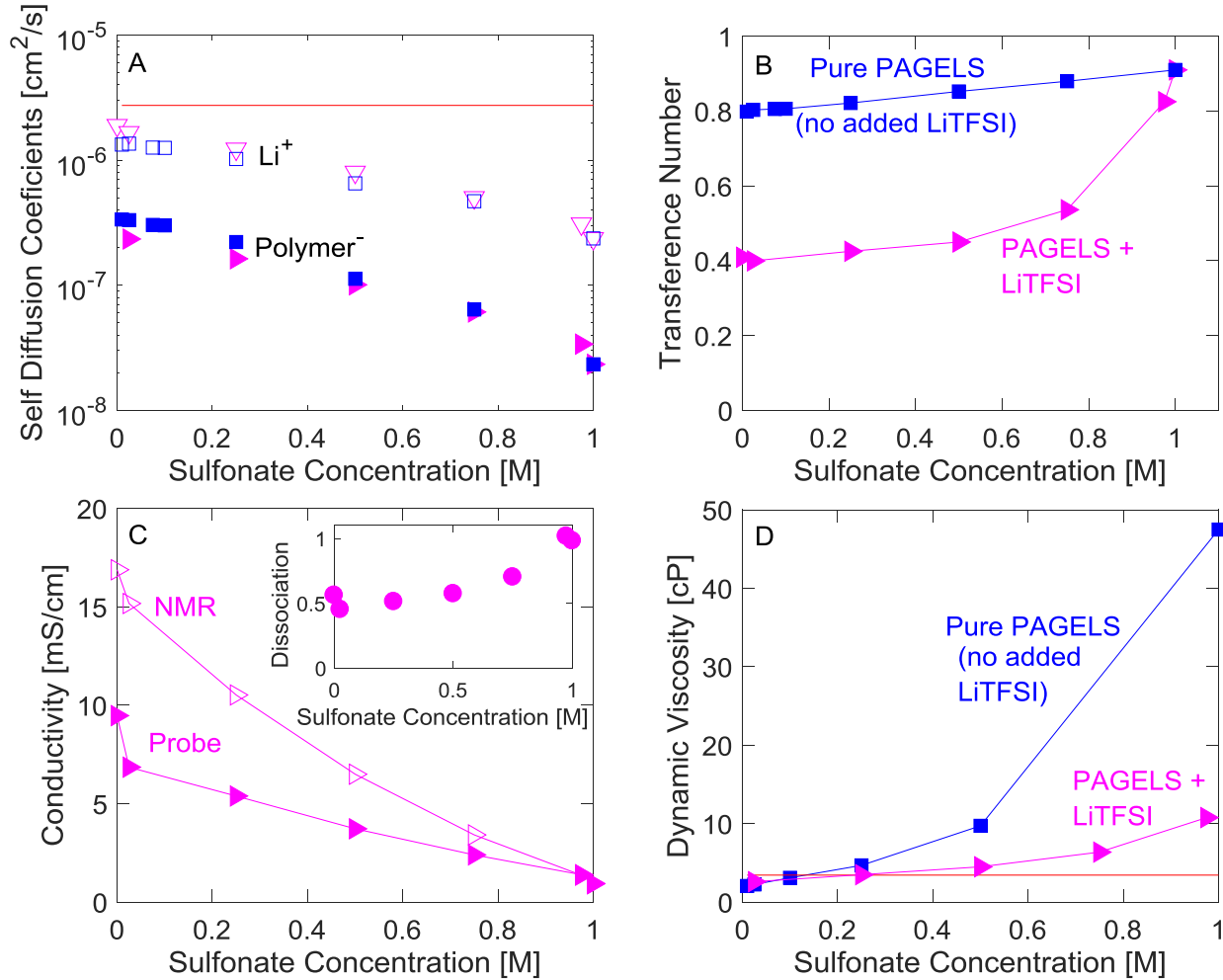
Figure 4-8 Transport properties of PAGELS (n=500) + LiTFSI solutions. The x-axis of all plots is sulfonate anion concentration from PAGELS. All PAGELS + LiTFSI mixtures (pink) are the compositions in Table 4-3, and have a total lithium concentration of 1 M. All solutions are in DMSO at 25°C. A) Self diffusion coefficients of the Li$^+$ (empty shapes), and of the polymer anion (filled shapes) in the pure polymer solutions (blue squares), and the mixtures (pink triangles). The red line is the self diffusion coefficient of Li$^+$ in LiTFSI at 1M. B) Transference number of mixed (pink triangles) and pure polymer (blue squares) solutions. C) Conductivity of the mixtures as measured by conductivity probe (filled) and by NMR (empty). The calculated dissociation is shown in the upper right hand corner. D) Dynamic viscosity of mixed (pink triangles) and pure polymer (blue squares) solutions. The red line is the dynamic viscosity of 1M LiTFSI.

4.7   **Conclusions**

In this chapter, I outlined various possible compositional parameters that influenced transport properties of polyelectrolyte solutions. The Li$^+$ transference number was found to be temperature independent, in agreement with theory for solutions that are fully dissociated at all temperatures measured. A positive

correlation between polymer molecular weight and Li^+ transference number was identified, the effect of which can only be partially described with existing scaling theories. While all three solvents tested here provided high t_+ and high conductivity, it was found that optimization of transport properties through solvent choice is influenced by a variety of different solvent parameters. A donor number large enough to dissociate the ions is critical, whereas ionic motion was also found to be influenced by solvent viscosity, solvent radius (which primarily affects Li^+ motion due to its occupation of Li^+'s solvation shell), and a combination of dielectric constant and polymer-solvent interaction parameter, both of which affect the conformation of the polymer chain. The addition of small molecule salts, such as LiTFSI, as additives to the polyelectrolyte solution, was not identified as a promising approach to improve conductivity while not substantially influencing t_+, but numerous questions remain in understanding why this direction does not appear to be beneficial.

5 Effect of sequence in amphiphilic peptoid coatings on surface structure and marine antifouling/fouling release properties

5.1 Abstract

Amphiphilic polymers, specifically combinations of hydrophilic and hydrophobic residues, have been shown to be effective as antifouling materials against the algae *Ulva linza* and *Navicula* diatoms. In this chapter we use the inherent sequence specificity of polypeptoids made by solid phase synthesis to show that the sequence of hydrophilic (methoxy) and hydrophobic (fluorinated) moieties affects both antifouling and fouling-release of *U. linza*. The platform used to test these sequences was a polystyrene-*b*-poly(ethylene oxide-*co*-allyl glycidyl ether) (PS-*b*-P(EO-*co*-AGE)) scaffold, where the polypeptoids are attached to the scaffold using thiolene click chemistry. The fluorinated moiety is very surface active and directs the surface composition of the polymer thin film. The position and number of fluorinated groups in the polypeptoid is shown to affect both the surface composition and antifouling properties of the film. Specifically, the position of the fluorinated units in the peptoid chain changes the surface chemistry and the antifouling behavior, while the number of fluorinated residues affects the fouling release properties. This work is also published in peer reviewed journals.[84,85]

5.2 Introduction

5.2.1 *Marine antifouling*

Marine biofouling is a complex problem, affecting many man-made structures which operate in water, particularly ships. These foulants adversely affect the performance of the ship, but more importantly, cause the spread of invasive species and harm local aqua-environments. Fouling organisms are classified into three main groups: "micro-settlers" which are microscopic slimes (*e.g.*, diatom *Naviculla*), "soft macro-settlers" which are larger seaweeds and sponges (*e.g.*, algae *Ulva linza*) and "hard macro-settlers" which are shell bearing invertebrates (*e.g.*, barnacles *Balanus Amphitrite*).[86,87] These three example organisms are the most commonly used in tests of marine antibiofouling coatings because of their different settling preferences and behavior.

Historically, antifouling coatings were made using toxic/biocidal materials such as tributyltin oxide.[86] However, legislation has outlawed the use of many of these biocides, and other materials such as copper have come under scrutiny.[88] This has created a need for effective, non-biocidal, marine antibiofouling coatings. The goal is to create a coating that will not kill organisms, but instead be unattractive for settlement.[86] To create such a surface, it is first necessary to understand the fouling process. The classic view of surface colonization involves the initial "conditioning" of a surface by organic materials such as proteins, which later recruit micro-settlers, followed by the settlement of macro-settlers. By this logic surface colonization will be avoided if the initial surface conditioning is avoided, and protein adsorption studies are effective tests for antifouling coatings. However, both seaweed spores[89] and barnacle larvae[90] are capable of settling on a pristine surface, meaning that protein and cell adsorption studies are not sufficient to test the marine antibiofouling performance of a surface.

Marine antibiofouling studies usually involve two main tests. The first is a settlement assay to determine whether the surface is attractive to the organism by finding the settlement density of the organism on the surface. The environmental cues that determine organism settlement include chemical, biological, and

topographical properties. In the case of *Ulva linza*, one of the two organisms used in this study, the spore will spend time "exploring" the surface. Once it finds an attractive surface for settlement, the spore will release vesicles filled with an adhesive onto the surface. The chemical composition of the adhesive itself is not well understood due to the difficulty in obtaining large amounts of the adhesive as well as difficulty in determining which molecules are actually involved in the adhesion process. The adhesive is a combination of a polydisperse 110kDa glycoprotein (the polydispersity is due to different degrees of glycosylation and number of repeated motifs) and smaller (45-80 kDa) proteins.[91] This adhesive is initially liquid and wets the surface differently depending on the hydrophobicity of the surface.[92] The adhesive then undergoes a curing process which involves the crosslinking of the glycoprotein by dithiol linkages. The second test is a fouling release assay which measures how easily an organism is removed from a surface under shearing forces. As a ship moves through water its hull is exposed to shearing forces, which may remove organisms which are not strongly attached. These properties are often related to the modulus of the material, though the chemistry will also have an effect. In the case of *Ulva linza,* after initial settlement the spore germinates and continues to produce the adhesive, which integrates with the cell wall, keeping the growing plant attached to the surface.[91]

5.2.2   *Why Polypeptoids*

In nature the sequence specificity of polypeptides and other biological polymers mediates the complex interactions between organisms and their environment. Small variations in sequence, size, and composition can have large effects on structure, as well as the peptide's interaction with living organisms. Peptoids are a class of non-natural biomimetic oligomers based on an N-substituted glycine backbone[93] that combine many of the advantageous properties of bulk polymers with those of synthetically produced polypeptides. Because the functional group in polypeptoids is introduced via a primary amine, there are a large number of cheap and readily available starting materials, and an enormous number of available functionalities. Additionally, peptoids can be synthesized in high yields and large, scalable batches by synthesis on rapid, automated synthesizers. Furthermore, they have the ability to incorporate biologically relevant functionalities as well as synthetic functionalities, and have high biological stability. Because there is no hydrogen bond donor in the peptoid backbone (in contrast to peptides, which contain secondary amines in the backbone) polypeptoids exhibit enhanced thermal and solution processability over other biological materials.[94] However, attaching peptoids to a surface in an industrially relevant way is challenging. For the purposes of this study, the peptoids are attached to the surface using a poly(styrene)-b-poly(ethylene oxide) scaffold polymer. This scaffold allows for the incorporation of the peptoid into a thin film, while adding mechanical stability to the film, as well as increasing compatibility with underlying coatings such as rubbery coatings or anticorrosive coatings.

These advantageous properties make polypeptoids ideal candidates for creating tunable materials for large scale applications such as coatings. The sequence specificity of polypeptoids enables their physical properties and therefore their processability to be tunable with monomer sequence. We can thus access a range of thin film processing conditions. At the same time, because many known antifouling functionalities can be incorporated using a single backbone chemistry, making a direct comparison of the effects of these functionalities and their sequence possible. Previous antifouling studies have shown that topographical patterns[95], low modulus surfaces[96], hydrophilic surfaces[97], amphiphilic surfaces[98,99] , and zwitterionic surfaces[100] all have favorable antifouling and fouling release properties. Our approach of

using polypeptoids to understand the effect of sequence on antifouling leads us to a particular interest in amphiphilic surfaces and sequences of the hydrophobic and hydrophilic groups.

5.3   Experimental

5.3.1   *Synthesis*

The synthesis of the polymers used in this study was performed using three main steps. First, the parent poly(styrene)-block-poly(ethylene oxide-co-allyl glycidyl ether) (PS-b-P(EO-co-AGE)) polymer was synthesized using anionic polymerization, Figure 5-1. Then, the thiol-terminated polypeptoids were synthesized using solid phase synthesis and purified using standard methods, Figure 5-2. Finally, the peptoids were attached to allyl groups pendent to the parent polymer using thiol-ene click chemistry Figure 5-3.

5.3.1.1   *PS-P(EO-co-AGE) synthesis*

PS-b-P(EO-co-AGE) with Mn(PS) = 22300, and Mn(P(EO-co-AGE)) = 46000 with 2.9 mol% AGE and a polydispersity (PDI) of 1.11 was synthesized as described previously.[99] In short, alcohol-terminated polystyrene (PS) was grown anionically in cyclohexane with a sec-butyl lithium initiator and termination with ethylene oxide followed by isopropyl alcohol. The resulting polymer was precipitated into 50:50 methanol/isopropanol, filtered, dried under vacuum, and characterized by refractive index size-exclusion chromatrography (RI-SEC) and 1H NMR spectroscopy. The hydroxyl terminated PS was then used as a macroinitiator for the anionic co-polymerization of ethylene oxide and allyl glycidyl ether in tetrahydrofuran (THF).
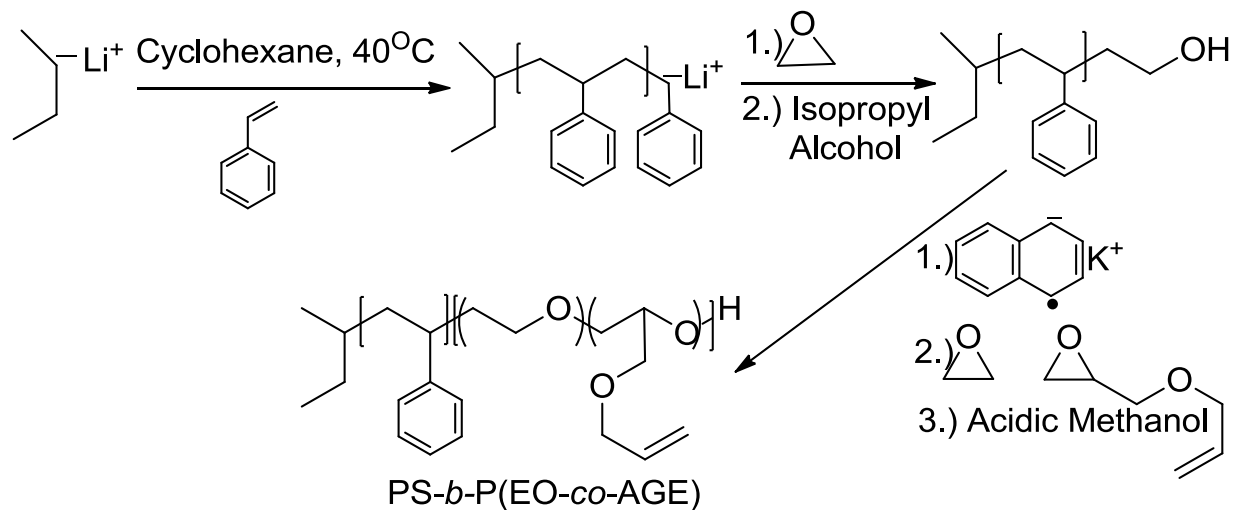
Figure 5-1 Reaction scheme for synthesis of the parent PS-b-P(EO-co-AGE) polymer.

5.3.1.2   *Peptoid Synthesis*

Polypeptoids were synthesized on a robotic synthesizer on 100 mg of Rink amide polystyrene resin (0.6 mmol/g, Novabiochem, San Diego, CA) using a previously described submonomer method.[101,102] All primary amine monomers, solvents, and reagents were purchased from commercial sources and used without further purification. Amine displacement times were typically 1 hour for methoxyethylamine (1.5

M in N-methyl pyrrolidone (NMP)) and 2 hours for heptafluorobutylamine (1.25 M in dimethyl formamide (DMF)) and amines coupled directly after that. Only when heptafluorobutylamine was to be coupled directly to the resin (or to one or two heptafluorobutyl groups already coupled to the resin) was the reaction performed at 50 °C for 3 hours. All peptoids were thiol functionalized by reacting for 1 hr in 1 mL of 0.5 M S-tritylmercaptopropionic acid and 75 µL of N,N'-Diisopropylcarbodiimide (DIC). Peptoid chains were cleaved from the resin by addition of 3.0 mL of cleavage cocktail (47.5 v% trifluoroacetic acid (TFA), 47.5 v% dichloromethane (DCM), 2.5 v% H2O, 2.5 v% triisopropylsilane (TIS)) for 10 minutes, which was then evaporated off using a Biotage V-10 evaporator. This simultaneously resulted in deprotection of the thiol functionality (significantly longer cleavage times would result in a cyclization reaction cleaving off the thiol and final monomer). Following cleavage, peptoids were dissolved in appropriate acetonitrile/water mixtures and lyophilized twice to obtain a fluffy white powder. All peptoids were purified by reverse-phase prep high performance liquid chromatography (HPLC), and their purity and mass were determined by analytical reverse-phase HPLC and matrix assisted laser desorption ionization (MALDI) as previously described[102]. Properties and sequences synthesized for this work are shown in Table 5-1.

Table 5-1 Thiol functionalized peptoids used in this study are shown below with their names and purity. The thiol functionality is represented by a dash in the sequence column, the N-(2-methoxyethyl)glycine unit is represented by green (dark), and the N-(heptafluorobutyl)glycine unit is represented by yellow (light). The code is used to identify the peptoid sequence. Once the peptoid has been clicked onto the PS-b-P(EO-co-AGE) scaffold described below, it is called AGE-(peptoid code).

Name	Code	Sequence	Mass	Observed mass $(+Na)^a$	Purity $(\%)^b$
5merA1	5		804.3	829.3	91
10merA2	10		1503.6	1529.0	92
15merA3	S3		2202.8	2228.1	90
15merB3	S2		2202.8	2227.5	86
15merC3	S1		2202.8	2227.4	81
15merC2	15-2		2078.9	2103.2	83
15merC1	15-1		1954.9	1979.8	80
12merD	12		1485.8	1510.9	81

[a] as observed on MALDI. The ionized peptoid usually flies with a sodium counterion, meaning that the observed mass is 23 g/mol larger than the calculated mass. This is not related to the state of charge in solution.

[b] as observed by analytical reverse-phase HPLC
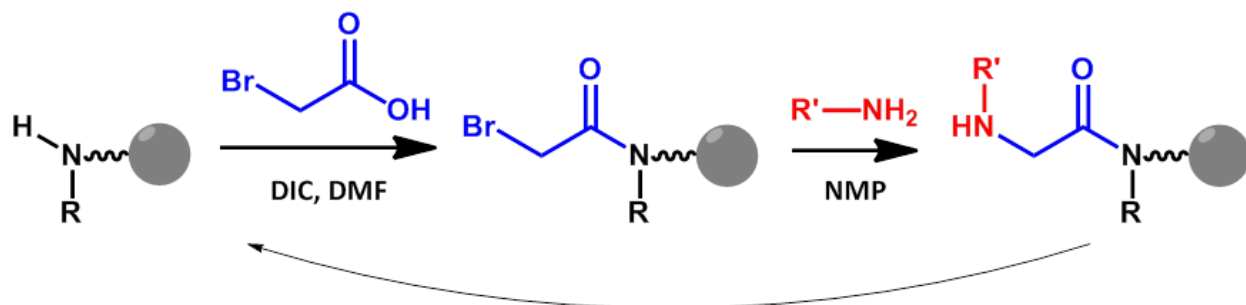
Figure 5-2 Solid phase synthesis of polypeptoids in two steps. First, the bromoacetylation occurs, then a displacement using a primary amine, recreating the secondary amine, which can then be bromoacetylated again. This synthesis allows for the sequence-specific synthesis of peptoids up to 50 monomers long where one monomer is formed by the two step reaction of bromoacetylation and displacement.

5.3.1.3 *Comb-copolymer Synthesis*

Thiol-ene coupling of the thiol functionalized peptoid sequences, as shown in Figure 5-3, was performed by dissolving 100 mg of polymer in a small amount of DMF (typically 550 µL per 100 mg of polymer) in a 1 dram vial. Then 2.5 equiv of thiol functionalized peptoid (with respect to alkene groups in the polymer) were added and dissolved. Finally 0.4 equiv of 2,2-dimethoxy-2-phenylacetophenone (DMPA) photoinitiator and a small stir bar were added. The vial was sealed with a screw cap fitted with a polytetrafluoroethylene (PTFE) septum, and the mixture was purged with argon for 10 min. Irradiation was carried out for 30 min with a 365 nm UV lamp. The reaction was driven to completion by extra addition of 0.5 equiv of peptoid, 0.2 equiv of DMPA, and DMF (50 µL per 100 mg). The new mixture was purged for 10 minutes with argon before reacting 30 extra minutes under UV irradiation. After the reaction, 2.5 ml of acetonitrile was added to the reaction vessel and the mixture was suspended in 12.5 ml of Milli-Q water. These mixtures were concentrated using Amicon Ultra centrifugal filter units (30 000 cutoff Mw, Millipore) and resuspended in 15 ml of 1:6 acetonitrile/water. This procedure was repeated twice. All concentrated block copolymer solutions were lyophilized from 1:6 acetonitrile/water mixtures. The reaction was monitored by ^{1}H NMR, shown in Figure 5-4.
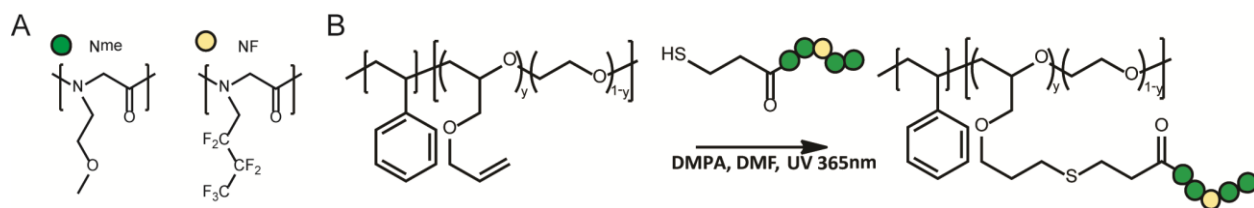
Figure 5-3 a.) Peptoid monomers used in this study, N-(2-methoxyethyl)glycine (Nme) and N-(heptafluorobutyl)glycine (NF), symbol, and abbreviation used to present them. b.) Thiol-ene click chemistry is used to functionalize PS-P(EO-co-AGE) with thiol terminated peptoids to make a comb shaped polymer. Specific functionalized polymers within this class are called AGE-(Peptoid code), where the peptoid code is provided in Table 5-1.

5.3.1.4 *Polymer characterization*

Nuclear magnetic resonance (^{1}H NMR) spectra, such as those in Figure 5-4, were recorded on a Bruker Biospin Avance II 500 MHz High Performance NMR Spectrometer at room temperature. Chemical shifts are reported in parts per million relative to CHCl$_3$ at 7.26 ppm for ^{1}H as an internal reference. Gel permeation chromatography (GPC) was performed on an Agilent GPC system, equipped with PLgel 5µm MIXED"D columns and calibrated with narrow polystyrene standards. Using a flow rate of 1 mL/min, the mobile phase was DMF at 40°.
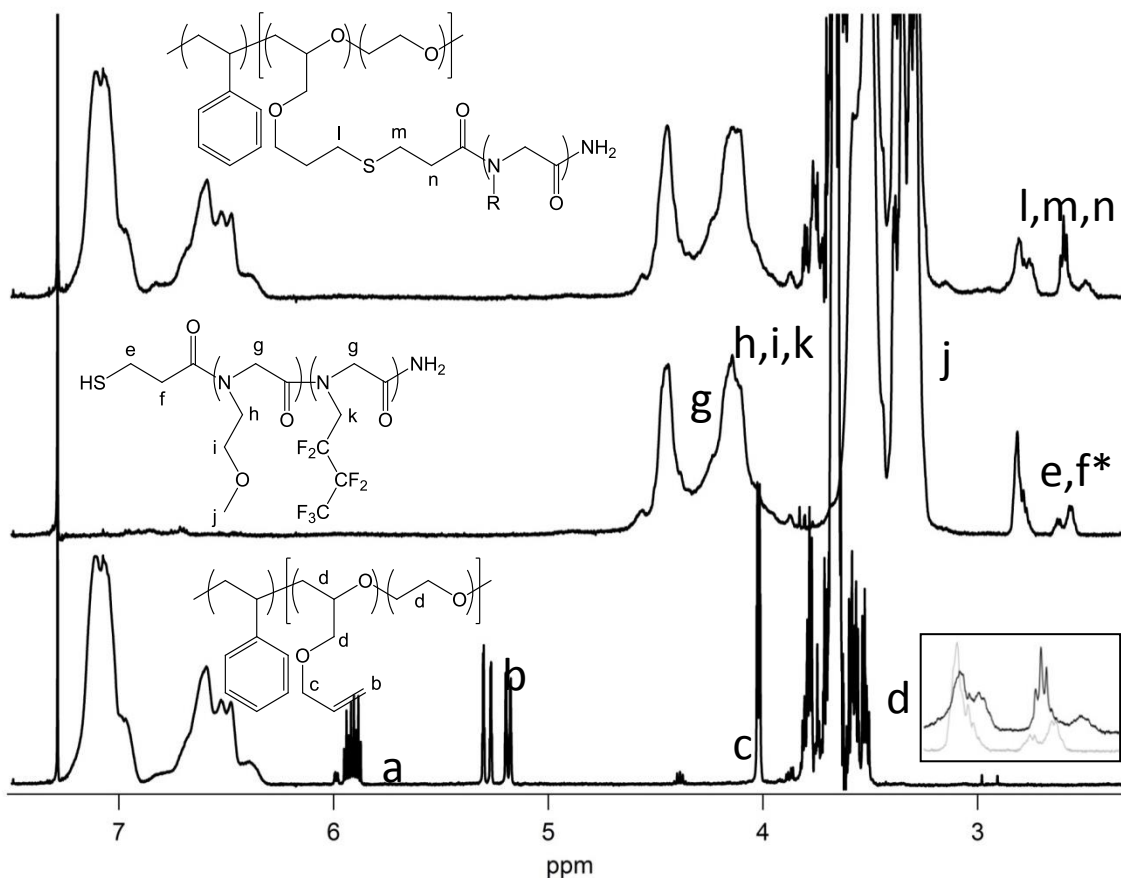
Figure 5-4 1H NMR spectra of the starting PS-b-P(EO-co-AGE) polymer (bottom), thiol terminated peptoid (middle), and the product after thiol-ene coupling (top). The inset shows an overlay of the 3-2.5 ppm region for the peptoid product. *Four peaks are visible due to the diastereotopic protons next to the amide bond and a minor amount of dithiol impurity.

5.3.2 *Thin film preparation and characterization*

Films with a thickness of approximately 80 nm were spin coated at 1500 rpm from 1.5% (w/v) block copolymer solutions in toluene onto plasma-cleaned silicon wafers. All films were vacuum annealed for at least 16 hours at 120 °C.

5.3.2.1 *Near Edge X-ray Absorption Fine Structure (NEXAFS)*

Near Edge X-ray Absorption Fine Structure (NEXAFS) experiments were conducted on the U7A NIST/Dow materials characterization end-station at the National Synchrotron Light Source at Brookhaven National Laboratory (BNL). The general NEXAFS principles and a description of the beam line at BNL have been previously reported[99,103–105]. In short, the X-ray beam hits the sample with an angle θ to the sample surface and ejected electrons are collected at an angle ϕ from surface normal as shown in Figure 5-5. Because the angle between the X-ray and detector is fixed at 36°, both the surface sensitivity and the sensitivity to bond orientation can be controlled by varying θ. At a θ of 120°, ϕ is 66° and the technique is more surface sensitive. At "magic angle" of θ equal to 54.7° the technique reports chemistry irrespective of ordering or bond orientation, and provides information about the top 2nm of the film. Unless otherwise specified, all spectra were taken at the magic angle.
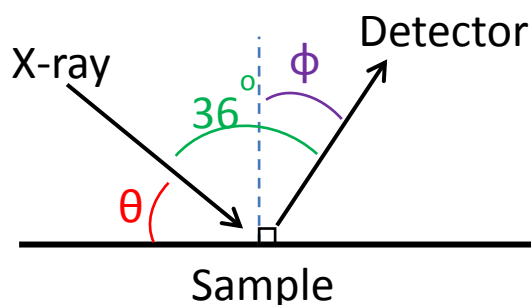
Figure 5-5 Geometry of NEXAFS set up at U7A endstation at NSLS.

The PEY C1s spectra were normalized by subtracting a linear pre-edge baseline from 270 – 280 eV and setting the edge jump to unity at 320 eV.[106] The photon energy was calibrated by adjusting the peak position of the lowest π* phenyl resonance from polystyrene to 285.5 eV[107]. No further normalization was conducted for the N1s spectra.

5.3.2.2 *Sum Frequency Generation (SFG)*

The polymers were coated on silica windows (1 inch in diameter, 1/8 inch thick, from ESCO Optics) via spin-coating and annealing, with a thickness of approximately 80 nm. The SFG spectroscopy was implemented according to the protocol reported previously[108]. Briefly, the visible and infrared (IR) input beams penetrated a SiO_2 window and overlapped spatially and temporally at the polymer surface/interface (Figure 5-6). The incident angles of the visible and IR beams were 60° and 54° with respect to the surface normal, and the pulse energies of the visible and IR beams were 50 and 100 μJ, respectively. The reflected SFG signal was collected by a monochromator along with a photomultiplier tube. All SFG spectra were collected using the ssp (SFG output, visible input, and IR input) polarization combination.
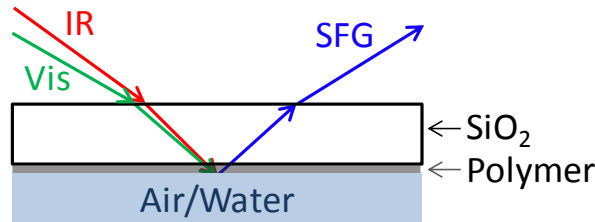
Figure 5-6 Schematic of setup used in SFG experiments. The polymer coating is on a silica window in air or water.

5.3.3   Ulva Assays

Both antifouling and fouling-release assays were performed as previously described[99,109]. Coatings were equilibrated in 0.22µm filtered artificial seawater (Tropic Marin®) for 24 hours before testing. Zoospores were obtained from mature plants of *U. linza*, collected at Llantwit Major in South Wales. Spores were released by the standard method. A suspension of zoospores (10 ml; 1×10^6 spores ml^{-1}) was added to individual compartments of quadriperm dishes, in the dark. After 45 minutes in darkness at c. 20 ^{o}C, the slides were washed by passing 10 times through a beaker of seawater to remove unsettled spores.

5.3.3.1   Settlement of zoospores

Slides were fixed using 2.5 % glutaraldehyde in seawater. The density of zoospores attached to the surface was counted on each of 3 replicate slides using an image analysis system attached to a fluorescence microscope. Spores were visualized by autofluorescence of chlorophyll. Counts were made for 30 fields of view (each 0.15 mm^2) on each slide.

5.3.3.2   Growth and Removal of Sporelings

Spores were allowed to settle on the coatings for 45 minutes and then washed as described above. The spores were cultured using supplemented seawater medium for 7 days to produce sporelings (young plants) on 6 replicate slides of each treatment. Sporeling growth medium was refreshed every 48 hours.

Sporeling biomass was determined *in situ* by measuring the fluorescence of the chlorophyll contained within the sporelings in a Tecan fluorescence plate reader. Using this method the biomass was quantified in terms of relative fluorescence units (RFU). The RFU value for each slide is the mean of 70 point fluorescence readings taken from the central portion. The sporeling growth data are expressed as the mean RFU of 6 replicate slides.

Strength of attachment of sporelings was initially assessed using a shear stress of 52 Pa in a water channel (52 Pa is the maximum achievable in our initial experimental setup)[110]. There was negligible removal from any of the peptoid test surfaces and consequently the apparatus was changed for a higher-powered water jet.

The relative attachment strength of sporelings on the peptoid comb copolymer coatings was determined by exposure to a water jet producing an impact pressure of 160 kPa (Figure 5-7). The sequences of these peptoids are shown in Table 5-1. Biomass remaining after exposure to the water jet was determined using

the fluorescence plate reader (as above). The percentage removal was calculated from readings taken before and after exposure to the shear stress.
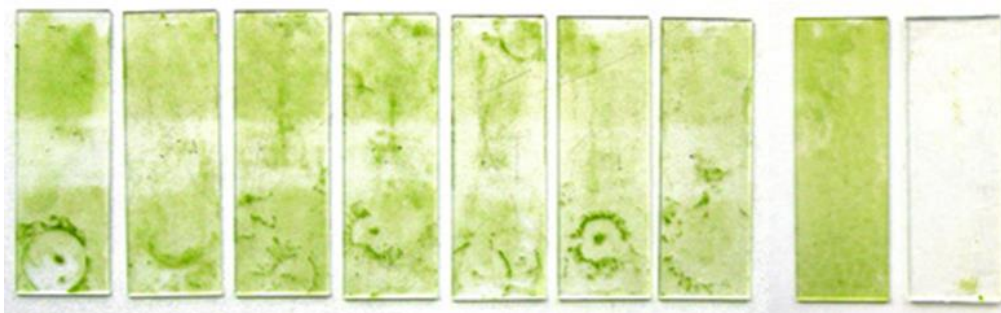
Figure 5-7 Image showing sporelings remaining on amphiphilic peptoid coatings after exposure to a shear stress of 160 kPa. From left: AGE-15-1, AGE-15-2, AGE-S1, AGE-S2, AGE-S3, AGE-10, AGE-5, glass, PDMS.

5.4 **Results and Discussion**

5.4.1 *NEXAFS to probe surface chemistry of dry polymer thin films*

A previous study of PS-b-peptoid model block copolymer systems indicated that fluorinated peptoid monomers drive surface segregation of a predominantly hydrophilic peptoid block[102]. The carbon edge near edge X-ray absorption fine structure (NEXAFS) spectrum shown in Figure 5-8 shows that the same is true for the PS-b-P(EO-co-AGE) copolymer system used here (23kPS, 46kPEO, 3 mol% AGE). In Figure 5-8 it is apparent that in the case of the fluorine deficient peptoid, AGE-12merD shown in Table 5-1, PS segregates at the top 2 nm[105] of the surface as characterized in Figure 5-8 by the sharp C 1s → $\pi^*_{C=C}$ transition at 285.5eV and no evidence of the C 1s → $\pi^*_{C=O}$ or the C 1s → $\pi^*_{C=O}$ transition (at 288.6 and 289.5 eV) that are characteristic of polypeptoids and PEO respectively. In this case, the PS has a lower surface free energy than the peptoid or the PEO and therefore forms a wetting layer at the surface of the film. However, fluorocarbon bonds have an even lower surface free energy and will segregate to the surface on top of the PS. When a fluorocarbon group is attached to the polypeptoid and PEO domains of the polymer, it provides a sufficient driving force to drag the polypeptoid and the PEO to the surface as well, effectively pushing the PS deeper into the film. This can be seen in the case of the fluorinated peptoid AGE-15merB3 in Figure 5-8 where no C 1s → $\pi^*_{C=C}$ transition is observed. Instead, typical PEO and peptoid π and σ transitions can be observed as well as the σ^*_{C-F} transition at 293 eV. Moreover, Figure 5-8 shows that closer to the surface (θ=120° is more surface sensitive than θ=55° as seen in Figure 5-5) the π^*_{C-N}, σ^*_{C-N}, and σ^*_{C-F} transitions are more pronounced, indicating that peptoid chains are concentrated at the surface since the fluorocarbon is attached directly to the peptoid.
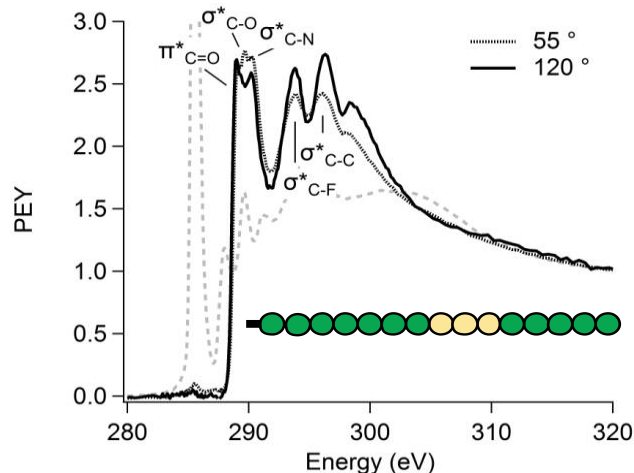
Figure 5-8 Carbon K-edge NEXAFS spectra of AGE-15merB3 (sequence on image) at two different θ. The dashed line is the spectrum of the hydrophilic AGE-12merD surface. It is identical to the spectrum obtained for a pure polystyrene surface and for the parent AGE copolymer because when there is no fluorine to direct the surface presentation, PS surface segregates.

A systematic study of the surface segregation behavior of the complete fluorinated peptoid series listed in Table 5-1 gives further insight into our control of surface composition with the modular PS-b-P(EO-co-AGE/peptoid) copolymers. The NEXAFS spectra for this series are shown in Figure 5-9. There is a strong dependence of surface chemistry on the position of the fluorinated moiety in the peptoid, despite identical overall chemical composition of the peptoid and therefore the overall polymer. The fluorinated groups were placed at the beginning of the peptoid (closest to the PEO backbone), in the middle of the peptoid, or at the end of the peptoid (farthest from the PEO backbone). All of these peptoids were fifteen repeat units long, containing three N-(heptafluorobutyl)glycine residues and twelve N-(2-methoxyethyl)glycine residues. They are compositionally identical with a molar mass of 2228 Da as observed by matrix-assisted laser desorption ionization (MALDI). The carbon edge NEXAFS spectra shown in Figure 5-9a shows that the σ^*_{C-F} peak from the peptoid and the $\pi^*_{C=C}$ peak from the PS are similar for all three sequences. For all three the surface is covered by the surface segregating fluorocarbon as indicated by a large σ^*_{C-F} peak, and PS is effectively covered by PEO and peptoid as indicated by the very small $\pi^*_{C=C}$ peak. However, there is a clear difference between the different sequences in the amount of PEO as compared to peptoid as seen in the σ^*_{C-N} and σ^*_{C-O} peaks. Because these peaks are close together and the peptoid is the only source of nitrogen in the system, it is informative to use the nitrogen edge NEXAFS spectrum shown in Figure 5-9b as an indicator of peptoid content at the surface. As the fluorinated units were moved from the outer edge of the peptoid towards the PEO backbone, the amount of peptoid at the surfaces decreased as seen in Figure 5-9b, and the amount of PEO increased because when the fluorine is at the end of the peptoid it dragged only peptoid towards the surfaces, covering the surface with fluorinated peptoid chain ends. However, when the fluorine is close to the PEO backbone, both the PEO and the peptoid are dragged to the surface and the surface is covered with fluorinated peptoid loops.

As one might expect, the length of the peptoids also has an effect on the thin film surface composition. In this case, peptoids were five, ten, and fifteen repeat units long and contained one, two, and three fluorinated residues, respectively. The nitrogen 1s NEXAFS spectra in Figure 5-9d show that there is less

peptoid at the surface of the films with shorter peptoids due to a lower volume fraction of peptoid in the film. From the carbon edge we see that there is a small increase in σ^*_{C-F} peak height with increasing fluorinated residue content. However, there is an increase in the size of the $\pi^*_{C=C}$ peak, indicating an increase in PS content with decreasing peptoid size. This indicates that the five unit and ten unit long peptoids are not able to completely cover the PS, and that to achieve a PS free surface, a higher peptoid volume fraction or larger groups are needed.

Finally Figure 5-9 shows that the fraction of fluorinated groups can be used to control the surface segregation. Decreasing the number of heptafluorobutyl groups does not change the amount of peptoid at the surface as seen in the nitrogen edge NEXAFS spectra, indicating that one group is sufficient to drag all geometrically accessible peptoid to the surface. As expected, we observe an increased σ^*_{C-F} signal for higher fluorine content polymers, but we also see a corresponding decrease in PS because the heptafluororbutyl groups are larger than the methoxyethyl groups and are more effective at covering the underlying PS.

5.4.2   *SFG to probe surface chemistry of hydrated thin films*

In collaboration with Zhan Chen's group at the University of Michigan, the same polymers as shown above were analyzed using sum frequency generation (SFG) spectroscopy. Unlike NEXAFS, which is done in ultra-high vacuum, SFG is able to probe the surface chemistry of polymer thin films under aqueous conditions relevant for marine antifouling applications. SFG works by only observing the stretches of molecules with particular symmetries. Because molecules at interfaces and in the bulk have different symmetries, it is possible to separate about the signals of these two populations[111]. It is sensitive to less than a monolayer of molecules[112]. In the case of the dry samples presented below, the first several layers of atoms are observed. In the case of the hydrated films, the signal is dominated by the monolayer of water closest to the polymer surface.

Figure 5-10A shows the SFG spectra of the polymer coatings in air. A distinct peak at 2815 cm^{-1} assigned to the O-CH$_3$ group on N-(2-methoxyethyl)glycine (Nme) was observed for all the Nme-containing polypeptoids, indicating that the O-CH$_3$ end group is present at the polymer surfaces in air. As expected, the spectrum of PFOT (a control sample containing no peptoid, only the parent PS-b-P(EO-co-AGE) polymer functionalized with perfluorooctanethiol) does not show any peak at 2815 cm^{-1}, verifying that the 2815 cm^{-1} signal for the other polymers is due to the presence of methoxyethyl groups on the peptoids.

Figure 5-10B shows the intensity of the peak at 2815 cm^{-1} detected from the polymer surfaces in air. We observe that the intensity is a function of polypeptoid sequence. The strongest intensity was detected for 15merC1, in which one N-(heptafluorobutyl)glycine (NF) residue is attached to the outer edge of the peptoid (farthest from the polymer backbone). The single NF residue segregates to the surface in air, bringing the rest of the peptoid and the methoxyethyl residues to the surface as well. As the number of the NF units at the outer edge of the peptoid increases from one to three (15merC1, 15merC2, and 15merC3), the SFG signal of Nme decreases because while peptoid is present at the surface, the heptafluorobutyl residues replace methoxyethyl residues at the surface. For 15merC3, 15merB3, and 15merA3, in which the number of the NF units stays constant at three in the peptoid chain, the O-CH$_3$ signal increases when the NF units are moved from the outer edge to the middle of the peptoid close to the polymer backbone. Unlike those at the end of the peptoid, the three NF units in the middle of peptoid can drag the Nme units at both sides to the surface, thereby increasing the surface coverage of Nme. For all the polymers, no

signal of the phenyl ring above 3000 cm^{-1} was detected, indicating the absence of polystyrene at the surfaces in the AGE-peptoid polymers containing NF. This is consistent with the NEXAFS results shown in 0.

Figure 5-10C shows a negative correlation between the SFG signal at 2815 cm^{-1} in air assigned to the Nme residue (Figure 5-10) and the NEXAFS signal at 293.8 eV assigned to the NF unit (Figure 5-9). The negative relationship demonstrates the inversely related surface coverage between the Nme and NF units due to their different surface energies, and also demonstrates the consistency between the results from SFG and NEXAFS measurements
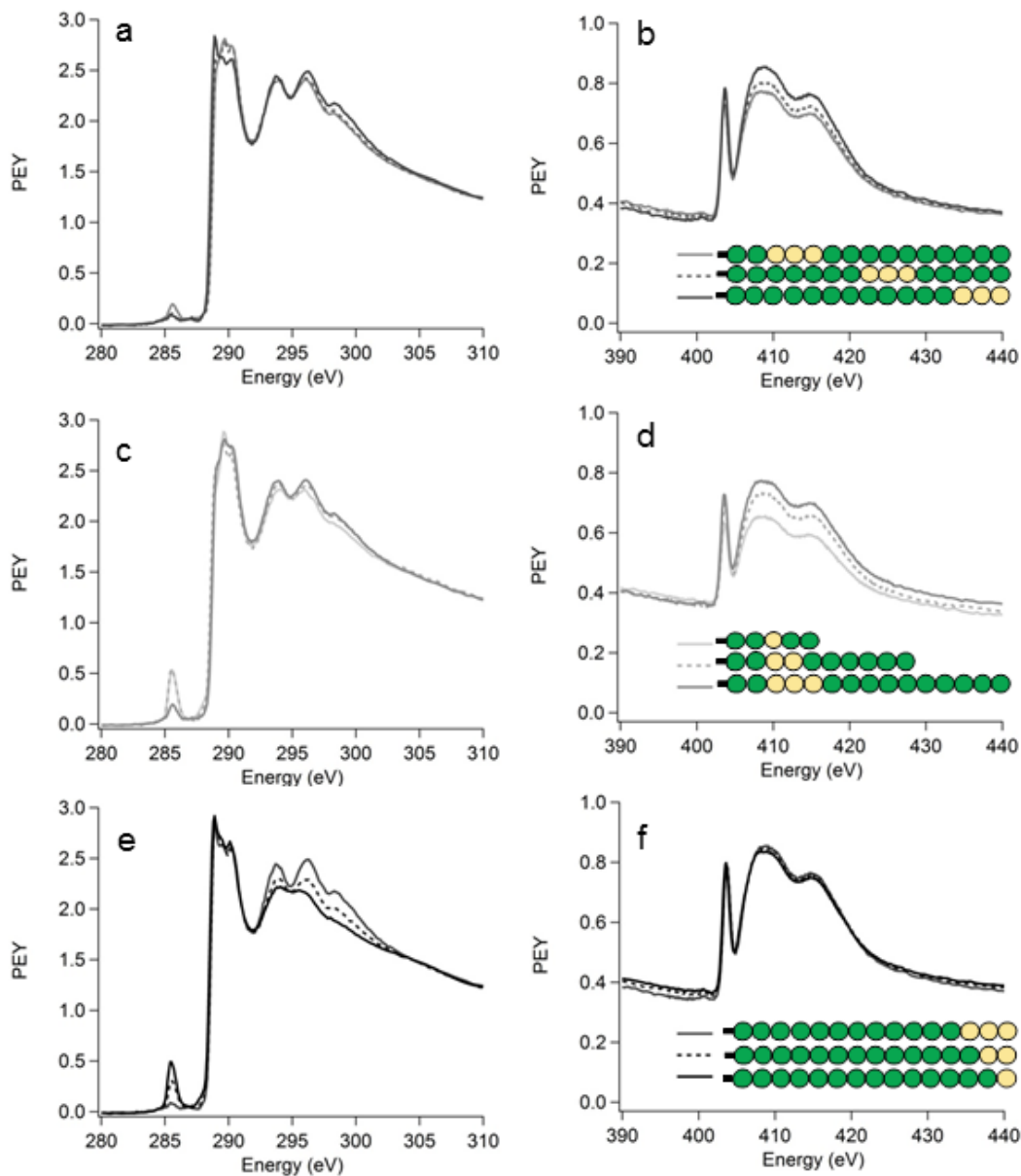
Figure 5-9 The carbon edge (left) and nitrogen edge (right) NEXAFS spectra of PS-b-P(EO-co-AGE/peptoid) copolymers show the surface chemistry of the films.
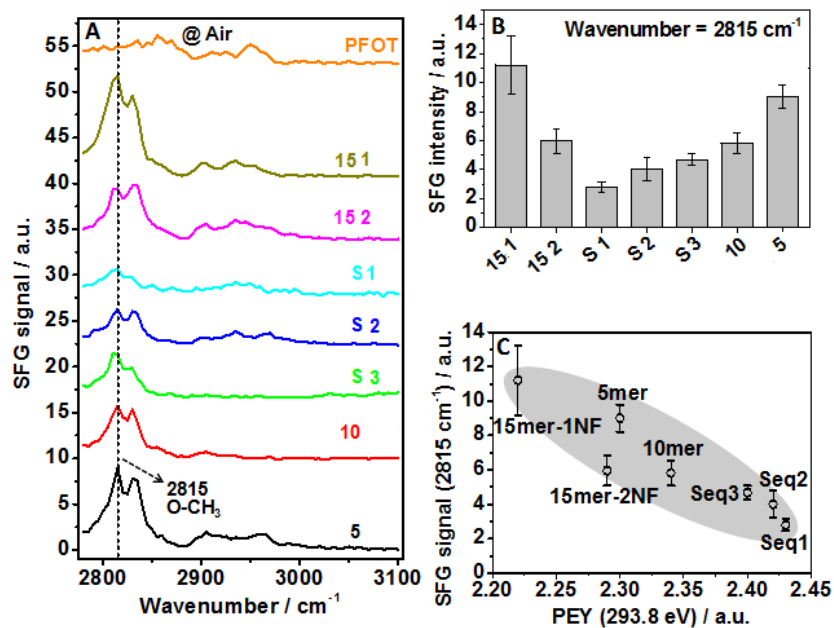
Figure 5-10 SFG spectra of polymer thin films and comparison with NEXAFS results. A) SFG spectra of the polymers in air allows us to probe the methoxy units in the polymer film. B) Peak intensity at 2815 cm^{-1} (assigned to methoxy residues) from the spectra of the polypeptoids in A. C) The SFG intensity at 2815 cm^{-1} assigned to O-CH$_3$ of Nme is negatively correlated to the partial electron yield (PEY) at 293.8 eV from NEXAFS assigned to the fluorine element on NF. These SFG results agree with the NEXAFS results.

While the SFG experiments on dry films agree with the NEXAFS experiments of dry films, the additional value of SFG is as a tool to probe the hydrated films. These results are shown in Figure 5-11. We observe that all of the polymers films in water show little C-H stretching signal, indicating a lack of ordering of the polymer surface. The random orientation of the polymer surface may result from the surface restructuring processes that amphiphilic polymers are expected to experience upon immersion in water or simply because of the swelling of polymer chains. Water signals dominate the SFG spectra at the polymer/water interfaces, with a stronger band at 3200 cm^{-1} and a weaker signal at 3400 cm^{-1}, assigned to strongly hydrogen-bonded and weakly hydrogen-bonded water, respectively. While the shape of the water spectra is similar for all of the polymers, the signal intensity varies depending upon the polymer surface structures, indicating the different ordering of the interfacial water molecules on different polymer surfaces. For example, an increase in the number of the NF units at the outer edge of the peptoid (15 1, 15 2, and S1) leads to a decrease of the water signal as a result of the unfavorable interaction between the hydrophobic fluorocarbon chains and water molecules, which disrupts the ordering of the interfacial water molecules. These SFG water spectra show that the hydration of the polymer surfaces is sensitive to the sequence of the peptoid (both the number and position of the fluorocarbon chains), revealing a subtle trade-off between the dragging effect on and the surface suppression of the hydrophilic components by the NF units.
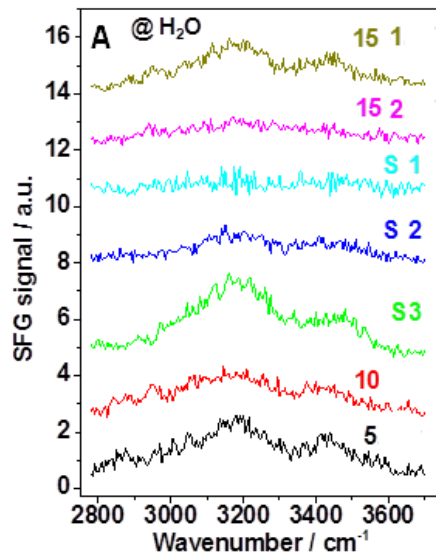
Figure 5-11 SFG spectra of the polymer/water interfaces for different polymers. There is little ordering of the polymer in the films, and the signal is dominated by the strongly and weakly hydrogen bonded water at the surface of the film.

5.4.3   *Antifouling and fouling release performance*

These surfaces were used to study the effect of sequence and surface chemistry on the settlement (attachment) of zoospores and the adhesion strength of sporelings (young plants) of *U. linza*, a widely studied fouling alga. In this system, polystyrene imparts stability to the film, but it is known to be attractive to spore settlement and is thus undesirable at the surface[113]. In this case, the heptafluorobutyl groups are used to not only direct the surface chemistry but also as the hydrophobic residue of our amphiphilic coating. Figure 5-12 shows the settlement and release performance of these films against *U. linza*.

Assays with zoospores showed that while all the surfaces were antifouling with respect to the glass and PDMS standard, the sequence in the peptoid affects both settlement behavior as well as the release properties of sporelings, the young plants that develop from settled spores. Notably, the position of the fluorinated residues in the peptoid has a large effect on the spore settlement density, with the most settlement on the peptoid with the fluorinated NF residue on the end of the peptoid. This may be due to the decreased amount of PEO at the surface, meaning that PEO is better at antifouling than the peptoid itself. While methoxyethyl peptoids have not been previously tested against *Ulva*, they have been shown to be resistant to protein adsorption and cell adhesion, similarly to PEO[114]. Alternatively, the geometry of the polymers at the surface may play a role. When the fluorinated NF is at the end of the peptoid farthest from the PEO backbone, the surface is populated by fluorinated chain ends whereas when the NF moves toward the PEO backbone, the surface is populated by fluorinated polymer loops. The chain ends will have more available conformations and a lower surface energy than the corresponding loops and may have caused the difference in settlement density. The position does not markedly affect the fouling release properties of the surface.
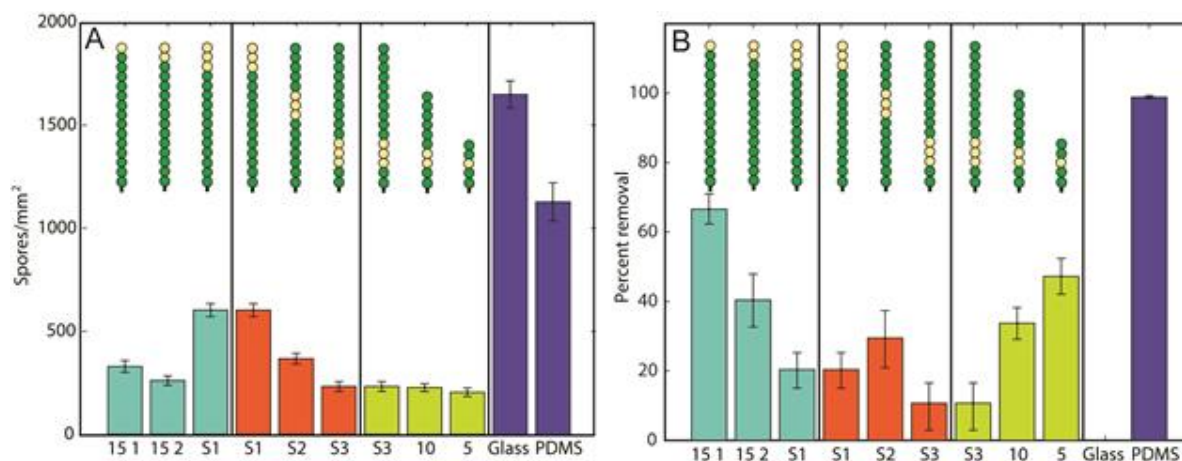
Figure 5-12 Antifouling and fouling-release assays on peptoid surfaces. A) Density of attached spores on peptoid surfaces after 45 min settlement. All surfaces performed well as antifouling materials compared to the glass and PDMS standards. The position of the fluorine in the peptoid affects spore settlement, while peptoid length and fluorine number does not have a marked effect. Each bar is the mean from 90 counts on three replicate slides. Bars show 95% confidence limits. B) Percent removal of sporelings (young plants) from the surfaces after exposure to an impact pressure of 160 kPa, generated by a calibrated water jet. The fluorine content of the peptoid and peptoid length affect fouling-release whereas fluorine position has no effect. As expected, there is high removal of sporelings from the PDMS (fouling-release) standard and no removal from the glass standard. Each bar shows the mean percentage removal of sporeling biomass from 6 replicate slides. Bars show standard error of the mean.

Peptoid length does not markedly affect antifouling. However, both length and number of fluorinated NF residues have a large effect on fouling-release, where peptoids with fewer NF groups have better fouling-release (i.e. higher % removal of sporelings). While this is unusual, as increased fouling release is often associated with higher fluorocarbon content[115], a similar trend was observed by Dimitriou *et al.* at very low fluorocarbon content[99]. It is interesting to note that the dominant antifouling factor in the peptoids of different length is not the size of the peptoid, but the number of fluorinated residues. In the varying length series (S3, 10, 5), the heptafluorobutyl volume fraction in the peptoid was kept the same, meaning that they contained different numbers of NF residues. Both the spore settlement density and the release of sporelings from these peptoids reflected the results obtained for the peptoids with a different number of NF residues.

5.5   Conclusions

We have found that peptoid sequence in our PS-b-P(EO-co-AGE/peptoid) thin films has a profound effect on both surface structure and marine antifouling properties. Using only two peptoid units, a hydrophilic N-(2-methoxyethyl)glycine unit and a hydrophobic N-(heptafluorobutyl)glycine unit, we are able to explore the effect of sequence on the properties of interest. For example, polymer thin films with identical chemical composition but different fluorinated NF group position have different surface composition because the fluorinated group prefers to segregate at the film surface, and will therefore drag portions of the polymer within its proximity to the surface. These films also have different antifouling and fouling-release properties, though it is unclear whether these differences are due to the difference in surface

chemical composition, surface structure, or a combination of the two. Studies of sequence-specific peptoid films must be expanded to identify the most important aspects of the sequence to obtain good antifouling properties. These insights into the relationship between architecture and sequence can be used to design the next generation of amphiphilic antifouling/fouling-release coatings.

6 Effects of polymer chemistry and structure on thin film stability and antifouling/fouling release performance

6.1 Abstract

Here I present work on the optimization of the polymer-peptoid hybrid system introduced in the previous chapter, as well as additional insights into their film structure. First, I introduce a triblock copolymer to replace the diblock morphology for improved mechanical properties, and use secondary ion mass spectroscopy (SIMS) to determine the structure of this polymer on an industrially relevant under layer. Next, I explore perfluorooctane thiol as a tool to direct surface presentation of the polymer system, using NEXAFS and AFM to understand the surface presentation. Finally, I compare the performance of the PS-b-P(EO-co-AGE)-b-PS triblock to that of an opposite polarity backbone, polystyrene-*b*-poly(dimethylsiloxane-*co*-methylvinylsiloxane)-*b*-polystyrene (PS-*b*-P(DMS-*co*-MVS)-*b*-PS). It was found that the coatings using the hydrophobic scaffold, PS-*b*-P(DMS-*co*-MVS)-*b*-PS, performed well against the *U. linza* sporelings, while the coatings using the hydrophilic coatings, polystyrene-*b*-poly(ethylene oxide-*co*-allyl glycidyl ether)-b-polystyrene, PS-*b*-P(EO-*co*-AGE)-*b*-PS, performed well against both *U. linza* and *Navicula* diatoms.

6.2 Thin films using triblocks

In the previous chapter, we used a PS-b-P(EO-co-AGE) polymer scaffold to present peptoids of different sequences on the surface of thin films for antifouling applications. While these films worked, they had limited long term stability in water. Additionally, those films were spin coated directly onto silicon or glass slides for studies. It would be preferable to use a spray coating method, and to apply the peptoid containing active layer on top of a thermoplastic elastomer underlayer. SEBS, (polystyrene-*b*-poly(ethylene-*co*-butylene)-*b*-polystyrene), is a commonly used elastomer underlayer for antifouling applications. Films of SEBS form hard, glass polystyrene (PS) spheres in a rubbery, poly(ethylene-*co*-butylene) (PEB) matrix as seen in Figure 6-1[116].
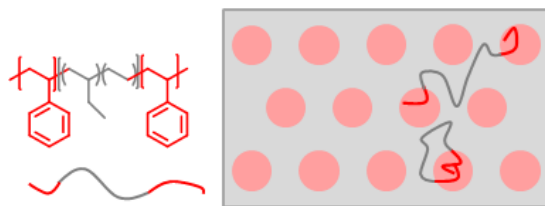
Figure 6-1 Chemical and thin film structure of SEBS.

The PS-b-P(EO-co-AGE) scaffold polymer used in the previous chapter is somewhat compatible with the SEBS underlayer, and was expected to form films with the structure shown on the left of Figure 6-2. It was hypothesized that the PS of the PS-P(EO-co-AGE) copolymer will insert itself into the PS domain of the SEBS (glassy PS spheres inside of a rubbery poly(ethylene/butylene) matrix) as shown in Figure 6-2, and that this morphology will lead to a strong interface between the SEBS and the PS-P(EO-co-AGE). It was also hypothesized that the transition from a diblock morphology (PS-b-P(EO-co-AGE)) to a triblock morphology (PS-b-P(EO-co-AGE)-b-PS) would lead to overall improved film stability because each EO/peptoid polymer has two tether points instead of only one, as shown on the right of Figure 6-2. These

polymers were synthesized, and the thin film morphology was probed using secondary ion mass spectroscopy (SIMS). We find that instead of an insertion of the PS chains into the PS domains, an interfacial PS wetting layer forms between the two layers. Despite this, we found that the triblocks did form stable films, and were used for further antifouling studies.
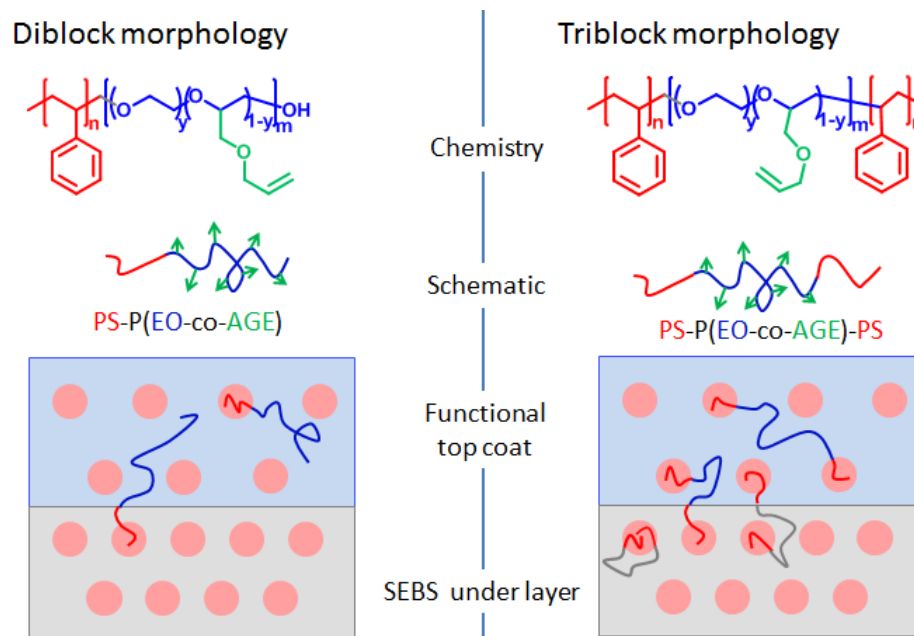
Figure 6-2 Comparison of diblock and triblock morphologies, and the effect on film structure.

6.2.1 *Synthesis of triblocks*

PS-b-P(EO-co-AGE)-b-PS triblock copolymers were synthesized similarly to the diblocks, with a few modifications. First, the P(EO-co-AGE) midblock was synthesized as described in the previous chapter, but using a difunctional initiator (1,4-benzenedimethanol) such that the resulting polymer was terminated with an alcohol on both sides (Figure 6-3A). As expected from anionic polymerization, this synthesis produces clean (Figure 6-3B) and close to monodisperse (Figure 6-3C) polymers.

Next, the difunctional P(EO-co-AGE) was functionalized with N-tert-Butyl-O-[1-(4-chloromethylphenyl)ethyl]-N-(2- methyl-1-phenylpropyl)hydroxylamine (Cl-BzEt-TIPNO)[117] as shown in the first step of Figure 6-4. TIPNO is an initiator for nitroxide-mediated radical polymerization (NMP), a living free radical polymerization method that gives low polydispersity (PDI) polymers due to the dynamic equilibrium between the active and inactive form of the nitroxide propagating chain end [118].

For the TIPNO functionalization, P(EO-co-AGE) was dissolved in dry tetrahydrofuran (THF) in a nitrogen atmosphere drybox. Sodium hydride (5 molar equivalents per alcohol) was added and the solution was stirred for 30 minutes. Chlorobenzyl TIPNO (2 molar equivalents per alcohol) was added to the solution,
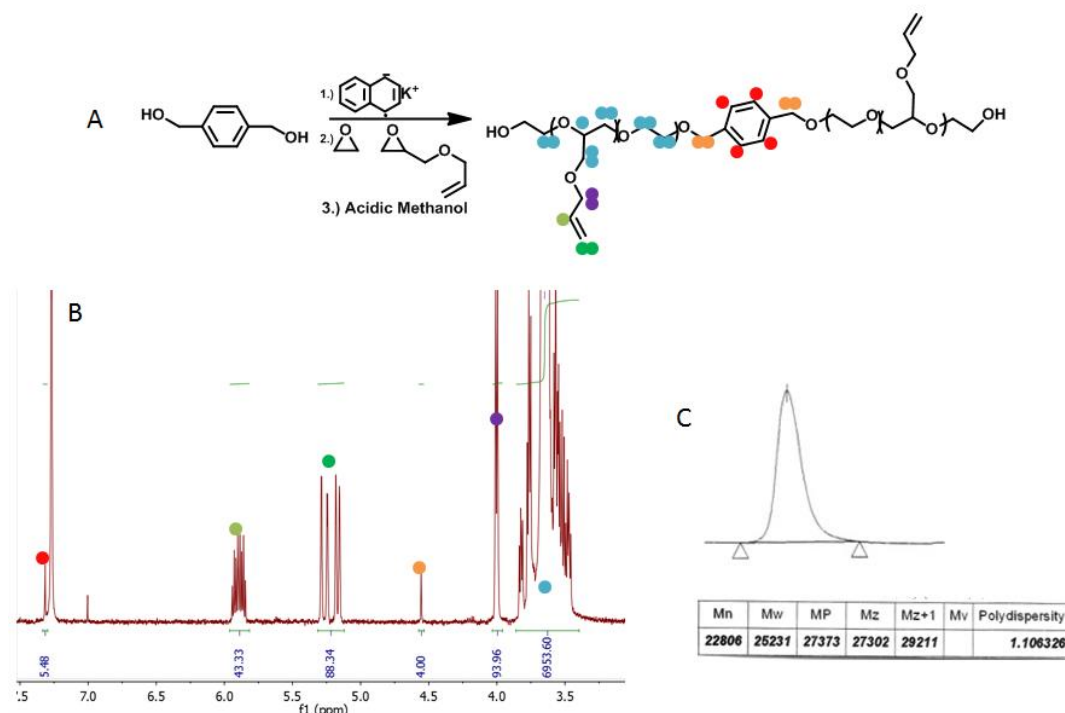
Figure 6-3 Synthesis and characterization of difunctional P(EO-co-AGE). A) The synthetic route. B) A typical NMR of these polymers in CDCl₃ and peak assignments as is coordinated with assignments shown in A. C) GPC trace of the resulting polymer in CHCl₃.
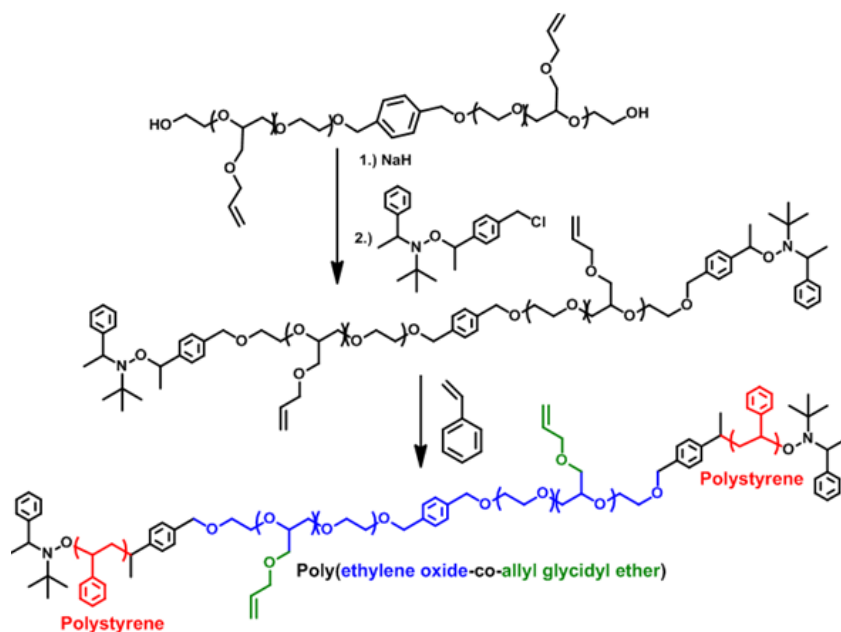
Figure 6-4 Functionalization of difunctional P(EO-co-AGE) with TIPNO and growth of PS to make PS-b-P(EO-co-AGE)-b-PS. The first step involves the deprotonation of the alcohol end groups with NaH and displacement of the Cl to attach the TIPNO initiator. The second step is the nitroxide mediated polymerization of styrene using the TIPNO end groups.

and allowed to react overnight. The solution was then filtered, precipitated into hexanes, and dried under vacuum. End group functionalization was confirmed by 1H NMR spectroscopy. It is possible for allyl to isomerize during the addition of the sodium hydride, as shown in Figure 6-5C. However, this is not observed, as seen in the NMR in Figure 6-5B.

Finally, PS chains were grown as shown in the second step of Figure 6-4. The TIPNO end functionalized P(EO-co-AGE) (5.5 g) was dissolved in 4.4 mL styrene (inhibitor removed) and 17mL toluene. The solution was freeze pump thawed three times, heated to 115 ^{O}C, and allowed to react overnight. The solution was then filtered, precipitated into hexanes, and dried under vacuum. The molar mass and composition were measured by ^{1}H NMR spectroscopy and GPC, as shown in Figure 6-5.
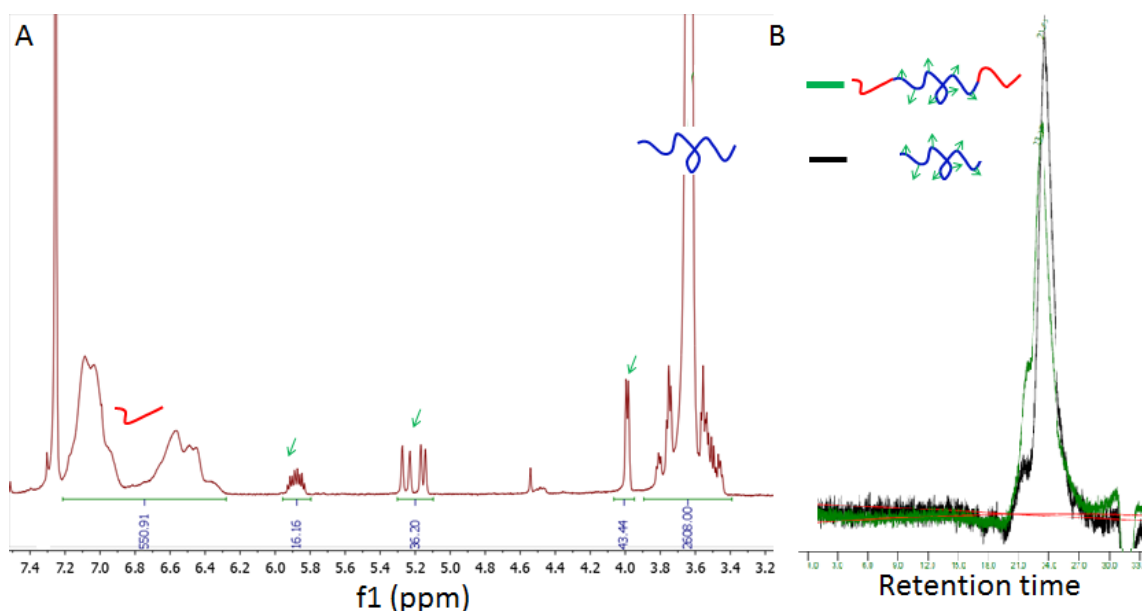
Figure 6-5 Confirmation of successful synthesis of PS-b-P(EO-co-AGE)-PS. A) 1H NMR of the synthesized polymer with peaks assigned. The red and blue portions schematically drawn here are assigned to polystyrene and poly(ethylene oxide), respectively, whereas the green arrows correspond to the allyl glycidyl ether components (the color scheme matches that in Figure 6-4). B) GPC trace before and after copolymerization of difunctional P(EO-co-AGE) with PS. The starting material has a high MW shoulder, perhaps due to polymer coupling. The green trace shows the polymer after growth of PS, and is shifted slightly to higher MW.

6.2.2   *Secondary Ion Mass Spectroscopy (SIMS)*

Secondary Ion Mass Spectroscopy (SIMS) uses a focused ion beam to remove material from the surface of a film in the form of both neutral and ionized species. Once removed, these species are sent to a mass spectrometer for analysis. It is a destructive technique that allows for elemental depth profiling of thin films.

For this experiment, the film shown in Figure 6-6 was used. A silicon substrate containing (^{28}Si) with 300nm of ^{18}O silicon oxide was used. The silicon layer contains only ^{28}Si, while the silicon oxide contains both ^{28}Si and ^{18}O. A layer of SEBS was spin coated onto the silicon wafer out of a 50 mg/mL toluene

solution at 2000 rpm for 30 seconds. This layer was vacuum annealed overnight at 120°C. The SEBS layer contains ^{1}H and ^{12}C so it can be differentiated from the silicon layer. To differentiate the PS in the SEBS layer and the PS-P(EO-co-AGE)-PS layer on top of it, PS-P(EO-co-AGE)-PS was synthesized with deuterated styrene to produce dPS-P(EO-co-AGE)-dPS (20K-(60K, 3 mol% AGE)-20K, PDI = 1.5). The deuterated polymer was spin coated on top of the SEBS out of a 20mg/mL solution in an orthogonal solvent (methyl ethyl ketone) at 2000 rpm for 30 seconds. This was again vacuum annealed overnight at 120°C. So that steady state is reached by the time the ion beam reaches the sample, it is useful to have a 100nm layer of regular PS on top of the stack after annealing. However, we could not find an orthogonal solvent for spin coating the final PS layer, so it was floated onto the stack. The final stack was not annealed.

PS (120 nm) → H, 12C

dPS-PEO-dPS (100 nm) → H, 2H, 12C, 18O
20k-70k-20k (f$_{PEO}$=0.6)

SEBS (250 nm) → H, 12C

SiO$_2$ (300 nm) → 18O, 28Si

Si Substrate → 28Si
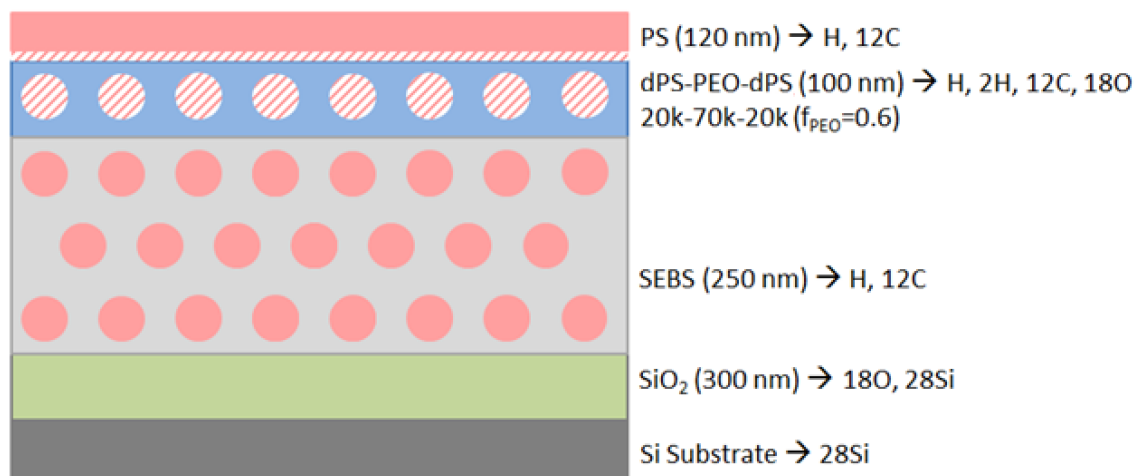
Figure 6-6 Sample preparation for SIMS. Gray is the pure silicon substrate. Green is the silicon oxide layer. Dark pink is PS, while the pink and white stripes are deuterated PS. Blue is P(EO-co-AGE) and the light pink is PEB. We know from NEXAFS experiments that the PS-b-P(EO-co-AGE)-PS films will display PS at the top surface if there are no fluorine groups to change the surface chemistry. For this reason, we have depicted the stack as having a thin layer of dPS between the dPS-b-P(EO-co-AGE-b-dPS and the PS layers.

SIMS was performed by Tom Mates at UCSB. A Cameca ims 5f instrument with cesium as the incident primary ion beam was used. This particular instrument has a 3-15 nm depth resolution (but lateral resolution on the order of 200 nm.) The results are shown in Figure 6-7. The x-axis can be calibrated against the known thickness of the SiO$_2$ layer, but has not been done here. The top of the film is at 0 nm. The top layer contains just ^{12}C and ^{1}H, as expected from a pure PS layer, and ranges from 0 to 190 nm. The next layer, the dPS-b-P(EO-co-AGE)-b-dPS layer ranges from 190-290 nm, and contains ^{12}C, some ^{1}H (but less than in the neighboring layers), ^{2}H from the dPS, and a small amount of ^{18}O from the EO layer. The SEBS layer ranges from 290-1000nm and contains only ^{12}C and ^{1}H. The presence of distinct layers suggests that there is no mixing of layers, despite the annealing above the Tg of PS. The spike of ^{28}Si and ^{18}O at 185 nm are likely due to impurities introduced when the PS layer was floated onto the film. While the depth resolution of the SIMS was not sufficient to conclusively confirm the existence of a PS-rich layer at the interfaces between the dPS-b-P(EO-co-AGE)-b-dPS layer and adjacent layers, the small spikes in ^{2}H intensity at either interface does suggest interfacial dPS enrichment, as would be consistent with NEXAFS studies presented in the previous chapter.
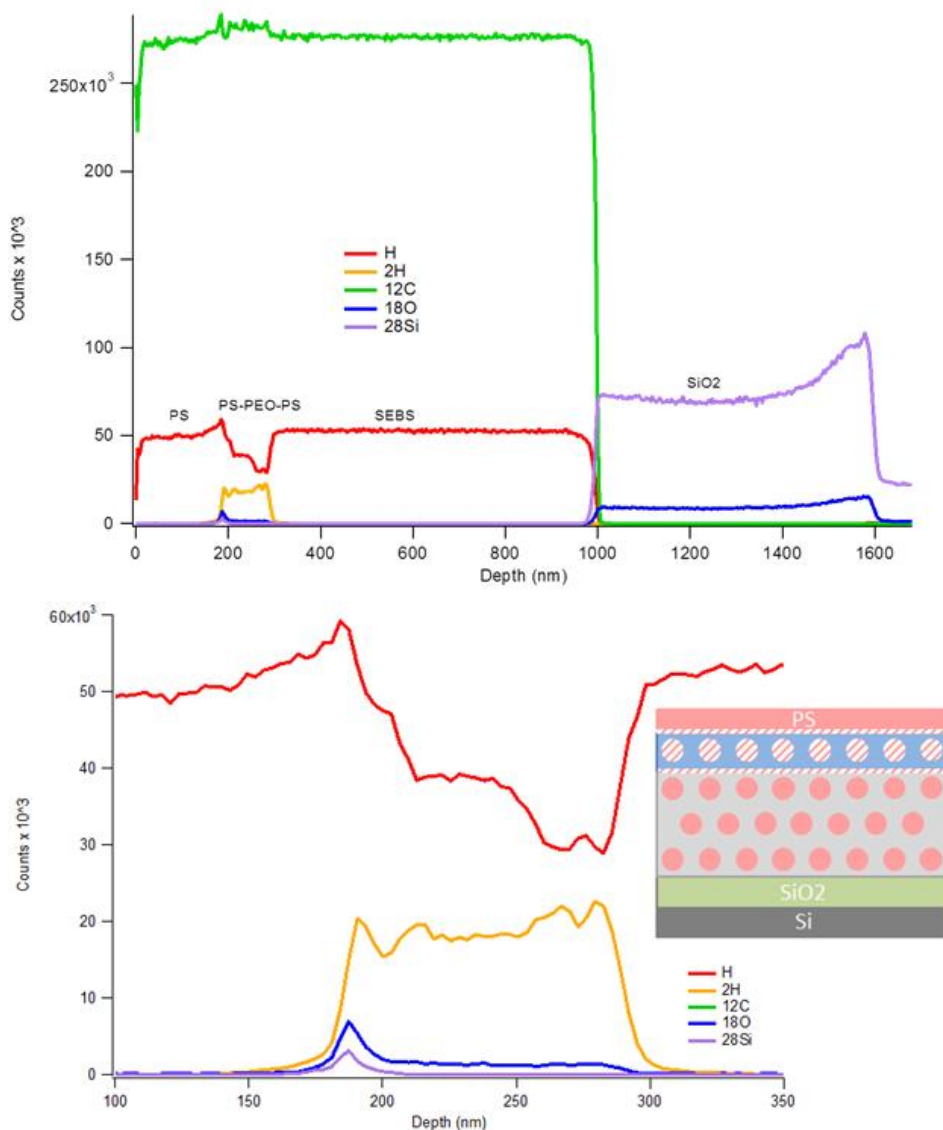
Figure 6-7 SIMS results and schematic of film structure. The top shows the counts of the detected elements for the entire film thickness while the bottom shows the zoomed in section of the dPS-b-P(EO-co-AGE)-b-dPS layer and adjacent layers. The spike of ^{28}Si and ^{18}O are likely due to impurities introduced when the PS layer was floated onto the film. The data suggests that instead of mixing into the SEBS layer, the dPS forms a wetting layer on both sides of the dPS-b-P(EO-co-AGE)-b-dPS layer, as shown in the schematic on the right (where color coding is similar to that indicated in Figure 6-6).

6.2.3   *Surface presentation of peptoids on triblocks*

To ensure that the triblock has similar surface presentation properties as the diblock equivalent studied in the previous chapter, the polymer shown in Figure 6-8 was synthesized and spin coated onto a silicon wafer for NEXAFS experiments that probes the upper 2-5 nm of the film surface. We also studied the stability of prepared films when immersed in water.
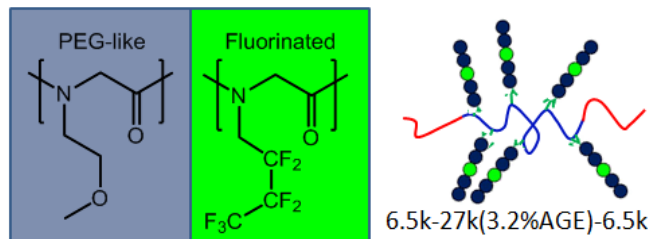
Figure 6-8 A schematic of the peptoid-functionalized triblock. The key on the left shows the peptoid residues, which were those studied in Chapter 5, while the schematic on the right shows the polymer used for this study. The polymer was made of a 27k P(EO-co-AGE) midblock (blue block in schematic) with 3.2mol% AGE (green arrows) and with 6.5k PS endblocks (red block).

The carbon 1s edge NEXAFS spectrum in surface-sensitive PEY mode, shown in Figure 6-9, indicates that the triblock system displays similar surface presentation to the diblock system, indicating that the surface presentation can be controlled by varying the triblock/peptoid composition in a similar fashion as the diblock/peptoid polymers. We see effective surface presentation of the peptoid by the presence of the characteristic C=O and C-F transitions. The polystyrene is successfully inhibited from surface enrichment through the attachment of the peptoid blocks, as seen by the almost non-existent C=C transition, particularly at 120 $^{\circ}$C, which corresponds to a probing depth of ~2 nm. However, the C=C transition does appear at lower angles, indicating that PS is observed deeper in the film, likely at around 5nm from the surface. The overlap of the 30°, 55°, 70°, and 90° spectra allow us to conclude that there is no bulk orientation of these polymers.
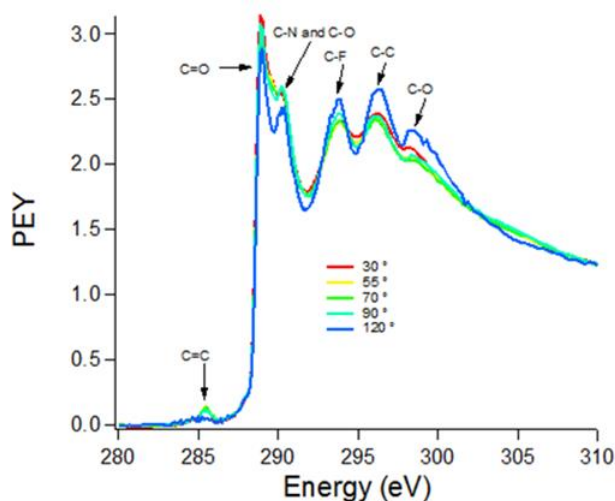
Figure 6-9 Carbon 1s edge NEXAFS spectrum of the peptoid functionalized triblock shown in Figure 6-8. The chemical structures of the polymer components are shown on the right. The different color lines are associated with different incident angles, and probe different depths (2-5 nm) into the film. Substantial overlap is observed in the 55-90° spectra.

However, Figure 6-10 shows that the triblocks, like the diblocks studied in the previous chapter, are not completely water stable. Here, NEXAFS C1s and N1s spectra are presented of triblock films before and after being immersed in water overnight. Before water immersion, negligible PS is observed at the film

surface, as indicated by the small C=C transition peak at 285.5 eV. After immersion, the C=C transition peak has substantially increased and the N peak intensity has decreased, indicating more PS and less peptoid at the surface. It is unclear whether this compositional change is due to reconstruction of the surface, or dissolution of the polymer into water. To address this challenge, a series of polymers with longer PS chains, which limits their water solubility, will be studied in the ensuing section.
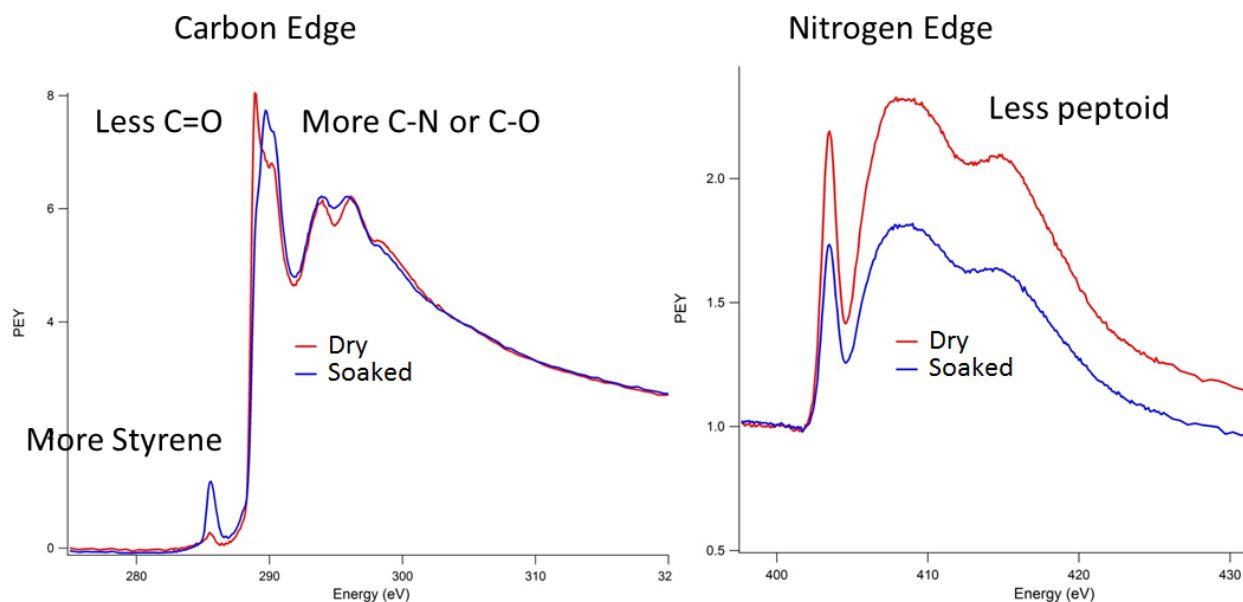
Figure 6-10 NEXAFS C1s and N1s spectra (55°) of a peptoid-functionalized triblock (shown in Figure 6-8) thin film before and after immersing in water.

6.3 Using polystyrene molecular weight and perfluorooctanethiol (PFOT) content to control surface chemistry

6.3.1 *Materials used*

While the method of incorporating fluorine into the peptoid to direct the peptoid to the surface of the film was very effective, it is synthetically nearly impossible to use this method for some peptoid chemistries. The body of anti-fouling literature using charged surfaces, particularly zwitterionic surfaces, makes peptoids a prime candidate for anti-fouling studies. However, charged and fluorinated peptoids are difficult to synthesize and work with due to their limited solubility in solvents. To control the surface presentation of these charged peptoids, we instead click a low surface energy fluorinated group, perfluorooctanethiol (PFOT), directly onto the P(EO-co-AGE) backbone as shown in Figure 6-11. The hypothesis is that the PFOT will surface segregate, thereby bringing the adjacent PEO backbone and peptoid to the surface, burying the PS.
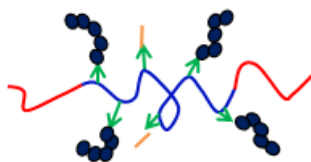
Figure 6-11 Schematic of using PFOT together with peptoids on PS-b-P(EO-co-AGE)-b-PS. Polystyrene is red, the PEO backbone is blue, peptoids are the dark dots, PFOT are the orange lines, and the green arrows are the functionalized allyl groups.

The PS-b-P(EO-co-AGE) diblocks and triblocks were functionalized with PFOT using thiolene click chemistry, as described in the previous chapter and as shown in Figure 6-12. As shown in Figure 6-12C, the duration of the UV exposure was used to control what fraction of the allyl groups were functionalized with PFOT. The final percent functionalization was monitored through the disappearance of the allyl groups using 1H NMR. The same 35k PEO midblock with 1.1 mol% AGE was used for all studies.
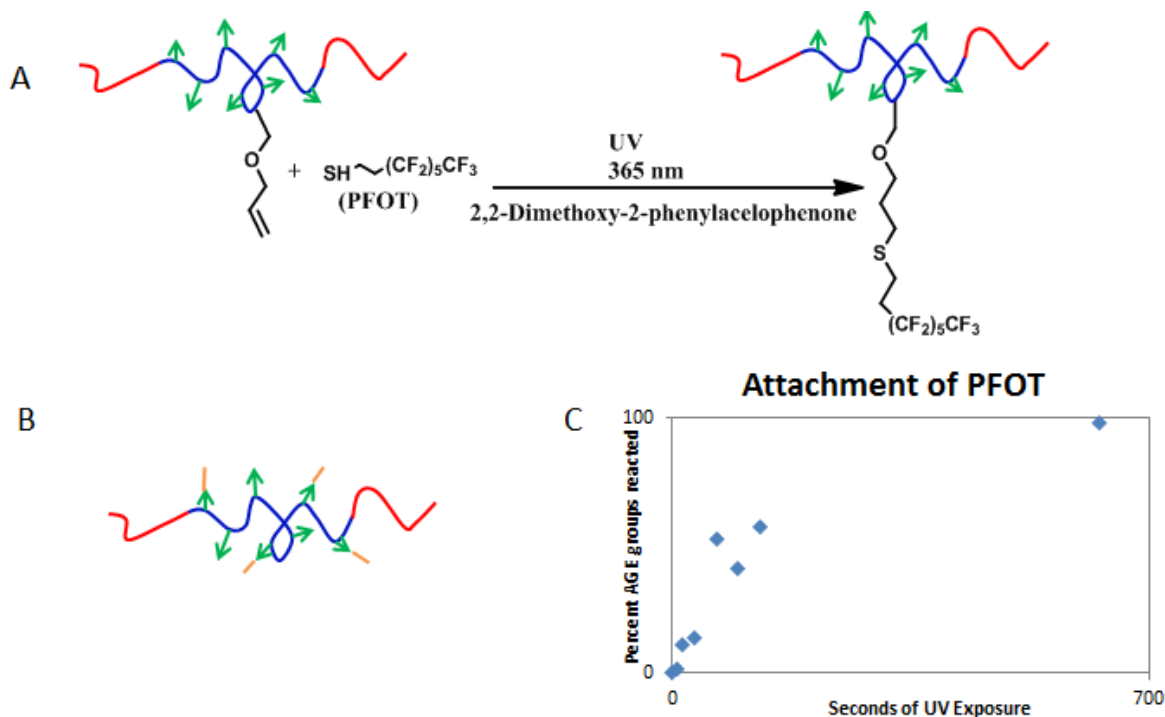
Figure 6-12 Functionalization of PS-b-P(EO-co-AGE)-b-PS with PFOT. A) Thiol-ene click chemistry was used to functionalized the polymer. As shown in B) only a fraction of the pendent allyl groups were functionalized with PFOT, leaving some allyl groups for peptoid functionalization. C) Shows the relationship between the duration of UV exposure and the percent of the allyl groups that were functionalized by PFOT.

Here we also explore the effect of PS molecular weight, because increased PS molecular weight decreases solubility in water and imparts water stability. However, there should be a minimal amount of PS actually present at the surface because of its poor antifouling properties. The polymer series used to explore this

68

tradeoff is shown in Table 6-1. The letter indicates the backbone polymer used, while the number indicates the fraction of the allyl groups that were functionalized with PFOT. For example, C2 is a 20k PS-b-35k P(EO-co-AGE)-b-20k PS polymer where 50% of the allyl groups have been functionalized with PFOT.

Table 6-1 Polymers used in this study. The letters indicate the polymer backbone, while the number indicates the PFOT content. The same 35k PEO midblock with 1.1mol% AGE was used for all triblocks (A-D). The diblock (E) is 22k PS, 46k PEO, with 3mol% AGE. Both PS molecular weight and PFOT content were determined using NMR. Boxes without Xs indicate polymers were not synthesized.

	0: 0% PFOT	1: 25% PFOT	2: 50% PFOT	3: 75% PFOT	4: 100% PFOT
A: 8.6kPS	X	X	X	X	X
B: 12k PS	X		X		X
C: 20k PS	X	X	X	X	X
D: 57 PS	X	X	X	X	X
E: Diblock	X		X		X

6.3.2   *Thin film characteristics*

1.1.1.1   NEXAFS
The NEXAFS spectra shown in Figure 6-13 provide insight into how PS MW and PFOT content affects the surface composition of these thin films. All samples here were spin coated onto SEBS, soaked in water overnight, then dried prior to NEXAFS characterization. Figure 6-13B shows the spectra for the B series of polymers, which have an intermediate size of PS and various PFOT contents. As expected, when there is no PFOT, the surface is dominated by polystyrene (and looks like the schematic on the left of Figure 6-13). As the amount of fluorine (in the form of PFOT) is increased, the amount of PS on the surface decreases, and the amount of PEO and fluorine at the surface increases, indicating that the film looks more like the schematic on the right of Figure 6-13D). We expected a similar trend for the polymer comprised of shorter PS endblocks, series A. However, we see in Figure 6-13A that A1 does not follow the expected trend. The surface of A1 looks much more like SEBS (in black) than either PS or PEO. This suggests that this shortest polymer with a minimal amount of PFOT is not sufficiently hydrophobic to prevent dissolution in water, and higher PS content or higher PFOT content polymer are required for stable films. Figure 6-13C shows the effect of increasing PS molecular weight at a fixed PFOT content. We see that as the length of the PS chains increases, the amount of PS at the surface increases, and the amount of PEO decreases. It is interesting to note that the diblock has the lowest PS content at the surface, though this is likely due to the higher PFOT concentration at the same percent PFOT (the diblock contains 3.5mol% AGE while the triblock contains 1.1mol% AGE).
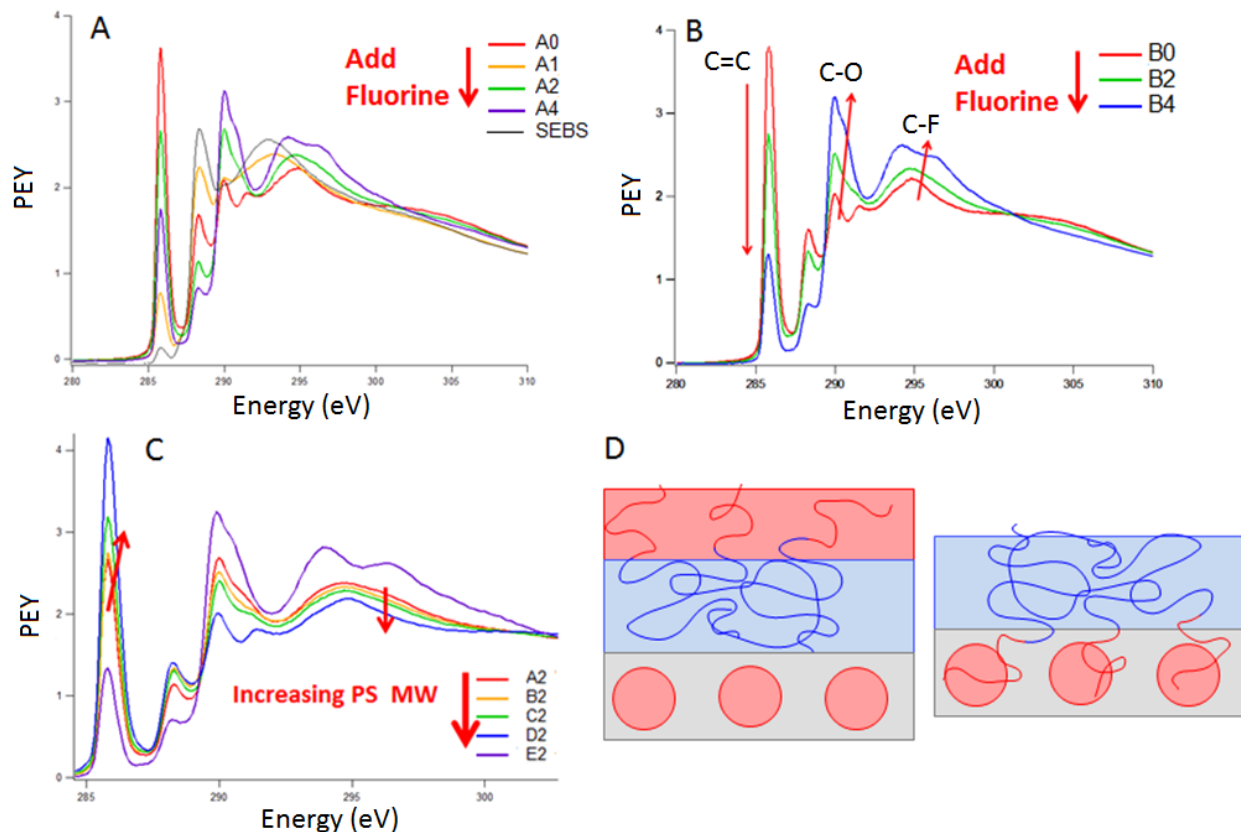
Figure 6-13 NEXAFS C1s spectra (55°) of triblock thin films after soaking is water. A) All members of series A from Table 6-1, with different PFOT contents. B) Series B members with different PFOT contents. C) Shows the effect of increasing PS MW at a fixed PFOT content (column 2 members of Table 6-1). D) Schematics of potential film structure, where the red segments are polystyrene, the blue segments are PFOT-functionalized P(EO-co-AGE), and gray segments are poly(ethylene-co-butylene) .

1.1.1.2   Bubble contact angle

Contact angles were determined using a ramé-hart Model 290 standard automated goniometer. The sample was immersed upside down in ultrapure water and an air bubble was placed onto the surface (Figure 6-14). It is interesting to note that as the fluorine content increases, the hydrophilicity of the surface actually increases (Figure 6-14). The first explanation is simply the effective displacement of the PS with PEO, suggesting that the hydrophilic nature of the PEO offsets the hydrophobicity of the PFOT groups at the surface. However, it is possible that when immersed in water, the PEO swells, allowing the normally crystalline PEO chains to be mobile. This mobility in turns allows the hydrophobic PFOT to rearrange and bury into the film, leaving predominantly PEO at the surface. Such rearrangement has been observed by our group in the past.[102] It is also interesting to note that despite the difference in PS peak size seen in the NEXAFS spectra as PS MW increases, the contact angle of these surfaces is not particularly dependent on the PS content.
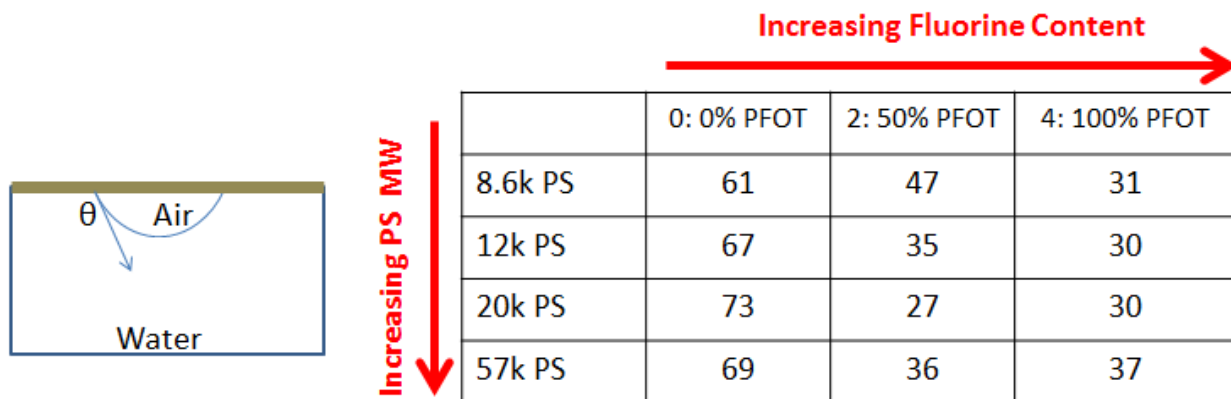
Figure 6-14 Bubble contact angle measurements of different triblock films. The left shows a schematic of the setup while the right shows the bubble contact angle of a variety of films. The film's hydrophobicity is not strongly correlated with PS MW, but surfaces become more hydrophilic with the addition of PFOT.

1.1.1.3 AFM

NEXAFS proves useful insight into the chemical composition of the thin films studied. Because the beam spot used for NEXAFS is about 1mm in diameter, the information gained is an average over that area. Tapping mode atomic force microscopy (AFM) provides additional insight into the surface patterns of these films. These measurements were conducted on a Digital Instruments MultiMode AFM equipped with a Nanoscope IIIa controller. Silicon cantilevers (Nanosensors, type PPP-NCL-50, force constant 21−98 N/m, resonance frequency 146−236 kHz) were used. The images in Figure 6-15 indicate that the films are very inhomogeneous. While the NEXAFS indicated that the surface of C0 (Table 6-1) is dominated by PS with very little PEO and PFOT, we see that the surface is in fact microphase separated into what appear to be mesas and valleys. We also see from the patterned surface that C2 has a highly crystalline surface, despite the fact that this material is not crystalline in the bulk. This observation suggests that the PFOT functionalities are driven to the surface by their low surface energy, where they then crystalize. This agrees with the high C-F coverage seen in the NEXAFS, but again indicates that the surface is highly heterogeneous, which may affect antifouling properties. More studies are required to better understand these inhomogeneities, particularly upon film hydration.
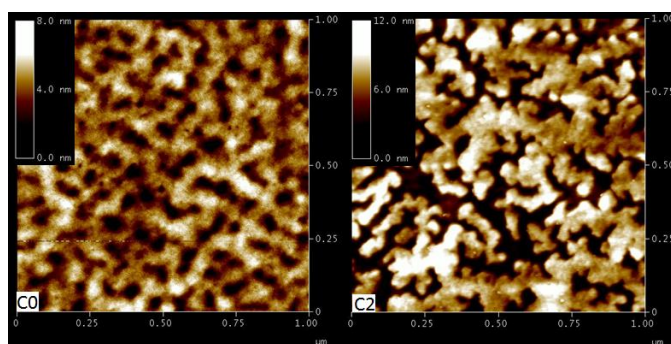
Figure 6-15 Height AFMs of C0 and C2 (Table 6-1) thin films. The AFM on the left shows that the triblock with no PFOT is microphase separated. The AFM on the right shows when the same polymer is 50% functionalized with PFOT, the PFOT crystalizes very strongly at the film surface.

6.4 Effect of backbone chemistry on antifouling performance

In the previous chapter it was shown that peptoid composition and sequence affects surface presentation and antifouling properties, while in the previous section it was shown that the structure of the scaffold polymer (diblock vs triblock and relative block sizes) also affects surface presentation. In this section, we explore different polymer backbones to present the sequences of interest. A natural analog to peptoids are polypeptides, naturally occurring sequence specific proteins. While these peptides are more challenging to work with than peptoids, they also have the sequence specificity desired for this study. For this reason, we compared the surface presentation of peptoids and pepides with the similar functional group sequences. We also compare the PS-b-P(EO-co-AGE)-b-PS scaffold to an equivalent molecular weight polystyrene-*block*-poly(dimethylsiloxane-*stat*-methylvinylsiloxane)-*block*-polystyrene (PS-b-P(DMS-co-MVS)-b-PS) scaffold. PMDS was chosen for its known fouling release properties[119], stable film formation in aqueous environments, and opposite polarity to the original PEO system.

6.4.1 *Pep(toid/tide) and P(EO/DMS) polymers made*

The PDMS based triblocks and the non-natural oligopeptides were synthesized by David Calabrese and Brandon Wenning in Chris Ober's group at Cornell. The structures of the polymers used for this study are shown in Figure 6-16. They synthesized their materials using methods similar to those used for PEO based triblocks (anionic) and peptoids (solid phase synthesis) as described in the previous chapter. Comb copolymers were prepared as in the previous chapter, using thiolene click chemistry to attach the thiol terminated pep(toid/tide) to the pendent carbon-carbon double bond pendent to the polymer midblock (vinyl in the PDMS and allyl in the PEO). More details can be found in our manuscript.[120] Both PDMS and PEO-based triblock copolymers shown in Figure 6-16 had polystyrene endblocks of 7 kDa, and a middle block of 70 kDa. There was a 2.6 mol% inclusion of vinyl/allyl groups in the middle block in both triblock copolymers.

This series of polymers allowed for the systematic comparison of hydrophobic (PDMS) vs hydrophilic (PEO) scaffold chemistry, as well as perfluorinated groups vs hydrocarbons, and peptoids vs peptides. While this series is by no means exhaustive, it was designed to explore a variety of parameters, and determine which ones have the largest effect on antifouling properties.

6.4.2 *Thin film formation*

Standard microscope glass slides (3 in × 1 in.) were treated with freshly prepared piranha solution (7:3 v/v, mixture of concentrated H_2SO_4 and 30 wt% H_2O_2 solution) overnight, and then sequentially rinsed with distilled water and anhydrous ethanol before drying with nitrogen gas. The dried clean glass slides were then immersed in 3.5% (v/v, in anhydrous ethanol) 3-(aminopropyl)trimethoxysilane solution at room temperature overnight, followed by washing with water, anhydrous ethanol, and drying using nitrogen. The aminosilane treated glass slides were cured by heating to 120°C in a vacuum oven at reduced pressure for 2 h before slowly cooling down to room temperature. The first layer coating was applied on the silane treated glass slides by spin coating with a maleic anhydride-functionalized SEBS/unfunctionalized SEBS solution (2% w/v MA-SEBS and 7% w/v SEBS) in toluene (2500 rpm, 30 sec), followed by baking the glass slides at 120°C in a vacuum oven at reduced pressure for 12 h, allowing the maleic anhydride groups in the polymer backbone to react with amine groups on the glass surfaces, therefore improving the bonding of the coating to the glass. The second layer was spin coated

with SEBS solution (12 % w/v SEBS solution) three times (2500 rpm, 30 sec.), followed by further baking at 120°C in a vacuum oven at reduced pressure for 12 h to give a base layer thickness about 1 mm. The modified triblock solutions (16 mg/mL, toluene) was finally spray coated on the surface using Badger model 250 airbrush and 50 psi nitrogen gas, and annealed in a vacuum oven at reduced pressure at 60°C for 12 h, and then 120 °C for 12 h to ensure the complete removal of the solvents.

Unfortunately samples 160 and 162 were not used because of delamination of the film during the antifouling experiment, as seen in the pictures in Figure 6-16. It is interesting to note that this delamination did not result in dissolution. It is likely that the delamination occurred due to poor incorporation of the PS into the SEBS under layer, and not due to overall polymer solubility. This problem did not manifest itself for the spin coated samples, only the spray coated samples. It is well known that processing, specifically spray vs spin coating, can affect film surface structure[121], and this delamination problem suggests that the processing also affects the polymer-polymer interface.

6.4.3 *Analysis of antifouling/fouling release data*

These surfaces were tested against both *Ulva linza* sporelings and *Navicula* diatoms. These two species have been shown to have very different mechanisms for biofouling. *U. linza* tend to settle more aggressively on hydrophilic surfaces, and avoid hydrophobic surfaces with lower surface energy[122]. Ulva spores are motile, meaning that they actively explore surfaces and are able settle selectively. On the other hand, *Navicula* diatoms tend to attach strongly to hydrophobic structures, and are easily removed from hydrophilic surfaces. *Navicula* are not motile making them gravity settlers[122]. Due to the different polarities of the two polymer backbones, testing against these two different types of biofoulants provides insight into the versatility of a given polymer against different biofoulants.

Spore settlement of *U. Linza*, characterized using methods outlined in the previous chapter, on peptide containing surfaces is shown in Figure 6-17A. All of the peptide containing coatings have lower settlement than the glass control and the unfunctionalized PS-*b*-P(DMS-*stat*-MVS)-*b*-PS triblock copolymer. This shows that all of the amphiphilic coatings have antifouling properties, regardless of whether the hydrophobic moiety is a hydrocarbon or perfluorinated. On the PS-*b*-P(EO-*stat*-AGE)-*b*-PS triblock, it appears that the perfluorinated peptide is more antifouling than the hydrocarbon counterpart, but the same is not true on the PS-*b*-P(DMS-*stat*-MVS)-*b*-PS triblock. Overall, there does not appear to be any significant difference between the two triblock copolymers for initial settlement of spores.

The fouling release data in Figure 6-17B shows that the PS-*b*-P(DMS-*stat*-MVS)-*b*-PS surfaces overall had better removal than the PS-*b*-P(EO-*stat*-AGE)-*b*-PS surfaces, and outperformed the PDMSe control. It is important to note that the percent removal is often affected by the initial spore settlement. Samples with high spore settlement, such as the unmodified VMS surface, often have high percent removal. However, the modified PS-*b*-P(DMS-*stat*-MVS)-*b*-PS surfaces, DPH and DFH, have both low initial settlement, and high %removal, indicating the improvement of performance in antifouling and fouling release with the peptide modification. The modified PS-*b*-P(EO-*stat*-AGE)-*b*-PS surfaces showed fouling release properties comparable to the PDMSe control, while the unmodified triblock surface was a poor fouling release surface. Again, this shows that the peptide modification enhanced fouling release performance of the PS-*b*-P(EO-*stat*-AGE)-*b*-PS surfaces.
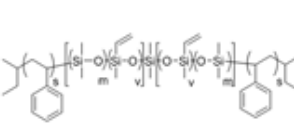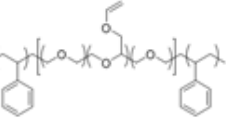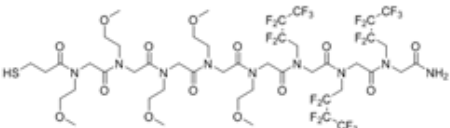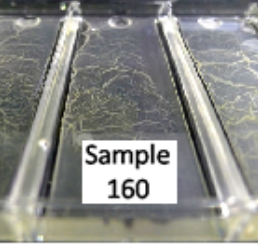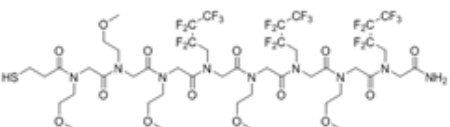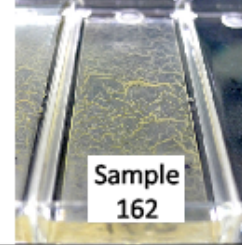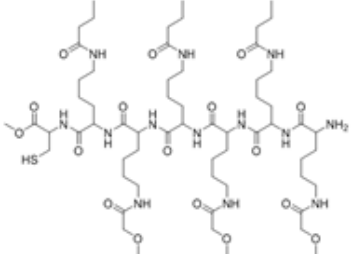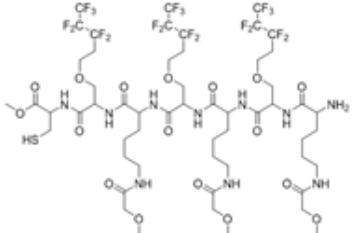
Polymer / Side Group	PS-P(DMS/VMS)-PS	PS-P(EO/AGE)-PS
Block Peptoid	Sample 159	Sample 160
Alternating Peptoid	Sample 161	Sample 162
Alkyl Alternating Peptide	Sample DPH	Sample APH
Fluoro Alternating Peptide	Sample DFH	Sample AFH

Figure 6-16 Polymers synthesized to explore differences between hydrophobic and hydrophilic scaffold chemistries. This series of polymers allowed for the systematic comparison of hydrophobic (PDMS) vs hydrophilic (PEO) scaffold chemistry, as well as perfluorinated groups vs hydrocarbons, and peptoids vs peptides. Sample 160 and 162 were not used because of delamination of the film during the antifouling experiment, as seen in the pictures.

74

The spore settlement on peptoid containing surfaces is shown in Figure 6-17C. Both of the peptoid coatings on PS-*b*-P(DMS-*stat*-MVS)-*b*-PS triblocks show very high spore settlement, and comparable or higher settlement than the unmodified VMS surface, showing that there is no antifouling benefit of the peptoids on these surfaces. The fouling release behavior of these surfaces in Figure 6-17D equally poor performance of the peptoid-containing polymers. While the percent removal is fairly high, it is about the same as the unmodified VMS surface. The cause of this poor behavior will be explored in the next section, with NEXAFS providing insights of surface composition of each film.
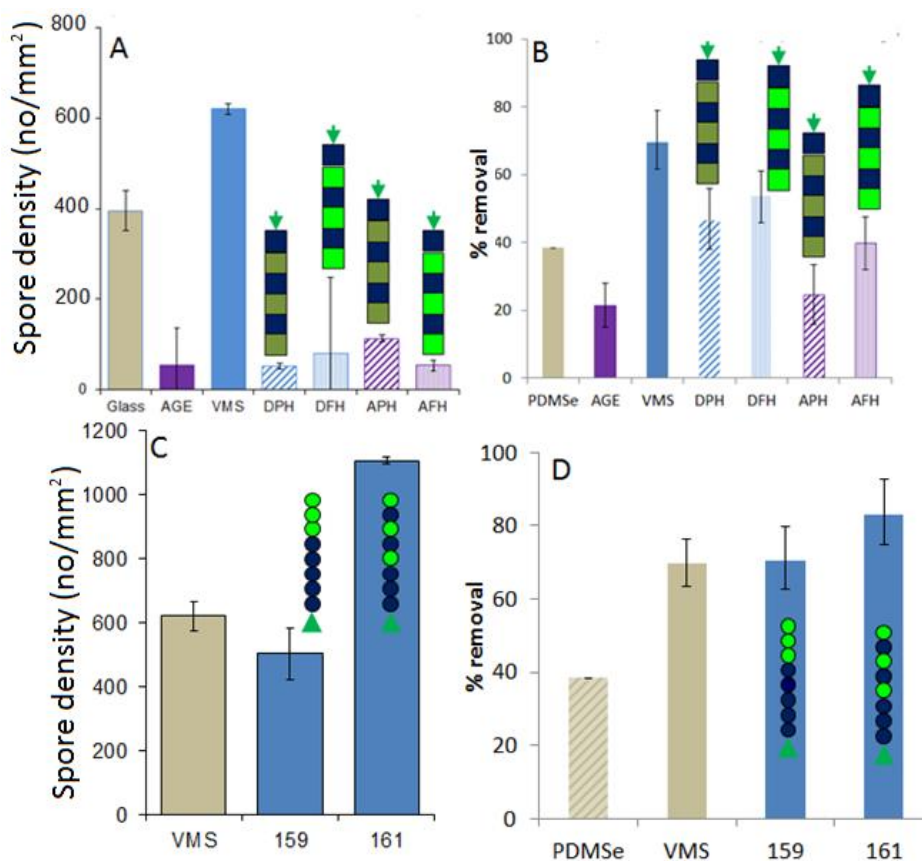
Figure 6-17 U. linza settlement and removal data from peptoid and peptide surfaces. A) Density of attached spores on peptide sequences on the PEO and the PDMS scaffold after 45 min settlement. DPH, DFH, APH, AFH, 159, and 161 structures are provided in Figure 6-16, VMS is the unfunctionalized PDMS surface, AGE is the surface from unfunctionalized PS-P(EO-co-AGE)-PS triblock, while glass and the PDMSe samples are literature controls. Each bar is the mean from 90 counts on three replicate slides. Bars show 95% confidence limits. B) Percent removal of sporelings (young plants) from the same surfaces as in (A) after exposure to an impact pressure of 160 kPa, generated by a calibrated water jet. C) Density of attached spore on two peptoid sequences on the PDMS scaffold, and the unfunctionalized PDMS surface. D) Percent removal from the same surfaces.

Navicula settlement and attachment strength assays were performed as describe elsewhere[123]. The cells were allowed to precipitate through the fouling test solution and land on the coating surfaces. After allowing the Navicula 120 minutes to settle, these surfaces are then washed gently with water to remove

unattached and weakly attached cells. The resulting attachment density measured in this assay reflects differences in the ability of cells to attach firmly to the. For fouling release tests, the settled slides were explosd to a shear stress of 33 Pa in the same water channel as used in the previous chapter for *U. linza.* *Navicula* settlement densities of coatings are shown in Figure 6-18. We see that attachment of the *Navicula* on the modified PS-b-P(DMS-stat-MVS)-b-PS coatings was higher than on the unmodified PS-b-P(DMS-stat-MVS)-b-PS coating. While the oligopeptides are able to improve the PDMS-based triblock copolymer performance against *U. linza* sporelings, they seem to hinder the antifouling properties against *Navicula* diatoms.

However the modified PS-b-P(EO-stat-AGE)-b-PS coatings show less attachment than the unmodified control. In fact, the PEO based coatings modified with the fluorinated oligopeptides are superior to all of the coatings for antifouling against *Navicula* diatoms including the PDMS standard. This shows that for the PS-b-P(EO-stat-AGE)-b-PS backbone, the oligopeptides are able to reduce the diatom settlement density on the coatings. The perfluorinated peptide shows the largest enhancement in antifouling behavior. It is interesting to note that the same peptides have opposite effects on the antifouling ability of the surfaces depending on the polymer backbone. As we will see from the NEXAFS data, this is due to differences in driving forces of surface presentation for the two polymer backbones.

The *Navicula* fouling release data in Figure 6-18B shows that only the two modified PS-b-P(EO-stat-AGE)-b-PS coatings showed significant removal of the diatoms from the surface. The lack of any removal of the diatoms from the unmodified PS-b-P(EO-stat-AGE)-b-PS coating shows that the oligopeptides on the PS-b-P(EO-stat-AGE)-b-PS triblock copolymer have a significant effect on the fouling release performance of the surfaces. None of the modified PS-b-P(DMS-stat-MVS)-b-PS based coatings showed any significant fouling release of the diatoms.

6.4.4   *Driving forces of surface presentation in PDMS vs PEO based triblock systems*

The representative PEY mode NEXAFS spectra, where the top 2-5 nm of the film surface are probed, shown in Figure 6-19 provide insight into the driving forces for surface presentation and the antifouling performance of film surfaces prepared from polymers shown in Figure 6-16. The carbon edge spectrum in Figure 6-19A shows the surface of the unmodified and peptoid containing PS-b-P(DMS-stat-MVS)-b-PS surfaces. In both cases, the spectrum shows predominantly PDMS, as reflected by the characteristic PDMS peak at 287.5 eV (slightly shifted from the polystyrene peak at 285 eV)[120]. The nitrogen edge NEXAFS spectrum of the film surface of polymer 159 in Figure 6-16, the peptoid modified PS-b-P(DMS-stat-MVS)-b-PS (Figure 6-19C), shows a similar surface with almost no peptoid. This observation indicates that the fluorine moieties in the peptoid do not have a sufficiently low surface energy to segregate to the top of the film. Instead, the low surface energy PDMS surface segregates.
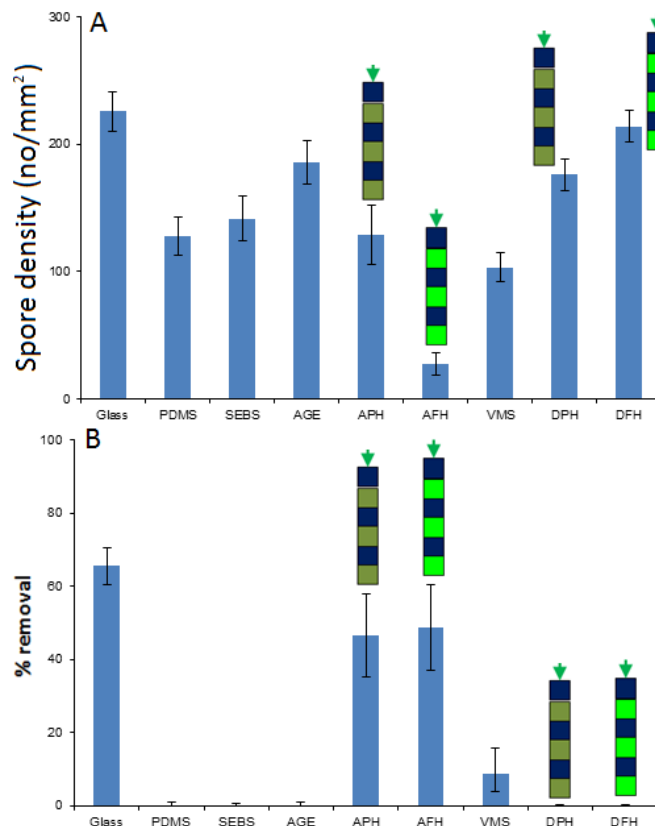
Figure 6-18 Navicula diatom settlement and removal data for peptides on PEO and PDMS scaffolds. Acronyms are provided in Figure 6-16 and Figure 6-17.

When the surface is immersed in water, the hydrophilic segments of the film will migrate to the surface.[120] The peptoids used here are less hydrophilic than the peptide equivalent, because of the hydrogen bond donors present along the backbone of the peptide. This means that when the peptoid containing films are immersed in water, the peptoids do not migrate to the surface, while the peptides do, explaining the antifouling performance of the peptide vs peptoid surfaces on the PDMS scaffold.

The NEXAFS spectra of PS-b-P(EO-stat-AGE)-b-PS surface presentation was similar to the diblock PS-b-P(EO-AGE) discussed in the previous chapter. The unmodified PS-b-P(EO-stat-AGE)-b-PS surface shows predominantly PS while the peptoid modified polymer (polymer 160 in Figure 6-16) shows mostly peptoid and PEO (Figure 6-19B). The nitrogen edge NEXAFS spectrum (Figure 6-19D) of peptoid modified PS-b-P(EO-stat-AGE)-b-PS surface shows a high peptoid content. These data indicate that the surface composition in the PEO triblocks is driven by surface energy, and structure developed during annealing in vacuum. This means that while the PEO triblock is an effective scaffold for the presentation of any fluorinated sequence, the PDMS triblock is only effective for the presentation of very hydrophilic materials.
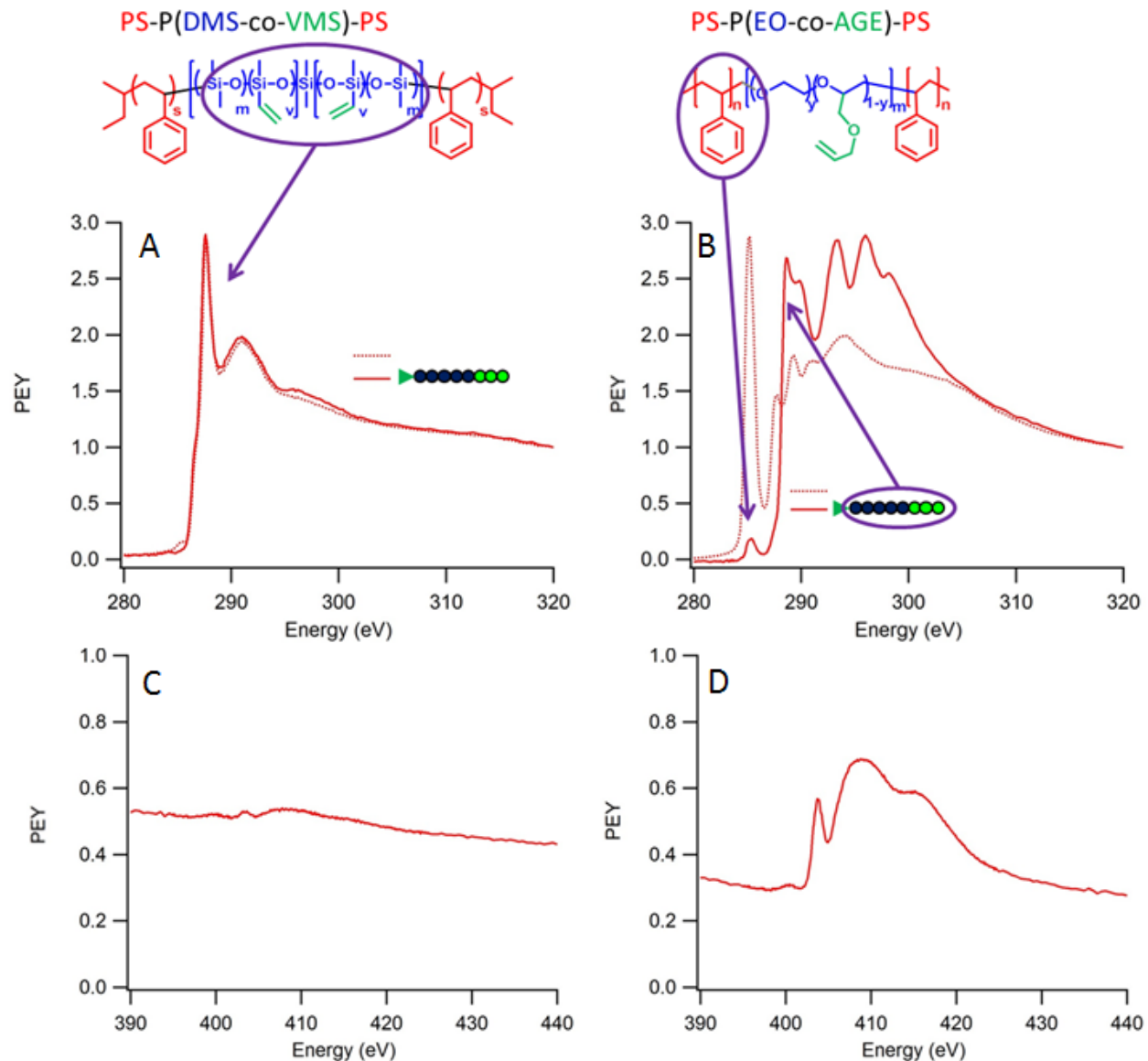
Figure 6-19 NEXAFS C1s and N1s spectra of PEO and PDMS based peptoid-modified triblock polymer surfaces. A) The carbon edge NEXAFS of the unmodified and peptoid containing PS-b-P(DMS-stat-MVS)-b-PS surfaces. In both cases, the spectrum shows predominantly PDMS. B) Carbon edge NEXAFS spectrum of unmodified PS-b-P(EO-stat-AGE)-b-PS surface shows predominantly PS while the peptoid modified polymer shows mostly peptoid and PEO (see Figure 6-9 for carbon edge peak assignments). C) Nitrogen edge NEXAFS spectrum of peptoid modified PS-b-P(DMS-stat-MVS)-b-PS surface shows almost no peptoid on the surface, while D) the nitrogen edge NEXAFS spectrum of peptoid modified PS-b-P(EO-stat-AGE)-b-PS surface shows a high peptoid content.

6.5   Conclusions

Triblock copolymers can be used instead of diblocks to present peptoids at the surface of thin films. As the length of the PS increases, so does the overall polymer hydrophobicity and resulting film stability. It was also found that PFOT is an effective way to control the surface chemistry of PS-b-P(EO-stat-AGE)-

b-PS thin films without introducing fluorine directly onto the peptoid. However, there are still challenges with compatibilizing this system with the underlying elastomer layer, particularly when spray coating. This likely has to do with the formation of a PS wetting layer between the two materials, instead of intermixing, as was originally anticipated. Despite the challenges with making a stable PEO based scaffold, the antifouling performance of these materials is better against the combination of *U. linza* and *Navicula* than the corresponding (and more mechanically robust) PDMS based scaffold. These enhanced antifouling properties are likely due to the more effective surface presentation of anti-fouling constituents than the PDMS based system. Overall, we have gained insights into the film structure of antifouling thin films, and explored methods to improve their stability, their presentation of functional materials, and their antifouling performance.

7 Completed and future work

In this work, we used a poly(allyl glycidyl ether) (PAGE) platform to explore the structure property relationship for polymer battery electrolytes and marine antifouling coatings. The tunable system used in this thesis allowed for the study of a wide variety of properties, and we achieved many of the materials properties desired. However, improvement in materials performance can likely be achieved through the following suggested future research directions.

7.1 Battery electrolytes

7.1.1 *Completed work*

First, we designed materials to have both high ionic conductivity and high cation transference number for use as lithium battery electrolytes. We used a sulfonate functionalized PAGE as dry single ion conducting polymer electrolyte. The material was synthesized using a combination of anionic ring opening polymerization and thiol-ene click chemistry. Composition was confirmed using nuclear magnetic resonance spectroscopy (NMR) and elemental analysis. Due to crystallization of the ionic groups, these materials had very low ionic conductivity by AC impedance spectroscopy, even at 90°C, well above the melting point of PEO. We studied the phase behavior of these materials in bulk, and conclude that to achieve ion dissociation and ionic conductivity, these polymers *must* be dissolved in strong Lewis basic solvents, such as DMSO.

We then showed that when these materials are dissolved in solvents, they have high Li^+ transference numbers (0.80–0.99) and high ionic conductivity (of order 1 mS/cm) at room temperature. The self diffusion coefficients used to calculate the transference number were measured using ^7Li and ^1H pulsed field gradient nuclear magnetic resonance (PFG-NMR). To validate these results and to gain insight into ion dissociation, the calculated conductivities from ion diffusion coefficients measured using NMR were compared against conductivity measured using an electrochemical conductivity probe. Viscosity measurements were used to help decouple the effects of viscosity from molecule size and dielectric friction on diffusion coefficients. These materials demonstrate among the highest combination of transference number and conductivity in a liquid electrolyte reported in the literature.

Further studies of these promising electrolyte materials provided insight into their properties as a function of temperature, polymer molecular weight, solvent, and small molecule additives. The cation transference number was found to be temperature independent, in agreement with theory for solutions that are fully dissociated. Polymer molecular weight was identified as an important parameter that influences Li^+ transference number, the effect of which can only be partially described with existing scaling theories. While all three solvents tested here had high Li^+ transference number and high conductivity, it was found that optimization of transport properties solely through solvent choice is difficult, although having sufficiently high Lewis basicity/acidity to dissociate the ions is critical. Other important solvent parameters include viscosity, which affects overall ionic motion, solvent radius, which affects the size of the Li^+ solvation shell, and a combination of dielectric constant and polymer-solvent interaction parameter, both of which affects the conformation of the polymer chain. The addition of small molecule salts, such as LiTFSI, as additives to the polyelectrolyte solution, was not identified as a promising approach to control t_+ and conductivity.

7.1.2   *Suggested future work*

First, it is critically important that new polymer chemistries are developed. In particular, novel chemistries that allow anions with low effective basicity are necessary to allow higher ion dissociation in lower donor number solvents that will be relevant for Li-based batteries. The sulfonate anion used in this work was effective as a proof of concept, but was insoluble in many solvents of interest, such as carbonates. Proposed anions have more delocalized electron density, either from nearby aromatic rings or electron withdrawing groups, such as structures like bis(trifluoromethan)sulfonamide (TFSI). Several examples of such polyanions exist[6,8,124,125], though it is possible to imagine a variety of other possible chemistries. Lithium neutralized polyanions with solubility in carbonates would enable studies in real batteries. In addition to changing the anion, the electrochemical stability of the polymer should be taken into account. Changing the backbone from PEO to other more stable backbones would be advisable, although improving backbone stability will likely be accompanied by a decrease in polymer solubility, resulting the need for studies to understand how to optimize both.   Furthermore, changing the ion linker chemistry to improve stability over the current thioether linkage is required, and it is suggested that alternative to the thio-ene click are explored in further studies.

Second, it is important to more completely understand the dielectric and electrostatic effects which control cation motion. This thesis reports initial studies that attempt to separate effects of viscous and electrostatic drag, but the self diffusion coefficient of the lithium cation is still not completely understood or predictable. It will be necessary to develop models which describe and predict the cation motion. NMR experiments such as relaxometry, the study of relaxation times, may provide insight into the interactions that influence the motion of the cation. Once these effects are better understood, the principles for appropriate materials design can be used to enable high performance battery electrolytes with optimal lithium conductivity and transference number.

7.2   **Marine anitfouling thin films**

Next we designed poly(styrene)-b-poly(ethylene oxide-co-allyl gylcidyl ether/peptoid) (PS-b-P(EO-co-AGE/peptoid)) polymers to study the effect of peptoid sequence on antifouling thin films. We found that peptoid sequence in our PS-b-P(EO-co-AGE/peptoid) thin films has a profound effect on both surface structure and marine antifouling properties. Using only two peptoid units, a hydrophilic and a hydrophobic unit, we are able to explore the effect of sequence on the properties of interest, namely antifouling and fouling release properties of *Ulva linza*. The resulting surfaces were also analyzed using near edge x-ray absorption fine structure (NEXAFS) spectroscopy and sum frequency generation (SFG) spectroscopy to gain insight into film organization and how that structure is affected by peptoid sequence. These insights into the relationship between architecture and sequence can be used to design the next generation of amphiphilic antifouling/fouling-release coatings.

Finally, we explore the effect of polymer structure on resulting film stability, studying different triblock PS-b-P(EO-co-AGE)-b-PS copolymers instead of diblocks. As the length of the PS increases, so does the overall polymer hydrophobicity and resulting film stability. We also explore different ways to control surface presentation of peptoids at the surface of the thin films, and found that it is also possible to use a perfluorinated group directly on the polymer backbone to direct surface presentation. These triblocks were compared to a similar poly(dimethyl siloxane) (PDMS) triblock, and we found that the antifouling performance of the PEO system is better against the combination of *U. linza* and *Navicula* than the

corresponding (and more mechanically robust) PDMS based scaffold. These enhanced antifouling properties are likely due to the more effective surface presentation of anti-fouling constituents than the PDMS based system. Overall, we have gained insights into the film structure of antifouling thin films, and explored methods to improve their stability, their presentation of functional materials, and their antifouling performance.

More work is needed in to understand the structure of the film while immersed in water. While SFG was used to probe liquid-solid interfaces the utility of this method is limited. Newly developed techniques to provide ambient pressure x-ray photoelectron spectroscopy[126] would provide vital information about hydrated film structure and the surface as it exists when explored for settlement by marine organisms. Additionally, now that sequence has been identified as an important parameter for marine antifouling applications, and we have established a platform to study this effect, it is important to explore more sequences and more chemical functionalities, particularly charged groups, which can mimic and provide insight into antifouling zwitterionic[127] surfaces.

References

(1)   Hosler, D.; Burkett, S. L.; Tarkanian, M. J. Prehistoric Polymers: Rubber Processing in Ancient Mesoamerica. *Science (80-.).* **1999**, *284*, 1988–1991.

(2)   LeClair, M. Lithium Battery Manufacturing in the US, 2016.

(3)   Sylla, S.; Sanchez, J.-Y.; Armand, M. Electrochemical Study of Linear and Crosslinked PEO-Based Polymer Electrolytes. *Electrochim. Acta* **1992**, *31*, 1699–1701.

(4)   Panday, A.; Mullin, S.; Gomez, E. D.; Wanakule, N.; Chen, V. L.; Hexemer, A.; Pople, J.; Balsara, N. P. Effect of Molecular Weight and Salt Concentration on Conductivity of Block Copolymer Electrolytes. *Macromolecules* **2009**, *42*, 4632–4637.

(5)   Hallinan, D. T.; Balsara, N. P. Polymer Electrolytes. *Annu. Rev. Mater Res* **2013**, *43*, 503–525.

(6)   Bouchet, R.; Maria, S.; Meziane, R.; Aboulaich, A.; Lienafa, L.; Bonnet, J.-P.; Phan, T. N. T.; Bertin, D.; Gigmes, D.; Devaux, D.; *et al.* Single-Ion BAB Triblock Copolymers as Highly Efficient Electrolytes for Lithium-Metal Batteries. *Nat. Mater.* **2013**, *12*, 452–457.

(7)   Trapa, P. E.; Acar, M. H.; Sadoway, D. R.; Mayes, A. M. Synthesis and Characterization of Single-Ion Graft Copolymer Electrolytes. *J. Electrochem. Soc.* **2005**, *152*, A2281.

(8)   Porcarelli, L.; Shaplov, A. S.; Salsamendi, M.; Nair, J. R.; Vygodskii, Y. S.; Mecerreyes, D.; Gerbaldi, C. Single-Ion Block Copoly(Ionic Liquid)S As Electrolytes for All-Solid State Lithium Batteries. *ACS Appl. Mater. Interfaces* **2016**, *8*, 10350–10359.

(9)   Inceoglu, S.; Rojas, A. A.; Devaux, D.; Chen, X. C.; Stone, G. M.; Balsara, N. P. Morphology-Conductivity Relationship of Single-Ion-Conducting Block Copolymer Electrolytes for Lithium Batteries. *ACS Macro Lett.* **2014**, *3*, 510–514.

(10)   Lee, B. F.; Kade, M. J.; Chute, J. A.; Gupta, N.; Campos, L. M.; Fredrickson, G. H.; Kramer, E. J.; Lynd, N. A.; Hawker, C. J. Poly(allyl Glycidyl Ether)-A Versatile and Functional Polyether Platform. *J. Polym. Sci. Part A Polym. Chem.* **2011**, *49*, 4498–4504.

(11)   Krogstad, D. V.; Choi, S. H.; Lynd, N. A.; Audus, D. J.; Perry, S. L.; Gopez, J. D.; Hawker, C. J.; Kramer, E. J.; Tirrell, M. V. Small Angle Neutron Scattering Study of Complex Coacervate Micelles and Hydrogels Formed from Ionic Diblock and Triblock Copolymers. *J. Phys. Chem. B* **2014**, *118*, 13011–13018.

(12)   Thelen, J. L.; Inceoglu, S.; Venkatesan, N. R.; Mackay, N. G.; Balsara, N. P. Relationship between Ion Dissociation, Melt Morphology, and Electrochemical Performance of Lithium and Magnesium Single-Ion Conducting Block Copolymers. *Macromolecules* **2016**, acs.macromol.6b01886.

(13)   Thelen, J. L.; Teran, A. A.; Wang, X.; Garetz, B. A.; Nakamura, I.; Wang, Z. G.; Balsara, N. P. Phase Behavior of a Block Copolymer/salt Mixture through the Order-to-Disorder Transition. *Macromolecules* **2014**, *47*, 2666–2673.

(14)   Thelen, J. L. The Influence of Charged Species on the Phase Behavior, Self-Assembly, and Electrochemical Performance of Block Copolymer Electrolytes, 2016.

(15)   Hexemer, A.; Bras, W.; Glossinger, J.; Schaible, E.; Gann, E.; Kirian, R.; MacDowell, A.; Church, M.; Rude, B.; Padmore, H. A SAXS/WAXS/GISAXS Beamline with Multilayer Monochromator.

     J. Phys. Conf. Ser. **2010**, *247*, 12007.

(16) Ilavsky, J. Nika : Software for Two-Dimensional Data Reduction. *J. Appl. Crystallogr.* **2012**, *45*, 324–328.

(17) MacCallum, J. R.; Vincent, C. A. *Polymer Electrolyte Reviews 1*; 1987.

(18) Thünemann, A. F.; General, S. Poly(ethylene Imine) N -Alkyl Carboxylate Complexes. *Langmuir* **2000**, *16*, 9634–9638.

(19) Antonietti, M.; Conrad, J.; Thünemann, A. F. Polyelectrolyte-Surfactant Complexes: A New Type of Solid, Mesomorphous Material. *Macromolecules* **1994**, *27*, 6007–6011.

(20) Mogurampelly, S.; Borodin, O.; Ganesan, V. Computer Simulations of Ion Transport in Polymer Electrolyte Membranes. *Annu. Rev. Chem. Biomol. Eng.* **2016**, *7*, 349–371.

(21) Buss, H. G.; Chan, S. Y.; Lynd, N. A.; Mccloskey, B. D. Nonaqueous Polyelectrolyte Solutions as Liquid Electrolytes with High Lithium Ion Transference Number and Conductivity. *ACS Energy Lett.* **2017**, *2*, 481–487.

(22) Doyle, M.; Newman, J. Analysis of Transference Number Measurements Based on the Potentiostatic Polarization of Solid Polymer Electrolytes. *J. Electrochem. Soc.* **1995**, *142*, 3465.

(23) Thomas, K. E.; Sloop, S. E.; Kerr, J. B.; Newman, J. Comparison of Lithium-Polymer Cell Performance with Unity and Nonunity Transference Numbers. *J. Power Sources* **2000**, *89*, 132–138.

(24) Dai, H.; Zawodzinski, T. a. The Dependence of Lithium Transference Numbers on Temperature, Salt Concentration and Anion Type in Poly (Vinylidene Fluoride)–hexafluoropropylene Copolymer-Based Gel Electrolytes. *J. Electroanal. Chem.* **1998**, *459*, 111–119.

(25) Zugmann, S.; Fleischmann, M.; Amereller, M.; Gschwind, R. M.; Wiemhöfer, H. D.; Gores, H. J. Measurement of Transference Numbers for Lithium Ion Electrolytes via Four Different Methods, a Comparative Study. *Electrochim. Acta* **2011**, *56*, 3926–3933.

(26) Timachova, K.; Watanabe, H.; Balsara, N. P. Effect of Molecular Weight and Salt Concentration on Ion Transport and the Transference Number in Polymer Electrolytes. *Macromolecules* **2015**, *48*, 7882–7888.

(27) Zheng, H.; Li, J.; Song, X.; Liu, G.; Battaglia, V. S. A Comprehensive Understanding of Electrode Thickness Effects on the Electrochemical Performances of Li-Ion Battery Cathodes. *Electrochim. Acta* **2012**, *71*, 258–265.

(28) Winter, M.; Brodd, R. J. What Are Batteries, Fuel Cells, and Supercapacitors? *Chem. Rev.* **2004**, *104*, 4245–4269.

(29) Doyle, M.; Fuller, T. F.; Newman, J. The Importance of the Lithium Ion Transference Number in Lithium/polymer Cells. *Electrochim. Acta* **1994**, *39*, 2073–2081.

(30) Bouchet, R.; Maria, S.; Meziane, R.; Aboulaich, A.; Lienafa, L.; Bonnet, J.-P.; Phan, T. N. T.; Bertin, D.; Gigmes, D.; Devaux, D.; *et al.* Single-Ion BAB Triblock Copolymers as Highly Efficient Electrolytes for Lithium-Metal Batteries. *Nat. Mater.* **2013**, *12*, 452–457.

(31) Zhang, H.; Maitra, P.; Liu, B.; Wunder, S. L.; Lin, H.-P.; Salomon, M. Preparation and

Characterization of Single Ion Conductors from High Surface Area Fumed Silica.

(32)   Kreuer, K.; Wohlfarth, A.; Araujo, C. C. De; Fuchs, A.; Maier, J. Single Alkaline-Ion (Li + , Na +) Conductors by Ion Exchange of Proton-Conducting Ionomers and Polyelectrolytes. **2011**, 2558–2560.

(33)   Adachi, B. G.; Imanaka, N.; Aono, H. Fast Li+ Conducting Ceramic Electrolytes. *Adv. Mater.* **1996**, *8*, 127–135.

(34)   Luntz, A. C.; Voss, J.; Reuter, K. Interfacial Challenges in Solid-State Li Ion Batteries. *J. Phys. Chem. Lett.* **2015**, *6*, 4599–4604.

(35)   Kamaya, N.; Homma, K.; Yamakawa, Y.; Hirayama, M.; Kanno, R.; Yonemura, M.; Kamiyama, T.; Kato, Y.; Hama, S.; Kawamoto, K. A Lithium Superionic Conductor. *Nat. Mater.* **2011**, *10*, 682–686.

(36)   Porcarelli, L.; Shaplov, A. S.; Bella, F.; Nair, J. R.; Mecerreyes, D.; Gerbaldi, C. Single-Ion Conducting Polymer Electrolytes for Lithium Metal Polymer Batteries That Operate at Ambient Temperature. *ACS Energy Lett.* **2016**, *1*, 678–682.

(37)   Oh, H.; Xu, K.; Yoo, H. D.; Kim, D. S.; Chanthad, C.; Yang, G.; Jin, J.; Ayhan, I. A.; Oh, S. M.; Wang, Q. Poly(arylene Ether)-Based Single-Ion Conductors for Lithium-Ion Batteries. *Chem. Mater.* **2016**, *28*, 188–196.

(38)   Wang, M.; Zhao, F.; Dong, S. A Single Ionic Conductor Based on Nafion and Its Electrochemical Properties Used As Lithium Polymer Electrolyte. *J. Phys. Chem. B* **2004**, *108*, 1365–1370.

(39)   Riley, M.; Fedkiw, P. S.; Khan, S. a. Transport Properties of Lithium Hectorite-Based Composite Electrolytes. *J. Electrochem. Soc.* **2002**, *149*, A667.

(40)   Holz, M.; Mao, X.; Seiferling, D.; Sacco, A. Experimental Study of Dynamic Isotope Effects in Molecular Liquids: Detection of Translation-rotation Coupling. *J. Chem. Phys.* **1996**, *104*, 669–679.

(41)   Ohuchi, M.; P, M.; Horiuchi, H.; Sakai, Y.; Furihata, K. Dynamics of Sodium and Lithium Counter-Ions and Water Molecules in Cation-Exchange Resins as Shown by NMR Spectroscopy. *Polym. J.* **2000**, *32*, 760–770.

(42)   Jerschow, A.; Muller, N. Convection Compensation in Gradient Enhanced Nuclear Magnetic Resonance Spectroscopy. *J. Magn. Reson.* **1998**, *132*, 13–18.

(43)   Jerschow, A.; Muller, N. Supression of Convection Artifacts in Stimulated-Echo Diffusion Experiments. Double-Stimulated-Echo Experiments. *J. Magn. Reson.* **1997**, *125*, 372–375.

(44)   Xu, W.; Angell, C. A. LiBOB and Its Derivatives. *Electrochem. Solid-State Lett.* **2001**, *4*, E1–E4.

(45)   Oostwal, M. G.; Blees, M. H.; Bleijser, J. De; Leyte, J. C. Chain Self-Diffusion in Aqueous Salt-Free Solutions of Sodium Poly(Styrenesulfonate). *Macromolecules* **1993**, *26*, 7300–7308.

(46)   Schipper, F.; Leyte, J. C. Mass Transport in Polyelectrolyte Solutions. *J. Phys. Condens. Matter* **1999**, *11*, 1409–1421.

(47)   Hayamizu, K.; Aihara, Y.; Arai, S. Pulse-Gradient Spin-Echo 1 H, 7 Li, and 19 F NMR Diffusion and Ionic Conductivity Measurements of 14 Organic Electrolytes Containing LiN(SO2CF3)2. *J.*

Phys. Chem. B **1999**, *103*, 519–524.

(48)   Edman, L.; Doeff, M. M.; Ferry, A.; Kerr, J.; De Jonghe, L. C. Transport Properties of the Solid Polymer Electrolyte System P(EO)nLiTFSI. *J. Phys. Chem. B* **2000**, *104*, 3476–3480.

(49)   Newman, J.; Thomas-Alyea, K. E. *Electrochemical Systems*; 3rd ed.; John Wiley & Sons, Inc., 2004.

(50)   Lascaud, S.; Perrier, M.; Vallee, A.; Besner, S.; Prud'homme, J.; Armand, M. Phase Diagrams and Conductivity Behavior of Poly (Ethylene Oxide)-Molten Salt Rubbery Electrolytes. *Macromolecules* **1994**, *27*, 7469–7477.

(51)   Goodenough, J. B.; Kim, Y. Challenges for Rechargeable Li Batteries. *Chem. Mater.* **2010**, *22*, 587–603.

(52)   Videa, M.; Xu, W.; Geil, B.; Marzke, R.; Angell, C. A. High Li+ Self-Diffusivity and Transport Number in Novel Electrolyte Solutions. *J. Electrochem. Soc.* **2001**, *148*, A1352–A1356.

(53)   Chauvin, C.; Ollivrin, X.; Alloina, F.; Lenest, J.; Sanchez, J. Lithium Salts Based on Oligoether Sulfate Esters. *Electrochim. Acta* **2005**, *50*, 3843–3852.

(54)   Chintapalli, M.; Timachova, K.; Olson, K. R.; Mecham, S. J.; Devaux, D.; DeSimone, J. M.; Balsara, N. P. Relationship between Conductivity, Ion Diffusion, and Transference Number in Perfluoropolyether Electrolytes. *Macromolecules* **2016**, *49*, 3508–3515.

(55)   Noda, A.; Hayamizu, K.; Watanabe, M. Pulsed-Gradient Spin - Echo 1 H and 19 F NMR Ionic Diffusion Coefficient , Viscosity , and Ionic Conductivity of Non-Chloroaluminate Room-Temperature Ionic Liquids. **2001**, 4603–4610.

(56)   Chintapalli, M.; Le, T. N. P.; Venkatesan, N. R.; Mackay, N. G.; Rojas, A. A.; Thelen, J. L.; Chen, X. C.; Devaux, D.; Balsara, N. P. Structure and Ionic Conductivity of Polystyrene- *Block* - Poly(ethylene Oxide) Electrolytes in the High Salt Concentration Limit. *Macromolecules* **2016**, acs.macromol.5b02620.

(57)   Fuoss, R. M. Polyelectrolytes. *Proc. Natl. Acad. Sci.* **1951**, *37*.

(58)   Dobrynin, A. V; Colby, R. H.; Rubinstein, M. Scaling Theory of Polyelectrolyte Solutions. *Macromolecules* **1996**, *28*, 1859–1871.

(59)   Odijk, T. Possible Scaling Relations for Semidilute Polyelectrolyte Solutions. *Macromolecules* **1979**, *12*, 688–693.

(60)   Vizcarra-Rendón, A.; Medina-Noyola, M.; Klein, R. Electrolyte Friction on Non-Spherical Polyions. *Chem. Phys. Lett.* **1990**, *173*, 397–402.

(61)   Schurr, J. M. A Theory of Electrolyte Friection on Translating Polyelectrolytes. *Chem. Phys.* **1980**, *45*, 119–132.

(62)   Krause, W. E.; Tan, J. S.; Colby, R. H. Semidilute Solution Rheology of Polyelectrolytes with No Added Salt. **1999**, 3429–3437.

(63)   Schipper, F.; Hollander, J. G.; Leyte, J. C. The Influence of Screening of the Polyion Electrostatic Potential on the Counterion Dynamics in Polyelectrolyte Solutions. *J. Phys. Condens. Matter* **1998**, *10*, 99207–99220.

(64) Hubbard, J. B.; Onsager, L. Dielectric Dispersion and Dielectric Friction in Electrolyte Solutions. I. *J. Chem. Phys.* **1977**, *67*, 4850.

(65) Bird, R. B.; Stewart, W. E.; Lightfoot, E. N. *Transport Phenomena*; Anderson, W.; Kulek, P., Eds.; Second.; John Wiley & Sons Inc., 2007.

(66) Angell, C. a; Ngai, K. L.; McKenna, G. B.; McMillan, P. F.; Martin, S. W. Relaxation in Glassforming Liquids and Amorphous Solids. *J. Appl. Phys.* **2000**, *88*, 3113–3157.

(67) Ediger, M. D.; Angell, C. A.; Nagel, S. R. Supercooled Liquids and Glasses. *J. Phys. Chem.* **1996**, *100*, 13200–13212.

(68) Gorecki, W.; Roux, C.; Clémancey, M.; Armand, M.; Belorizky, E. NMR and Conductivity Study of Polymer Electrolytes in the Imide Family: P(EO)/Li[N(SO2CnF2n+1)(SO2CmF2m+1)]. *ChemPhysChem* **2002**, *3*, 620–625.

(69) Dobrynin, A. V; Rubinstein, M. Theory of Polyelectrolytes in Solutions and at Surfaces. *Prog. Polym. Sci.* **2005**, *30*, 1049–1118.

(70) Colby, R. H.; Dobrynin, A. V. Dynamics of Semidilute Polyelectrolyte Solutions. *Phys. Rev. Lett.* **1994**, *73*, 2776–2779.

(71) Oostwal, M.; Odijk, T. Novel Dynamic Scaling Hypothesis for Semidilute and Concentrated Solutions of Polymers and Polyelectrolytes. *Macromolecules* **1993**, *26*, 6489–6497.

(72) Barrat, J.-L.; Joanny, J.-F. Theory of Polyelectrolyte Solutions. *Adv. Chem. Phys.* **1995**.

(73) Liao, Q.; Dobrynin, A. V; Rubinstein, M. Molecular Dynamics Simulations of Polyelectrolyte Solutions: Nonuniform Stretching of Chains and Scaling Behavior. **2003**, 3386–3398.

(74) Smiatek, J.; Wohlfarth, A.; Holm, C. The Solvation and Ion Condensation Properties for Sulfonated Polyelectrolytes in Different Solvents — a Computational Study. *New J. Phys.* **2014**, *16*, 0–21.

(75) Ganter, J. L. M. S.; Milas, M.; Rinaudo, M. On the Viscosity of Sodium Poly(styrene Sulphonate), a Flexible Polyelectrolyte. *Polymer (Guildf).* **1992**, *33*, 113–116.

(76) Sedlak, M.; Konák, C.; Stepanek, P.; Jakes, J. Semidilute Solutions of Poly (Methacrylic Acid) in the Absence of Salt : Dynamic Light- Scattering Study. *Polymer (Guildf).* **1987**, *28*, 873–880.

(77) Hiemenz, P. C.; Lodge, T. P. *Polymer Chemistry*; 2nd ed.; Taylor & Francis: Boca Raton, FL, 2007.

(78) Odijk, T. Polyelectrolytes near the Rod Limit. *J. Polym. Sci. Polym. Phys. Ed.* **1977**, *15*, 477–483.

(79) Bell, G. M. Self-Diffusion of Ions in the Electric Fields of Spherical Particles. *T. Faraday Soc.* **1964**, *60*, 1752.

(80) Holz, M.; Heil, S. R.; Sacco, A. Temperature-Dependent Self-Diffusion Coefficients of Water and Six Selected Molecular Liquids for Calibration in Accurate 1H NMR PFG Measurements. *Phys. Chem. Chem. Phys.* **2000**, *2*, 4740–4742.

(81) Nishida, K.; Kaji, K.; Kanaya, T.; Fanjat, N. Determination of Intrinsic Viscosity of Polyelectrolyte Solutions. **2002**, *43*, 1295–1300.

(82)   Cohen, J.; Priel, Z.; Rabin, Y. Viscosity of Dilute Polyelectrolyte Solutions. *J. Chem. Phys.* **1988**, *88*, 7111–7116.

(83)   Wyatt, N. B.; Gunther, C. M.; Liberatore, M. W. Increasing Viscosity in Entangled Polyelectrolyte Solutions by the Addition of Salt. *Polymer (Guildf).* **2011**, *52*, 2437–2444.

(84)   Van Zoelen, W.; Buss, H. G.; Ellebracht, N. C.; Lynd, N. A.; Fischer, D. A.; Finlay, J.; Hill, S.; Callow, M. E.; Callow, J. A.; Kramer, E. J.; *et al.* Sequence of Hydrophobic and Hydrophilic Residues in Amphiphilic Polymer Coatings Affects Surface Structure and Marine Antifouling/fouling Release Properties. *ACS Macro Lett.* **2014**, *3*, 364–368.

(85)   Leng, C.; Buss, H. G.; Segalman, R. A.; Chen, Z. Surface Structure and Hydration of Sequence-Specific Amphiphilic Polypeptoids for Antifouling/Fouling Release Applications. *Langmuir* **2015**, *31*, 9306–9311.

(86)   Callow, J. A.; Callow, M. E. Trends in the Development of Environmentally Friendly Fouling-Resistant Marine Coatings. *Nat. Commun.* **2011**, *2*.

(87)   Kirschner, C. M.; Brennan, A. B. Bio-Inspired Antifouling Strategies. *Annu. Rev. Mater. Res.* **2012**, *42*, 211–229.

(88)   Thomas, K. V; Brooks, S. The Environmental Fate and Effects of Antifouling Paint Biocides. *Biofouling* **2010**, *26*, 73–88.

(89)   Callow, M. E.; Callow, J. A.; Pickett-Heaps, J. D.; Wetherbee, R. Primary Adhesion of Enteromorpha (Chlorophyta, Ulvales) Propagules: Quantitative Settlement Studies and Video Microscopy. *J. Phycol.* **1997**, *33*, 938–947.

(90)   Roberts, D.; Rittschof, D.; Holm, E.; Schmidt, A. R. Factors Influencing Initial Larval Settlement: Temporal, Spatial and Surface Molecular Components. *J. Exp. Mar. Bio. Ecol.* **1991**, *150*, 203–221.

(91)   Callow, J. A.; Callow, M. E. *Biological Adhesives*; 2006.

(92)   Callow, J. A.; Callow, M. E.; Ista, L. K.; Lopez, G.; Chaudhury, M. K. The Influence of Surface Energy on the Wetting Behaviour of the Spore Adhesive of the Marine Alga Ulva Linza (Synonym Enteromorpha Linza). *J. R. Soc. INTERFACE* **2005**, *2*, 319–325.

(93)   Zuckermann, R. N.; Kerr, J. M.; Kent, S. B. H.; Moos, W. H. Efficient Method for the Preparation of Peptoids [oligo(N-Substituted Glycines)] by Submonomer Solid-Phase Synthesis. *J. Am. Chem. Soc.* **1992**, *114*, 10646–10647.

(94)   Rosales, A. M.; Murnen, H. K.; Zuckermann, R. N.; Segalman, R. A. Control of Crystallization and Melting Behavior in Sequence Specific Polypeptoids. *Macromolecules* **2010**, *43*, 5627–5636.

(95)   Carman, M. L.; Estes, T. G.; Feinberg, A. W.; Schumacher, J. F.; Wilkerson, W.; Wilson, L. H.; Callow, M. E.; Callow, J. A.; Brennan, A. B. Engineered Antifouling Microtopographies - Correlating Wettability with Cell Attachment. *Biofouling* **2006**, *22*, 11–21.

(96)   Chaudhury, M. K.; Finlay, J. A.; Chung, J. Y.; Callow, M. E.; Callow, J. A. The Influence of Elastic Modulus and Thickness on the Release of the Soft-Fouling Green Alga Ulva Linza (Syn. Enteromorpha Linza) from Poly(dimethylsiloxane) (PDMS) Model Networks. *Biofouling* **2005**, *21*, 41–48.

(97)   Statz, A.; Finlay, J.; Dalsin, J.; Callow, M. E.; Callow, J. A.; Messersmith, P. B. Algal Antifouling and Fouling-Release Properties of Metal Surfaces Coated with a Polymer Inspired by Marine Mussels. *Biofouling* **2006**, *22*, 391–399.

(98)   Krishnan, S.; Ayothi, R.; Hexemer, A.; Finlay, J. A.; Sohn, K. E.; Perry, R.; Ober, C. K.; Kramer, E. J.; Callow, M. E.; Callow, J. A.; *et al.* Anti-Biofouling Properties of Comblike Block Copolymers with Amphiphilic Side Chains. *Langmuir* **2006**, *22*, 5075–5086.

(99)   Dimitriou, M. D.; Zhou, Z.; Yoo, H. S.; Killops, K. L.; Finlay, J. A.; Cone, G.; Sundaram, H. S.; Lynd, N. A.; Barteau, K. P.; Campos, L. M.; *et al.* A General Approach to Controlling the Surface Composition of Poly(ethylene Oxide)-Based Block Copolymers for Antifouling Coatings. *Langmuir* **2011**, *27*, 13762–13772.

(100)   Zhang, Z.; Finlay, J. A.; Wang, L.; Gao, Y.; Callow, J. A.; Callow, M. E.; Jiang, S. Polysulfobetaine-Grafted Surfaces as Environmentally Benign Ultralow Fouling Marine Coatings. *Langmuir* **2009**, *25*, 13516–13521.

(101)   Figliozzi, G. M.; Goldsmith, R.; Ng, S. C.; Banville, S. C.; Zuckermann, R. N. Synthesis of N-Substituted Glycine Peptoid Libraries. *Methods Enzymol.* **1996**, *267*, 437–447.

(102)   van Zoelen, W.; Zuckermann, R. N.; Segalman, R. A. Tunable Surface Properties from Sequence-Specific Polypeptoid–Polystyrene Block Copolymer Thin Films. *Macromolecules* **2012**, *45*, 7072–7082.

(103)   Genzer, J.; Sivaniah, E.; Kramer, E. J.; Wang, J.; Xiang, M.; Char, K.; Ober, C. K.; Bubeck, R. A.; Fischer, D. A.; Graupe, M.; *et al.* Molecular Orientation of Single and Two-Armed Monodendron Semifluorinated Chains on "Soft" and "Hard" Surfaces Studied Using NEXAFS. *Macromolecules* **2000**, *33*, 6068–6077.

(104)   Paik, M. Y.; Krishnan, S.; You, F.; Li, X.; Hexemer, A.; Ando, Y.; Kang, S. H.; Fischer, D. A.; Kramer, E. J.; Ober, C. K. Surface Organization, Light-Driven Surface Changes, and Stability of Semifluorinated Azobenzene Polymers. *Langmuir* **2007**, *23*, 5110–5119.

(105)   Sohn, K. E.; Dimitriou, M. D.; Genzer, J.; Fischer, D. A.; Hawker, C. J.; Kramer, E. J. Determination of the Electron Escape Depth for NEXAFS Spectroscopy. *Langmuir* **2009**, *25*, 6341–6348.

(106)   Samant, M. G.; Stöhr, J.; Brown, H. R.; Russell, T. P.; Sands, J. M.; Kumar, S. K. NEXAFS Studies on the Surface Orientation of Buffed Polyimides. *Macromolecules* **1996**, *29*, 8334–8342.

(107)   Liu, Y.; Russell, T. P.; Samant, M. G.; Stöhr, J.; Brown, H. R.; Cossy-Favre, A.; Diaz, J. Surface Relaxations in Polymers. *Macromolecules* **1997**, *30*, 7768–7771.

(108)   Leng, C.; Han, X.; Shao, Q.; Zhu, Y.; Li, Y.; Jiang, S.; Chen, Z. In Situ Probing of the Surface Hydration of Zwitterionic Polymer Brushes: Structural and Environmental Effects. *J. Phys. Chem. C* **2014**, *118*, 15840–15845.

(109)   Mieszkin, S.; Martin-Tanchereau, P.; Callow, M. E.; Callow, J. a. Effect of Bacterial Biofilms Formed on Fouling-Release Coatings from Natural Seawater and Cobetia Marina, on the Adhesion of Two Marine Algae. *Biofouling* **2012**, *28*, 953–968.

(110)   Schultz, M. P.; Finlay, J. A.; Callow, M. E.; Callow, J. A. A Turbulent Channel Flow Apparatus for the Determination of the Adhesion Strength of Microfouling Organisms. *Biofouling* **2000**, *15*,

243+.

(111) Shen, Y. R. Basic Theory of Surface Sum-Frequency Generation. *J. Phys. Chem. C* **2012**, *116*, 15505–15509.

(112) Shen, Y. R. Surface Properties Probed by Second-Harmonic and Sum-Frequency Generation. *Nature* **1989**, *337*, 519–525.

(113) Grozea, C. M.; Gunari, N.; Finlay, J. A.; Grozea, D.; Callow, M. E.; Callow, J. A.; Lu, Z.-H.; Walker, G. C. Water-Stable Diblock Polystyrene- Block -poly(2-Vinyl Pyridine) and Diblock Polystyrene- Block -Poly(methyl Methacrylate) Cylindrical Patterned Surfaces Inhibit Settlement of Zoospores of the Green Alga Ulva. *Biomacromolecules* **2009**, *10*, 1004–1012.

(114) Statz, A. R.; Meagher, R. J.; Barron, A. E.; Messersmith, P. B. New Peptidomimetic Polymers for Antifouling Surfaces. *J. Am. Chem. Soc.* **2005**, *127*, 7972–7973.

(115) Imbesi, P. M.; Finlay, J. A.; Aldred, N.; Eller, M. J.; Felder, S. E.; Pollack, K. A.; Lonnecker, A. T.; Raymond, J. E.; Mackay, M. E.; Schweikert, E. A.; *et al.* Targeted Surface Nanocomplexity: Two-Dimensional Control over the Composition, Physical Properties and Anti-Biofouling Performance of Hyperbranched Fluoropolymer–poly(ethylene Glycol) Amphiphilic Crosslinked Networks. *Polym. Chem.* **2012**, *3*, 3121.

(116) Lewis, P. R.; Price, C. Electron Microscopy of Sym-SBS Block Polymers. *Polymer (Guildf).* **1972**, *13*, 20–26.

(117) Bothe, M.; Schmidt-Naake, G. An Improved Catalytic Method for Alkoxyamine Synthesis − Functionalized and Biradical Initiators for Nitroxide-Mediated Radical Polymerization. *Macromol. Rapid Commun.* **2003**, *24*, 609–613.

(118) Hawker, C. J.; Bosman, A. W.; Harth, E. New Polymer Synthesis by Nitroxide Mediated Living Radical Polymerizations. *Chem. Rev.* **2001**, *101*, 3661–3688.

(119) Martinelli, E.; Suffredini, M.; Galli, G.; Glisenti, A.; Pettitt, M. E.; Callow, M. E.; Callow, J. A.; Williams, D.; Lyall, G. Amphiphilic Block Copolymer/poly(dimethylsiloxane) (PDMS) Blends and Nanocomposites for Improved Fouling-Release. *Biofouling* **2011**, *27*, 529–541.

(120) Calabrese, D. R.; Wenning, B. M.; Buss, H. G.; Finlay, J. A.; Fischer, D. A.; Claire, A.; Segalman, R. A.; Ober, C. K. Comparison Onf Hydrophobic and Hydrophilic Polymer Backbones with Pendent Oligopeptide Units for Antifouling and Fouling-Release Coatings. *Green Mater.*

(121) Dimitriou, M. D.; Sundaram, H. S.; Cho, Y.; Paik, M. Y.; Kondo, M.; Schmidt, K.; Fischer, D. A.; Ober, C. K.; Kramer, E. J. Amphiphilic Block Copolymer Surface Composition: Effects of Spin Coating versus Spray Coating. *Polymer (Guildf).* **2012**, *53*, 1321–1327.

(122) Weinman, C. J.; Finlay, J. A.; Park, D.; Paik, M. Y.; Krishnan, S.; Sundaram, H. S.; Dimitriou, M.; Sohn, K. E.; Callow, M. E.; Callow, J. A.; *et al.* ABC Triblock Surface Active Block Copolymer with Grafted Ethoxylated Fluoroalkyl Amphiphilic Side Chains for Marine Antifouling/Fouling-Release Applications. *Langmuir* **2009**, *25*, 12266–12274.

(123) Zhou, Z.; Calabrese, D. R.; Taylor, W.; Finlay, J. a; Callow, M. E.; Callow, J. a; Fischer, D.; Kramer, E. J.; Ober, C. K. Amphiphilic Triblock Copolymers with PEGylated Hydrocarbon Structures as Environmentally Friendly Marine Antifouling and Fouling-Release Coatings. *Biofouling* **2014**, *30*, 589–604.

(124) Black, S. B.; Chang, Y.; Bae, C.; Hickner, M. A. FTIR Characterization of Water-Polymer Interactions in Superacid Polymers. *J. Phys. Chem. B* **2013**, *117*, 16266–16274.

(125) Shaplov, A. S.; Vlasov, P. S.; Armand, M.; Lozinskaya, E. I.; Ponkratov, D. O.; Malyshkina, I. a.; Vidal, F.; Okatova, O. V.; Pavlov, G. M.; Wandrey, C.; *et al.* Design and Synthesis of New Anionic "polymeric Ionic Liquids" with High Charge Delocalization. *Polym. Chem.* **2011**, *2*, 2609–2618.

(126) Axnanda, S.; Crumlin, E. J.; Mao, B.; Rani, S.; Chang, R.; Karlsson, P. G.; Edwards, M. O. M.; Lundqvist, M.; Moberg, R.; Ross, P.; *et al.* Using "Tender" X-Ray Ambient Pressure X-Ray Photoelectron Spectroscopy as A Direct Probe of Solid-Liquid Interface. *Sci. Rep.* **2015**, *5*, 9788.

(127) Zhang, Z.; Vaisocherová, H.; Cheng, G.; Yang, W.; Xue, H.; Jiang, S. Nonfouling Behavior of Polycarboxybetaine-Grafted Surfaces: Structural and Environmental Effects. *Biomacromolecules* **2008**, *9*, 2686–2692.